Aero-Acoustic Computations of Wind Turbines

Zhu, Wei Jun; Shen, Wen Zhong; Sørensen, Jens Nørkær

Publication date:
2008

Citation (APA):
Zhu, W. J., Shen, W. Z., & Sørensen, J. N. (2008). Aero-Acoustic Computations of Wind Turbines. (MEK-FM-PHD; No. 2007-02).

MEK-PHD 2007-09

Aero-Acoustic Computations of Wind Turbines

Dissertation submitted to the Technical University of Denmark in partial fulfillment of the requirements for the degree of Doctor of Philosophy in Mechanical Engineering

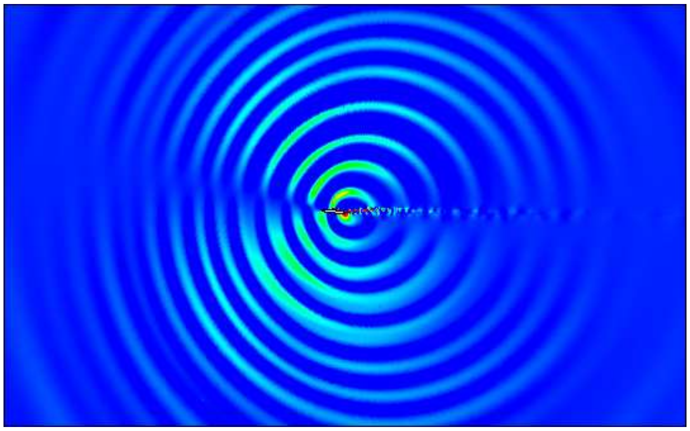

Wei Jun Zhu

Fluid Mechanics
Department of Mechanical Engineering
Technical University of Denmark
September, 2007

Fluid Mechanics
Department of Mechanical Engineering
Nils Koppels Allé, Building 403
Technical University of Denmark
DK-2800 Lyngby, Denmark

Printed in Denmark, Lyngby

MEK-PHD 2007-09 / ISBN 978-87-7475-348-3

This thesis has been typeset using LaTeX2e. Figures were produced using Tecplot, MATLAB, Xfig and ImageMagick.

Preface

This dissertation is submitted in partial fulfillment of the requirement for the Ph.D. degree. The research work has been carried out during the period from June 2004 to August 2007 at the Fluid Mechanics Section, Department of Mechanical Engineering, Technical University of Denmark.

The research was supervised by Associate Professor Wen Zhong Shen and Professor Jens Nørkær Sørensen whom I wish to extend my sincere thanks for their patient guidance and encouraging discussions. Also I wish to give my acknowledgment to the Technical Research Council of Denmark (STVF) which financed my research.

I would like to extend my warm thanks to all my colleagues at Fluid Mechanics Section for creating such a friendly environment. I wish to thank Doc. Dalibor Cavar for the good management of our clusters where I obtained most of my computational results. A warm thank to Professor Jens Nørkær Sørensen and Associate Professor Robert Mikkelsen who have been my good partners in football field.

I want express my thanks to Ph.D. students Niels Troldborg, Clara Marrika Velte, Gabriel Gerardo Martinez Hernández and Jimmy Kjærsgård-Rasmussen for our wonderful Ph.D. life.

My best regards and gratitude to Associate Professor Wen Zhong Shen for his kindly help during the past few years. The knowledge and spirit had great impact on me.

Finally, I would like to thank my family and friends for showing interest of my research. And the last, but definitely not the least, special gratitude to my wife Yuan Lu who has been my most strongest support.

Technical University of Denmark
Lyngby, September 2007

Wei Jun Zhu

Abstract

A high-order finite difference method to predict flow-generated noise is introduced in this thesis. The technique consists of solving the viscous incompressible flow equations and inviscid acoustic equations using an incompressible/acoustic splitting technique. The incompressible flow equations are solved using the in-house flow solver EllipSys2D/3D which is a second-order finite volume code. The acoustic equations are solved using high-order finite difference schemes. The incompressible flow equations and the acoustic equations are solved at the same time levels where the pressure and the velocities obtained from the incompressible equations form the input to the acoustic equations. To achieve low dissipation and dispersion errors, either Dispersion-Relation-Preserving (DRP) schemes or optimized compact finite difference schemes are used for spatial discretizations of the acoustic equations. The acoustic solver consists of numerical schemes from fourth-order up to tenth-order accuracy, the use of different schemes are case dependent. In practice, at high Reynolds numbers when flow becomes turbulent, schemes with the highest order of accuracy are always used to resolve the small waves. For time integration, the classical 4-stage Runge-Kutta scheme is applied. Non-centered high-order schemes at numerical boundaries and high-order filter schemes are also discussed due to their importance.

The method was validated against a few test cases and further applied for flows around a cylinder and an airfoil both for laminar and turbulent flows. Results have shown that sound generation is due to the unsteadiness of the flow field and the spectrum of sound has a strong relation with fluctuating forces on the solid body. Flow and acoustic simulation were also carried out for a wind turbine where general trends of sound generation from blades was found.

Dansk resumé

En høj-ordens finite difference metode til forudsigelse af strømnings-genereret støj bliver introduceret i denne afhandling. Teknikken består i at løse de viskøse ikke-kompressible ligninger for strømningen ved brug af en ikke-kompressibel/akustisk splitting teknik. De ikke-kompressible ligninger for strømningen løses med EllipSys2D/3D der er en anden-ordens finite volume løser udviklet her på MEK. De akustiske ligninger løses med høj-ordens finite difference metoder. De ikke-kompressible ligninger for strømningen og de akustiske ligninger sammenkobles på hvert skridt ved at trykket og hastighederne fra EllipSys bruges som input til de akustiske ligninger. For at opnå små dissipations og dispersions fejl, bruges enten Dispersion-Relation-Preserving (DRP) eller optimerede kompakte finite difference metoder til rumlig diskretisering af de akustiske ligninger. Den akustiske løser består af numeriske metoder fra fjerde-ordens op til tiende-ordens nøjagtighed. Brugen af de forskellige metoder afhænger af problemet. I praksis bruges den højest mulige orden altid ved høje Reynolds tal med turbulent strømning, for at opløse de små bølger. Til integration bruges den klassiske fjerde-ordens Runge-Kutta metode. Ikke-centrerede høj-ordens metoder ved numeriske grænser og høj-ordens filter metoder diskuteres grundet deres vigtighed.

Metoden blev valideret på et par test problemer og videre anvendt for strømning om en cylinder og et bæreplan, både for laminære og turbulente strømninger. Resultater har vist at lyd kilder skabes ved ustabiliteter i strømnings feltet og at lyd-spektret har en stærk relation til fluktuerende kræfter på objektet i strømningen. Strømnings- og akustik-simulering blev også udført for en vindmølle, hvor generelle tendenser for lyd generering på bladene blev fundet.

List of Publications

In peer-reviewed journals (2004-2007)

Zhu W J, Heilskov N, Shen W Z and Sørensen J N 2005 Modeling of Aerodynamically Generated Noise From Wind Turbines. *J. Solar Energy Engineering* **127** 517-528.

Zhu W J, Shen W Z and Sørensen J N 2005 An Aerodynamic Noise Propagation Model for Wind Turbines. *J. Wind Engineering* **2** 129-143.

Brøns M, Shen W Z, Sørensen J N and Zhu W J 2007 The influence of imperfections on the flow structure of steady vortex breakdown bubbles. *J. Fluid. Mech.* **578** 453-466.

In conference proceedings (2004-2007)

Zhu W J, Shen W Z and Sørensen J N 2007 Airfoil Noise Computation Use High-order Schemes. *European Wind Energy Conference, Milan, Italy*

Zhu W J, Shen W Z and Sørensen J N 2007 Computational Aero-Acoustic using High-order Schemes. *J. Phys. Conference Series* 75 (2007) 012084

Leloudas G, Zhu W J, Sørensen J N and Shen W Z 2007 Prediction and reduction of noise from a 2.3 MW wind tubine. *J. Phys. Conference Series* 75 (2007) 012083

List of Figures

List of Tables

List of Symbols

Roman letters

A	Amplitude
c_0, c	Sound speed / Chord length
C_d, C_l	Drag and lift coefficients
c_p	Specific heat capacity / Phase speed
C_p	Pressure coefficient
f, f_e, f_o	Frequency
f_i	Acoustic co-variable
k	Coefficient of thermal conductivity / Wave number
l_i, l_j	Vector pointing from source to observer
$\mathcal{L}_i$	Characteristic waves
M	Mach number
$\mathcal{O}$	High-order terms
p, P	Incompressible pressure
p'	Fluctuating pressure
p'_L	Loading component of p'
p'_Q	Quadrupole component of p'
p'_S	Surface component of p'
p'_T	Thickness component of p'
p'_V	Volume component of p'
r	Radius
R	Radius / Gas constant
$\mathcal{R}$	Real part of a complex number
S	Entropy / Integration area
t	Time
t'	Retarded time
T	Temperature
T_{ij}	Lighthill's stress tensor
u, v, w	Velocity components in cartesian system
v_θ, v_r	Velocity components in polar system
U, V, W	Flow velocity components
u', v', w'	Acoustic velocity components
V_θ	Group velocity
W	Weighting function
x, y, z	Cartesian coordinate system
$\mathtt{x}, \mathtt{y}$	Receiver and Observer points

Greek letters

α	Angle of attack / Wave number
β	Coefficient of thermal expansion
δ_d	Filter coefficient
$\delta(f)$	Dirac delta function
δ_{ij}	Kronecker delta
ϕ	Viscous dissipation
γ	Specific heat ratio / Grid stretching rate
λ	Wave length
ε	Error tolerance
σ	Damping coefficient
φ	The mean flow angle

η	Integral limit
θ	Azimuthal angle
μ	Viscosity
ν	Kinematic viscosity
ν_t	Eddy viscosity
Γ	Vortex strength
ρ	Flow density
ρ'	Fluctuating density
τ_{ij}	Stress tensor
ω	Angular rotor velocity / Wave number
Ω	Integration area

Indices

$_\infty$	Farfield
$_o$	Free stream / flow at rest
$'$	Fluctuation / Space derivative
$''$	Second-order space derivative
$_n$	Normal direction
$\hat{}$	Vector pointing outwards
$_r$	In radiation direction
$\dot{}$	Time differentiation
$\bar{}$	Mean value / Matrix
$\tilde{}$	Laplace or Fourier transform / Filter / Matrix
$_e$	External oscillation
$_{ret}$	At retarded time
$_{ref}$	At reference position

Special numbers

CFL	Courant - Friedrichs - Lewy number
Re	Reynolds number
St	Strouhal number

Acronyms

2D,3D	Two, three-dimensional
BPM	Brooks, Pope and Marcolini
CAA	Computational aeroacoustics
CFD	Computational fluid dynamics
CPU	Central processing unit
DES	Detached eddy simulation
DNS	Direct numerical simulation
DRP	Dispersion-relation-preserving scheme
FFT	Fast Fourier transform
GKS	Gustafsson, Kreiss and Sundstrom
HPC	High performance computing
LES	Large eddy simulation
MPI	Message Passing Interface for parallel computations
NS	Navier-Stokes equations
PDEs	Partial differential equations
PML	Perfectly matching layer
RANS	Reynolds-averaged Navier-Stokes
SPL	Sound pressure level
TE	Truncation error

Contents

Part I

Theory

Chapter 1

Introduction

The practical interest of this thesis is the use of high-order numerical methods to predict sound generation due to unsteady flow field around solid bodies such as airfoils. Computational Aeroacoustics (CAA) is such a technique developed for solving flow induced noise. Within this technique, incompressible/acoustic splitting methods[1, 2] is used in the current study. Wave number optimized high-order numerical schemes are used to discretize the acoustic equations.

In recent years, the vast development of High Performance Computing (HPC) technology provides the possibility for numerical aerodynamics to effectively resolve complex flows with reasonably large meshes. Computational Fluid Dynamics (CFD) has reached a very mature state since its early beginning in the middle of last century. However, CAA has been separated as an individual research area only since 1990s. It might be a bit confusing to separate aeroacoustics from aerodynamics since aeroacoustics is also motion of air. The same argument might hold for CFD and CAA which use similar numerical approaches. The major distinction between them is the small length scale and magnitude of CAA quantities relative to the quantities of the flow. In addition, however, CFD deals with algorithms. Problems occur by utilizing standard CFD procedures for aeroacoustic problems. The first difficulty is due to the extremely small magnitude of waves. For noise level up to 100 dB which is terrifyingly loud and not supposed to happen very often, the magnitude of the fluctuating sound pressure is only less than 10^{-4} of the ambient atmospheric pressure. Another issue for CAA is that the resolvable high frequency components are related to the order of numerical schemes, the grid density and quality. CAA has a few distinct characteristics as compared to CFD, and therefore more attention needs to be drawn.

Efforts have been done during last few decades in the area of CAA. The aeroacoustic computation of flow generated noise was pioneered by Lighthill

[3] in the 1950th. Soon after that, Lighthill's equation, the acoustic analogy, became widely used. The acoustic analogy is applied for flow generated noise in many situations, typically for predicting jet noise. Improvements of Lighthill's acoustic equation are still going on and much effort is still made to generalize the theoretical description. Among those, Curle [4] extended the theory by including the influence of static boundaries. Subsequently, Ffowcs Williams et al. [5] extended it further by including the influence of boundaries in arbitrary motion. In all the approaches, the key issue is to compute the sound sources generated by the flow that relates exactly to integrals of surface and volume source terms. These source terms can be obtained by solving the incompressible/compressible Navier-Stokes (NS) equations in the near-field. Once the source terms are known, the acoustic far-field can be solved by using the acoustic analogy.

The most accurate way of simulating aerodynamically generated noise is Direct Numerical Simulation (DNS) where both fluid flow and sound are obtained directly from solving the compressible NS equations. With this method, it is possible to accurately predict near-field sound generation. To solve the problem, however, a very fine mesh and highly accurate schemes both in space and time are needed. Studies that make use of DNS can be found in [6, 7, 8] where a few typical computational cases were shown. To obtain time series of acoustic signals and determine the acoustic spectra distribution, the computational time has to be long enough which is a realistic problem for DNS. The method is straight forward, however, studies using DNS to simulate aeroacoustics are so far limited due to requirement of a large amount of computer resource.

Another method also is a newly developed method, called incompressible/acoustic splitting method, was proposed by Hardin and Pope [1] in 1994. Shen and Sørensen [2] remedied the original splitting technique by changing slightly the basic decomposition of the variables. The decomposition technique proposed by Shen and Sørensen is used in the present work. The first part of the splitting approach is the viscous flow part which is simulated from the incompressible NS equations. The variables obtained from the incompressible solver are used in the second part of the calculation where the acoustic or perturbed equations are solved. Under the assumption of low Mach number, the perturbed quantities represent the difference between compressible flow and incompressible flow. Therefore, the perturbed variables are solved in the compressible equations by knowing all incompressible quantities. The modified splitting method has been applied by Shen and Sørensen [9, 10, 11] for flows past a cylinder and an airfoil for both laminar and turbulent flow cases where second-order finite volume/finite difference methods are used for the flow and the acoustic computations. The results obtained from previous computations are encouraging and may possibly be an effective and convenient method of near field acoustic simulation for low Mach number flows. As an extension to previous work, in the present work, high-order finite difference schemes are used to solve acoustic equations. The use of high-order schemes is due to the large disparity between the length and time scales of the flow and acoustics. A high-order wave number optimized scheme was developed by Tam and Webb [12] which is the so-called Dispersion-Relation-Preserving (DRP) scheme. Using the strategy of developing DRP scheme and apply on the original high-order compact finite difference schemes of Lele [13], Kim and Lee [14] derived an wave number optimized compact scheme. Both the high-order DRP schemes and optimized compact schemes have the characteristic of low dissipation and dispersion error which are designed for wave propagation problems.

The thesis is structured as follows: Chapter 2 and Chapter 3 are the theoretical parts where acoustic models are discussed in Chapter 2 and high-order numerical methods of solving those acoustic models are given in Chapter 3. Applications of acoustic theory are shown in Chapter 4, 5 and 6. Finally, the conclusions of the present work are given in Chapter 7.

Chapter 2

The CAA methods

This chapter provides a brief review of some commonly used computational methods in the field of computational aeroacoustics. Numerical prediction of noise can be classified into two groups: the direct method and hybrid approaches. A schematic diagram of CAA methods is given in Figure 2.1. It is seen that there are quite a few numerical approaches to simulate flow generated noise. The direct method solves the compressible NS equations which compute both sound and flow field together. The hybrid approach computes flow and acoustic field separately where solution from flow computation is used to start acoustic computation. Among the hybrid methods the incompressible/acoustic splitting technique is used in our numerical simulation and therefore it is given in more details.

2.1 Flow induced noise

Noise radiation is directly associated with flow unsteadiness. The more unsteady the flow is, the louder the noise level will be. The energy of the generated sound is proportional to the turbulence energy, but sound energy is negligible small compared to flow energy. Figure 2.2 is an illustration of noise generation by a turbulent flow around a symmetric airfoil. It is worth mentioning that at moderate Reynolds number, it will be extremely difficult or even not possible to resolve the acoustic generation from a symmetric airfoil. The reason is that the flow is fully attached to the airfoil and flow field becomes very steady while doing unsteady flow computation. Separation starts while increasing the Reynolds number, as seen in Figure 2.2. The flow is fully attached to the airfoil until half of the airfoil chord, then the boundary layer starts to become unstable and finally separation bubbles are generated near the trailing edge. The acoustic energy is concentrated at the trailing edge where the flow is most unstable. The figure shows a typical trailing edge noise generation. There could be more noise sources on airfoil while increasing Reynolds number or at larger angle of attacks where sepa-

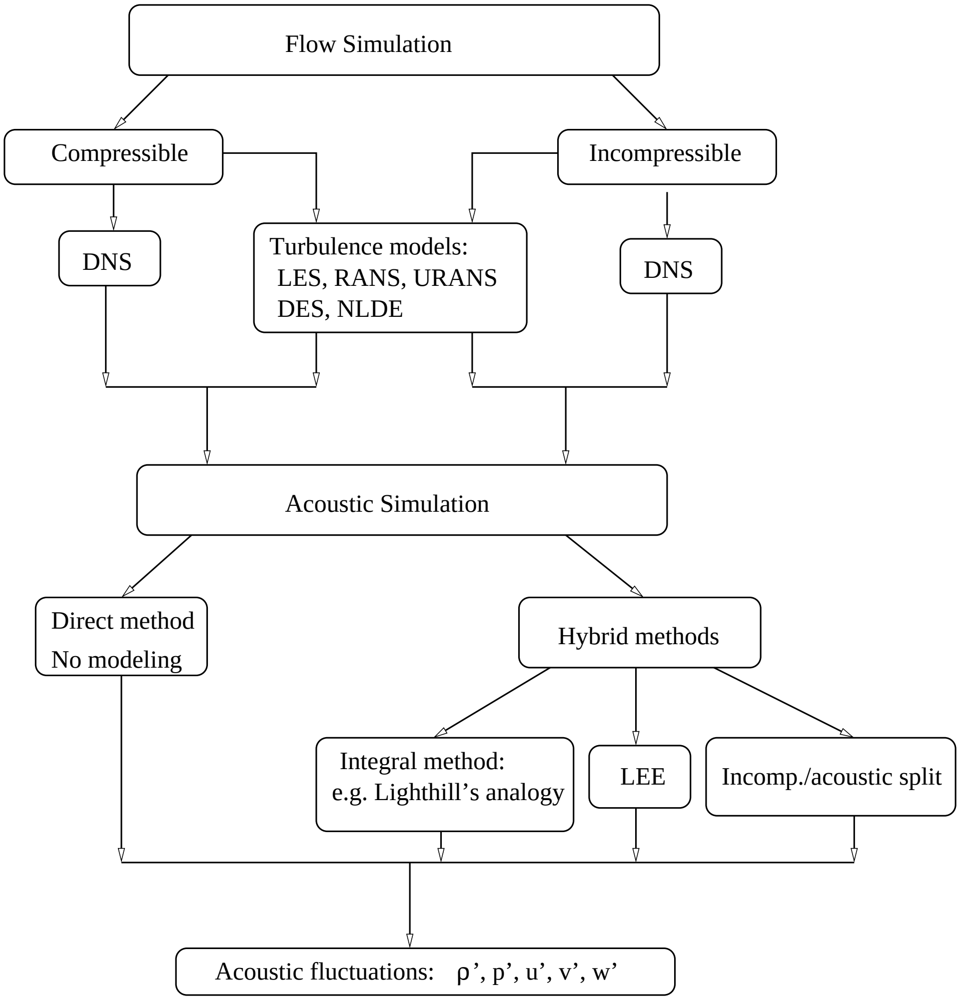

Figure 2.1: A diagram of CAA methods.

ration point moves towards leading edge.

Challenges exist while resolving such flow and acoustic fields. First, from a flow point of view, since it is the unsteady flow that makes noise the turbulent flow structure should be well represented by the flow simulation. The unsteady Reynolds averaged Navier-Stokes (URANS) method is normally not always good enough because small turbulence structures are difficult to capture due to the time average. Other models such as large eddy simulation (LES) or detached eddy simulation (DES) are better to model small turbulent structures. But still the uncertainty of turbulence model will effect acoustic prediction, this is an important issue for future discussion. Secondly, the acoustic wave length at low Mach number has large disparities. Unfortunately, the small waves or waves at high frequencies are often of our interest. On the other hand, the disparity of magnitudes of flow and acoustic solutions requires high accuracy of acoustic simulation. Hybrid methods have the advantages of separating flow and acoustic simulations where numerical accuracy for flow simulation is less critical. The numerical accuracy of flow simulation was studied by Hixon et al. [15]. In their study, four solvers with different numerical accuracies are used for both flow and acoustic simulations. The difference in mean flow simulated with sixth-order and second-order schemes is within 0.1%. For acoustic simulations the second-order scheme obtains a very different solution from the high accuracy schemes and even produced spurious acoustic waves. Further, there is a need of a large computational domain and use of non-reflecting boundary conditions since we can not solve the problem with an infinitely large domain. Finally, the required computational time for acoustic computation is much longer than for flow simulations. The time step for acoustic calculation is much smaller and depends on the Mach number. Also, the spectral solution is very important which requires a long time series result.

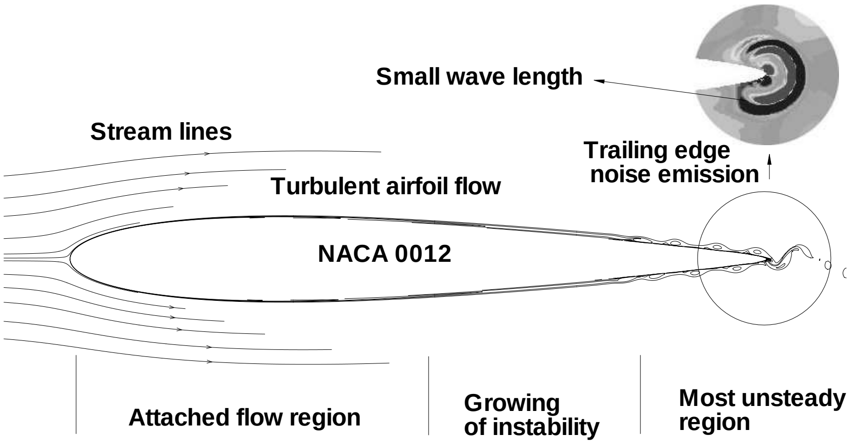

Figure 2.2: Example of noise generation due to unsteady flow.

2.2 Lighthill's acoustic analogy

The comprehensive study of computational aeroacoustics was started in the early 1950s when Lighthill [3] developed his acoustic analogy with the purpose of reducing noise from jet engines. The acoustic equation is derived from the momentum and continuity equations. Equations of arbitrary fluid motion can be rewritten by grouping the nonlinear terms into a source term which is the so-called Lighthill stress tensor. The wave equation is described by a scalar partial differential equation (PDE) with fluctuating density as the only primary variable.

The mass and momentum equations for compressible fluid motion without external forces are written as

$$\begin{aligned} \frac{\partial \rho}{\partial t} + \frac{\partial}{\partial x_i}(\rho u_i) &= 0 && (2.1) \\ \frac{\partial}{\partial t}(\rho u_i) + \frac{\partial}{\partial x_j}(\rho u_i u_j) &= -\frac{\partial p}{\partial x_i} + \frac{\partial \tau_{ij}}{\partial x_j} && (2.2) \end{aligned}$$

where ρ, u, p are fluid density, velocity and pressure, respectively. The viscous stress tensor is

$$\tau_{ij} = \mu \left[\frac{\partial u_i}{\partial x_j} + \frac{\partial u_j}{\partial x_i} - \frac{2}{3} \left(\frac{\partial u_k}{\partial x_k} \right) \delta_{ij} \right] \tag{2.3}$$

where δ_{ij} is the Kronecker symbol, $\delta_{ij} = 1$ for $i = j$ otherwise 0. Combining the mass and momentum Equations (2.1) and (2.2), Lighthill's analogy can be found as

$$\frac{\partial^2 \rho'}{\partial t^2} - c_0^2 \frac{\partial^2 \rho'}{\partial x_i^2} = \frac{\partial^2 T_{ij}}{\partial x_i \partial x_j} \tag{2.4}$$

where the fluctuation density is equivalent to $\rho' = \rho - \rho_0$ with ρ_0 denotes the fluid density at rest. And the Lighthill stress tensor is expressed as

$$T_{ij} = \rho u_i u_j + \left((p - p_0) - c_0^2(\rho - \rho_0) \right) \delta_{ij} - \tau_{ij} \tag{2.5}$$

where μ is the viscosity and the pressure $p = \rho RT$, R is the gas constant and T is the temperature.

The viscosity is often neglected in case of low Mach number air flow. Therefore the Lighthill's stress tensor is much simplified by ignoring the viscous stress tensor τ_{ij}. If the right hand side of Equation (2.4) is known from flow simulation, the Lighthill's equation can be written in an integral form:

$$4\pi c_0^2 \rho' = \frac{\partial^2}{\partial x_i \partial x_j} \int_{\infty} \frac{T_{ij}(\mathbf{y}, t')}{\mid \mathbf{x} - \mathbf{y} \mid} d\Omega(\mathbf{y}) \tag{2.6}$$

where $\mathbf{x}$ is the observation point and $\mathbf{y}$ is the source location, Ω is the integration domain. The acoustic source term T_{ij} is related to the source position and the retarded time $t' = t - |\mathbf{x} - \mathbf{y}|/c_0$. The acoustic source term can be obtained from an unsteady flow solution based on incompressible or compressible equations. The noise source region needs to be acoustically compact and no significant source close to computational boundary.

2.3 Ffowcs Williams and Hawkings' equation

The Lighthill's theory was further developed by Ffowcs Williams & Hawkings [5] and Farassat & Brentner [16, 17] who introduced the effect from arbitrary moving surfaces. This became a more generalized approach for noise prediction based on Lighthill's acoustic analogy. The Ffowcs Williams and Hawkings' integral approach has some resemblance with the Kirchhoff's theory [18] which was proposed in 1882. In Kirchhoff's theory the wave equation is represented by a surface integral and was originally applied for light diffraction and electromagnetic problems. An extension of Kirchhoff's theory for sound propagation was proposed by Farassat and Myers [19]. The attempt of Ffowcs Williams and Hawkings was to formulate the governing equations using generalized Green's function to express the solution of the wave equation. The resulted wave equation has both a surface source term and a volume source term on the right hand side.

The surface of the solid body divides the computational domain into two parts. The moving or stationary surface S is defined by a function $f(\mathbf{x}, t)$ which is zero on the surface, negative inside the surface and positive in the surrounding fluid, see also [20]. The Ffowcs Williams and Hawkings' equation can be written in the form followed by Brentner and Farassat [17], as shown in Equation (2.7). The same authors have also shown examples of helicopter noise [21, 22] by using the equation

$$\begin{aligned}\Box^2 p'(\mathbf{x}, t) \quad = \quad & \frac{\partial^2}{\partial x_i \partial x_j}\left[T_{ij} H(f)\right] - \frac{\partial}{\partial x_i}\left\{\left[P_{ij}\hat{n}_j + \rho u_i (u_n - v_n)\right]\delta(f)\right\} \\ & + \frac{\partial}{\partial t}\left\{\left[\rho_0 v_n + \rho(u_n - v_n)\right]\delta(f)\right\} \qquad (2.7)\end{aligned}$$

where the wave operator is written as $\Box^2 = [(1/c_0^2)(\partial^2/\partial t^2)] - \nabla^2$, $p'(\mathbf{x}, t)$ is the acoustic pressure at observer position, the function $H(f) = 0$ for $f < 0$ and $H(f) = 1$ for $f > 0$, $P_{ij} = p'\delta_{ij}$ for inviscid fluid, $\hat{n}_i$ is the unit vector pointing out of surface, u_i is fluid velocity component, $u_n = u_i\hat{n}_i$ is the fluid velocity normal to the surface, v_n is the normal velocity on the surface, ρ and ρ_0 are fluid density and density at rest, and $\delta(f)$ is the Dirac delta function.

The integral representation of the acoustic equation is followed by [22]

$$p'(\mathbf{x},t) = p'_T(\mathbf{x},t) + p'_L(\mathbf{x},t) + p'_Q(\mathbf{x},t). \tag{2.8}$$

Equation (2.8) separates the noise sources into three parts, namely p'_T, p'_L and p'_Q which denote the thickness noise component (monopoles surface source), the loading noise component (dipoles surface source) and the quadrupole volume noise component, respectively. Their integral forms are

$$\begin{aligned} 4\pi p'_T(\mathbf{x},t) = & \int_{f=0} \left[\frac{\rho_0(\dot{U}_n + U_{\dot{n})}}{r(1-M_r)^2} \right]_{ret} dS \\ & + \int_{f=0} \left[\frac{\rho_0 U_n (r\dot{M}_r + c_0(M_r - M^2))}{r^2(1-M_r)^3} \right]_{ret} dS \end{aligned} \tag{2.9}$$

$$\begin{aligned} 4\pi p'_L(\mathbf{x},t) = & \frac{1}{c_0} \int_{f=0} \left[\frac{\dot{L}_r}{r(1-M_r)^2} \right]_{ret} dS \\ & + \int_{f=0} \left[\frac{L_r - L_M}{r^2(1-M_r)^2} \right]_{ret} dS \\ & + \frac{1}{c_0} \int_{f=0} \left[\frac{L_r (r\dot{M}_r + c_0(M_r - M^2))}{r^2(1-M_r)^3} \right]_{ret} dS \end{aligned} \tag{2.10}$$

where a dot over a symbol indicates time differentiation. M is the Mach number, $M_r = M_i \hat{r}_i$ is the Mach number of the sources in radiation direction. In Equation (2.9) and (2.10), $U_n = U_i \hat{n}$, $L_r = L_i \hat{r}_i$ and $L_M = L_i M_i$ where $U_i = [1 - (\rho/\rho_0) v_i + \rho u_i/\rho_0]$ and $L_i = P_{ij}\hat{n}_j + \rho u_i (u_n - v_n)$. In the equations, the subscript ret indicates the retarded time $t' = t - r/c_0$ as mentioned earlier. The quadrupole component is often neglected in case the noise sources are mainly generated at surfaces, it is able to be determined by various methods, such as [23, 24].

2.4 Curle's equation

The acoustic analogy between Curle and Ffowcs Williams and Hawkings are very similar since both of the approaches considered the presence of solid bodies. However, it is worth mentioning the work done by Curle [4] since his theory was developed earlier than Ffowcs Williams and Hawkings but without considering the effect of surface motion. The method was also widely used for many applications, such as noise generation from open cavities [25, 26] and flow induced cylinder noise in a uniform inflow [27, 8]. In

[27], Curle's formulation is compared analytically and numerically with a formulation based on Green's function. Inoue et al. [8] compared acoustic results at a Reynolds number of 150 using DNS and Curle's approach where the results showed good agreement.

The starting point of deriving Curle's equation is similar to the one by Ffowcs Williams and Hawkings. Assume the fluid is divided by the stationary solid body S and the fluid is at rest at infinity and at surface S. Curle wrote the solution of Lighthill's equation with surface and volume sources as

$$p'(\mathbf{x},t) = p'_S(\mathbf{x},t) + p'_V(\mathbf{x},t) \tag{2.11}$$

where the surface term is

$$p'_S(\mathbf{x},t) = \frac{1}{4\pi}\int_S l_i n_j \left[\frac{\dot{p}\delta_{ij} - \dot{\tau}_{ij}}{c_0 r} + \frac{p\delta_{ij} - \tau_{ij}}{r^2}\right] dS(\mathbf{y}) \tag{2.12}$$

and the volume source is

$$p'_V(\mathbf{x},t) = \frac{1}{4\pi}\int_V \left[\frac{l_i l_j}{c_0^2 r}\ddot{T}_{ij} + \frac{3l_i l_j - \delta_{ij}}{c_0 r^2}\dot{T}_{ij} + \frac{3l_i l_j - \delta_{ij}}{r^3}T_{ij}\right] dV(\mathbf{y}) \tag{2.13}$$

where variables such as $\mathbf{y}, r, \tau_{ij}$ are the same as defined in previous sections and l_i is the unit vector pointing out from the source to the observer.

2.5 Direct simulation

Direct simulation is defined as the numerical approach of solving the NS equations without modeling or approximations. DNS requires use of sufficient high numerical accuracy and reasonably fine mesh, the technique is able to describe all details of flow and associated sound. Therefore the method is straightforward and it provides a possibility of comprehensive study of aerodynamic sound phenomena. The disadvantage of the method is the Reynolds number limitation. The computational cost of direct simulation is large, and previous studies have seen limited to relatively simple flows problems and ideal cases.

Sound generation from a circular cylinder at a low Reynolds number was proposed by Inoue et al. [8] and general agreement was found by comparing with acoustic analogy. Sound generation from a compressible co-rotating vortex pair was studied by Mitchell et al. [28, 29] using DNS. The sound frequency was found at twice of the rotational frequency. Studies at modest high Reynolds number are direct computations of sound generation from jet

[30, 31], turbulent vortex ring [32], turbulent cavity flow [33].

Assuming that very small turbulence scales have less effect on sound generation, the cost of direct simulation of compressible equation can be reduced by introducing turbulence models. Turbulence models such as LES and URANS can be used in the full or a part of the domain and sound field is still computed directly. Noise from a 3D airfoil at a Reynolds number of 500 000 was computed by Marsden et al.[34] in a relatively small computational domain. Another example concerns sound generation from a wind turbine tip [35] where the simulation was carried out with 320 million computational cells on the Earth Simulator.[1]

2.6 Linearized Euler equations with source terms

In this section, acoustic analogy combined with linearized euler equations (LEE) is introduced based on Bogey and Bailly [36, 37, 38, 39], which is an alternative method of simulating aerodynamic sound. The background for proposing this method is due to the drawbacks of direct simulation and acoustic analogy. Direct simulation is known to be expensive for flows of practical interest at high Reynolds numbers and Mach numbers. To solve the Lighthill's acoustic equation, one needs to find a compact region containing source terms and then evaluating integrals around the domain. However, Lighthill's equation is the representation of the source terms where the effect of mean flow to acoustic field is considered [40, 38]. This makes it difficult to take into account all the effects where the source region is not only the compact turbulence region [38] but also containing all acoustic-flow interactions. As stated by Bogey et al., the velocity field used to build all source terms needs to be compressible.

The source term based on the previous work by Bailly et al.[39] is combined with a stochastic velocity field [36]. The expression of the velocity source terms is obtained by directly solving the unsteady compressible NS equations. Consider an unsteady flow with mean density $\bar{\rho}$, velocities $\bar{u_1}, \bar{u_2}$ and pressure $\bar{p}$, the small perturbation above the mean quantities are governed by the LEE [36]

$$\frac{\partial U}{\partial t} + \frac{\partial E}{\partial x_1} + \frac{\partial F}{\partial x_2} + H = S \tag{2.14}$$

where the vectors U, E, F, H and S are given as follows

---

[1] The Earth Simulator (ES) is one of the world fastest supercomputer system of today.

$$U = \begin{pmatrix} \rho' \\ \bar{\rho} u_1' \\ \bar{\rho} u_2' \\ p' \end{pmatrix}, E = \begin{pmatrix} \rho' \bar{u}_1 + \bar{\rho} u_1' \\ \bar{u}_1 \bar{\rho} u_1' + p' \\ \bar{u}_1 \bar{\rho} u_2' \\ \bar{u}_1 p' + \gamma \bar{p} u_1' \end{pmatrix} F = \begin{pmatrix} \rho' \bar{u}_2 + \bar{\rho} u_2' \\ \bar{u}_2 \bar{\rho} u_1' \\ \bar{u}_2 \bar{\rho} u_2' + p' \\ \bar{u}_2 p' + \gamma \bar{p} u_2' \end{pmatrix},$$

$$H = \begin{pmatrix} 0 \\ (\bar{\rho} u_1' + \rho' \bar{u}_1) \frac{\partial \bar{u}_1}{\partial x_1} + (\bar{\rho} u_2' + \rho' \bar{u}_2) \frac{\partial \bar{u}_1}{\partial x_2} \\ (\bar{\rho} u_1' + \rho' \bar{u}_1) \frac{\partial \bar{u}_2}{\partial x_1} + (\bar{\rho} u_2' + \rho' \bar{u}_2) \frac{\partial \bar{u}_2}{\partial x_2} \\ (\gamma - 1) p' \nabla \cdot \bar{\mathbf{u}} - (\gamma - 1) \mathbf{u}' \cdot \nabla \tilde{p} \end{pmatrix}, S = \begin{pmatrix} 0 \\ S_1 - \bar{S}_1 \\ S_2 - \bar{S}_2 \\ 0 \end{pmatrix}. \quad (2.15)$$

The term H is zero for uniform mean flow. The right hand side is the source term S where $S_i = -\frac{\partial \rho u_i' u_j'}{\partial x_j}$ and $\overline{S_i} = -\overline{\frac{\partial \rho u_i' u_j'}{\partial x_j}}$.

Test cases have shown that LEE is able to provide reasonable solutions for aerodynamic noise. However, as discussed by Colonius and Lele [41, 48], the numerical difficulty of solving the LEE is due to the fact that the equations admit non-trivial instability waves to appear in the solutions of the homogenous equations. These instability waves will effect both the source region and computational boundaries.

2.7 Incompressible/acoustic splitting method

In this section, the incompressible/acoustic splitting method, sometimes also called acoustic/viscous splitting technique or expansion about incompressible flow (EIF) is introduced. This approach was first proposed by Hardin and Pope [1] as an alternative to full-blown direct simulations of the sound field. The acoustic equations are fully non-linear without the artifice of analog approaches.

The incompressible/acoustic splitting method proposed by Hardin and Pope is a novel approach which is distinct from previously introduced methods. The first step of the approach is to solve the unsteady incompressible flow where the density is a constant. Secondly, a hydrodynamic density correction to the constant incompressible density is calculated from the incompressible pressure fluctuations. Finally, the compressible flow solution is obtained by superimposing the perturbations to incompressible flow.

Consider a viscous compressible flow in the absence of external forces. The fluid motion is governed by the complete set of compressible NS equations [42]

$$\begin{aligned}
\frac{\partial \rho}{\partial t} + \frac{\partial}{\partial x_i}(\rho u_i) &= 0 && (2.16)\\
\frac{\partial}{\partial t}(\rho u_i) + \frac{\partial}{\partial x_j}(\rho u_i u_j + p_{ij}) &= 0 && (2.17)\\
p &= p(\rho, S) && (2.18)\\
T\frac{DS}{Dt} = c_p\frac{DT}{Dt} - \frac{\beta T}{\rho}\frac{Dp}{Dt} &= \phi + \frac{1}{\rho}\frac{\partial}{\partial x_i}\left(k\frac{\partial T}{\partial x_i}\right) && (2.19)
\end{aligned}$$

where ρ, p, T and S are density, pressure, temperature and entropy per unit mass, respectively. c_p, β, k and ϕ are the specific heat capacity at constant pressure, the coefficient of thermal expansion, the coefficient of thermal conductivity and the viscous dissipation respectively. The velocity u_i is defined in a reference coordinate system x_i and as defined in Lighthill's equation,

$$p_{ij} = p\delta_{ij} - \mu\left[\frac{\partial u_i}{\partial x_j} + \frac{\partial u_j}{\partial x_i} - \frac{2}{3}\left(\frac{\partial u_k}{\partial x_k}\right)\delta_{ij}\right] \tag{2.20}$$

where μ is the dynamic viscosity and δ_{ij} is the Kronecker function.

Consider the incompressible flow with a constant density ρ_0. The incompressible solution is written as

$$\begin{aligned}
\frac{\partial U_i}{\partial t} + \frac{\partial (U_i U_j)}{\partial x_j} &= -\frac{1}{\rho_0}\frac{\partial P}{\partial x_i} + \nu\frac{\partial^2 U_i}{\partial x_i \partial x_j} && (2.21)\\
\frac{\partial U_i}{\partial x_i} &= 0 && (2.22)
\end{aligned}$$

where $P(x_i, t)$ and $U_i(x_i, t)$ are time dependent unsteady incompressible pressure and velocity components. The pressure change for the ambient pressure p_0 is $dp = P - p_0$. Returning to the compressible Equation (2.18) and differentiating both sides of this equation, we then get a new relation as follows

$$dp = \left(\frac{\partial p}{\partial \rho}\right)_S d\rho + \left(\frac{\partial p}{\partial S}\right)_\rho dS. \tag{2.23}$$

Since the sound speed is defined as $c = \sqrt{(\partial p/\partial \rho)_S}$, the pressure change can be expressed as

$$dp = c^2 d\rho + \left(\frac{\partial p}{\partial S}\right)_\rho dS. \tag{2.24}$$

This relation tells that it is the density and entropy changes that are responsible for pressure changes. The next is to determine which of the two terms is the most important. The formulation of entropy change already exists as part of the compressible Equations (2.19) given by Batchelor [42]. As noted by Batchelor that in terms of solving the magnitude of pressure fluctuation the flow can be assumed to be isentropic. The viscous and heat conduction have only little effect on the pressure magnitude, more effects are normally to the pressure distributions. Therefore, these effect are slow on an acoustic timescale. The time-averaged incompressible pressure distribution is given

$$\bar{P}(x_i) = \lim_{T\to\infty} \frac{1}{T} \int_0^T P(x_i, t)dt. \tag{2.25}$$

The pressure fluctuation in time can be proved to be a function of density fluctuations. The incompressible pressure can be divided into two parts as

$$p(\rho, S) = p'(\rho) + \bar{P}(S) \tag{2.26}$$

where the time-averaged pressure $\bar{P}$ is related to the entropy effect and the fluctuating pressure is assumed isentropic. The time derivative of the total pressure p results

$$\frac{\partial p}{\partial t} = \frac{\partial p'}{\partial t} = \frac{dp'}{d\rho}\frac{\partial \rho}{\partial t} = \left(\frac{\partial p}{\partial \rho}\right)_S \frac{\partial \rho}{\partial t} = c^2 \frac{\partial \rho}{\partial t}. \tag{2.27}$$

To derive the acoustic equations, the compressible variables are first decomposed into two parts, the mean flow and the perturbed flow.

$$u_i = U_i + u_i' \tag{2.28}$$

$$p = P + p' \tag{2.29}$$

$$\rho = \rho_0 + \rho_1 + \rho' \tag{2.30}$$

where u_i and p' are velocity and pressure perturbations, ρ' is the perturbed density about the corrected incompressible density $\rho_0 + \rho_1$, the hydrodynamic density correction ρ_1 to the ambient density ρ_0 is given as

$$\rho_1(x_i,t) = \frac{P(x_i,t) - \bar{P}(x_i)}{c_0^2} \tag{2.31}$$

where P is the incompressible pressure and $\bar{P}$ is the time-averaged incompressible pressure distribution. Inserting Equations (2.28-2.30) into (2.16), (2.17) and (2.27) and neglecting the effect of viscosity on the fluctuations, the non-linear equations set for acoustic perturbations is obtained as

$$\frac{\partial \rho'}{\partial t} + \frac{\partial f_i}{\partial x_i} = -\frac{\partial \rho_1}{\partial t} - U_i \frac{\partial \rho_1}{\partial x_i} \tag{2.32}$$

$$\frac{\partial f_i}{\partial t} + \frac{\partial}{\partial x_j}[f_i(U_j + u'_j) + (\rho_0 + \rho_1)U_i u'_j + p'\delta_{ij}] = -\frac{\partial(\rho_1 U_i)}{\partial t} - U_j \frac{\partial(\rho_1 U_i)}{\partial x_j} \tag{2.33}$$

$$\frac{\partial p'}{\partial t} - c^2 \frac{\partial \rho'}{\partial t} = c^2 \frac{\partial \rho_1}{\partial t} \tag{2.34}$$

where $f_i = (\rho_0 + \rho_1)u'_i + \rho'(U_i + u'_i)$ and sound speed is calculated by

$$c^2 = \frac{\gamma p}{\rho} = \frac{\gamma(P + p')}{\rho_0 + \rho_1 + \rho'} \tag{2.35}$$

where $\gamma = 1.4$ is the specific heat ratio for standard atmospheric condition. Here the sound speed needs to be computed at each iteration based on the known pressure and velocity field. Equations (2.32)-(2.34) are the resulting nonlinear acoustic equations proposed by Hardin and Pope [1] with a closed set of five equations for five unknowns. The acoustic equations are solved at each iteration after the incompressible solutions are obtained. It is noticed that different numerical schemes can be used for acoustic and incompressible solvers which provides the freedom to treat them with different accuracy. The set of equations were applied for sound generation from a pulsating sphere and cavity flow [1, 43, 46].

A careful examination of the equations was done by Shen and Sørensen [2] who argued that the equations contain no sources. If one introduces new variables $\bar{\rho} = \rho_1 + \rho'$ and $\bar{f}_i = \rho u'_i + \bar{\rho} U_i$ instead of using ρ' and f_i. The Hardin and Pope's acoustic equations are reconstructed into

$$\begin{aligned}
\frac{\partial \bar{\rho}}{\partial t} + \frac{\partial \bar{f}_i}{\partial x_i} &= 0 \qquad (2.36)\\
\frac{\partial \bar{f}_i}{\partial t} + \frac{\partial}{\partial x_j}[\bar{f}_i(U_j + u'_j) + \rho_0 U_i u'_j + p'\delta_{ij}] &= 0 \qquad (2.37)\\
\frac{\partial p'}{\partial t} - c^2 \frac{\partial \bar{\rho}}{\partial t} &= 0 \qquad (2.38)
\end{aligned}$$

where no source terms were contained in the systems. Since the introduction of a hydrodynamic density correction did not contain new information therefore there it is not necessary to do the correction. The remedy of the original system is to use a new decomposition for the compressible equations:

$$\begin{aligned}
u_i &= U_i + u'_i \qquad (2.39)\\
p &= P + p' \qquad (2.40)\\
\rho &= \rho_0 + \rho' \qquad (2.41)
\end{aligned}$$

where the density correction is omitted. Insert them into compressible equations and ignore the viscous terms we have a modified acoustic formulation

$$\begin{aligned}
\frac{\partial \rho'}{\partial t} + \frac{\partial f_i}{\partial x_i} &= 0 \qquad (2.42)\\
\frac{\partial f_i}{\partial t} + \frac{\partial}{\partial x_j}[f_i(U_j + u'_j) + \rho_0 U_i u'_j + p'\delta_{ij}] &= 0 \qquad (2.43)\\
\frac{\partial p'}{\partial t} - c^2 \frac{\partial \rho'}{\partial t} &= -\frac{dP}{dt} \qquad (2.44)
\end{aligned}$$

where $f_i = \rho u'_i + \rho' U_i$. The system is closed by introducing the of sound speed as

$$c^2 = \frac{\gamma p}{\rho} = \frac{\gamma(P + p')}{\rho_0 + \rho'}. \qquad (2.45)$$

This new formulation by Shen and Sørensen was used in the present study. Some examples of flow and noise computations will be shown in the second part of this thesis. Previous analysis on cylinder and airfoil noise have shown good results by Shen and Sørensen, see [9, 10, 11]. The present study is considered as an extension of their previous work by introducing high-order finite difference schemes.

The 3D acoustic Equations (2.42)-(2.44) can be rewritten in vector form such that

$$\frac{\partial Q}{\partial t}+\frac{\partial E}{\partial x}+\frac{\partial F}{\partial y}+\frac{\partial G}{\partial z}=S \tag{2.46}$$

where matrices Q, E, F, G and S are

$$Q=\begin{pmatrix}\rho' \\ \rho u'+\rho' U \\ \rho v'+\rho' V \\ \rho w'+\rho' W \\ p'\end{pmatrix}, E=\begin{pmatrix}\rho u'+\rho' U \\ \rho(2Uu'+u'^2)+\rho' U^2+p' \\ \rho(Vu'+Uv'+u'v')+\rho' UV \\ \rho(Wu'+Uw'+u'w')+\rho' UW \\ c^2(\rho u'+\rho' U)\end{pmatrix},$$

$$F=\begin{pmatrix}\rho v'+\rho' V \\ \rho(Vu'+Uv'+u'v')+\rho' UV \\ \rho(2Vv'+v'^2)+\rho' V^2+p' \\ \rho(Vw'+Wv'+v'w')+\rho' VW \\ c^2(\rho v'+\rho' V)\end{pmatrix},$$

$$G=\begin{pmatrix}\rho w'+\rho' W \\ \rho(Wu'+Uw'+u'w')+\rho' UW \\ \rho(Wv'+Vw'+v'w')+\rho' VW \\ \rho(2Ww'+w'^2)+\rho' W^2+p' \\ c^2(\rho w'+\rho' W)\end{pmatrix}, S=\begin{pmatrix}0 \\ 0 \\ 0 \\ 0 \\ -\frac{\partial P}{\partial t}\end{pmatrix}. \tag{2.47}$$

A similar vector formulation has been given by Ekaterinaris [44, 45] who performed 2D aeroacoustic simulations on a co-rotating vortex pair and the results fits well with analytic solution. The vector formulation can be alternatively written in a form with primitive variables as shown by Ekaterinaris [44, 45]. Such a formulation can be seen in Appendix A where the 3D acoustic equations of Shen and Sørensen are written in a form of primitive variables.

2.8 Summary

A few commonly used techniques of solving flow generated noise have been introduced in this chapter: (1) acoustic analogy combined with turbulence models when flow is turbulent; (2) direct simulation of compressible equations, turbulence models can be applied in part of or full computational domain; (3) the approaches solving systems of equations, the LEE(with source terms from acoustic analogy) and (4) incompressible/acoustic splitting methods. Generally, the large length scale difference for low Mach number flows makes direct simulation of sound very difficult, while hybrid methods are ideal for today's computer power. Hybrid methods based on

Lighthill's theory are more like postprocessing of flow field. The incompressible/acoustic splitting method is the direction toward direct simulation of sound generation where compressible equations are solved in two steps: the incompressible flow part and acoustic part. The computational cost of the splitting technique is in between the direct method and acoustic analogy and the only assumption made is the neglect of viscosity which is nature for sound propagation in the atmosphere.

Some recent reviews on CAA can be found by Wells et al. [47], Wang et al. [49] and Colonius et al. [41, 48].

Chapter 3

Numerical study

Some essential details of numerical issues for CAA are presented in this chapter. The issues arise from a host of difficulties involved when solving flow generated noise. Small amplitude and large disparity of wavelengths are the basic characteristics of sound waves. High-order spatial and temporal numerical schemes are used to minimize numerical errors, e.g., little attenuation and distortion of waves after travelling for a long distance. Together with high-order schemes, sufficient number of grid points need to be provided to resolve waves at given wavelengths, see Figure 3.1 for a schematic diagram of numerical features. For a given wave, a minimum number of mesh points per wavelength is required [52] depending on the accuracy of numerical scheme. The use of high-order schemes make it favorable to use fewer grid points per wavelength and still achieve the desired resolution. Non-physical waves resulting from centered schemes and wall boundaries needs to be suppressed at each time iteration. In some cases, the solutions diverge quickly without a suitable filter scheme. Only high-order filter schemes are allowed to be used since physical waves can easily be deteriorated by low-order filters after some thousand iterations. In some cases, a damping zone can be designed together with filtering techniques, see illustration in Figure 3.1. If the vortical disturbance near the out boundary is still too strong, the damping zone can effectively absorb most of the energy and decrease the amplitude of vortical waves before they reach the outer boundary. Boundary formulation and numerical schemes near boundary are also discussed which are issues relate to the numerical stability. The requirement for the radiation and outflow boundary conditions are quite simple, that is no reflection of acoustic waves back to the computational domain. However, all numerical boundary conditions are reflective and what we can do is to minimize the effect of reflection as much as possible. It is very often that the computational grids are stretched such that they are coarser near outer domain which automatically smooth out waves. Most of the issues discussed below are highly relevant for our present study which were implemented into the aeroacoustic solver. The over all solver structure is discussed in the final section of this chapter.

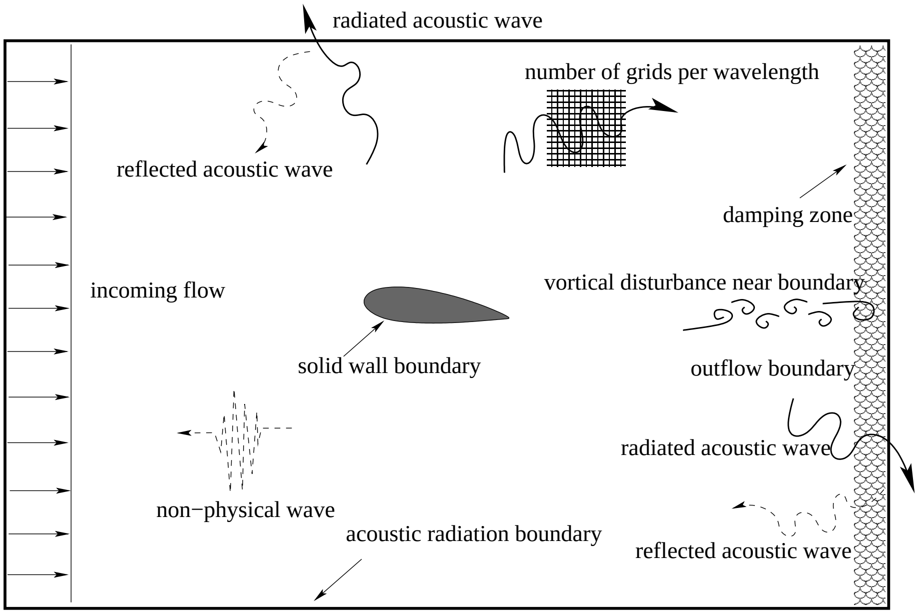

Figure 3.1: Numerical issues involved for solving flow generated noise.

3.1 Spatial discretization

One of the most important issues of CAA is the numerical discretization methods. In CAA simulations, a large number of grid points and small time steps are typically required. High-order schemes are thus commonly used for realistic CAA simulations to reduce the number of grid points per wavelength. The numerical schemes are usually originated from traditional schemes and further developed for CAA problems. Among those schemes, Dispersion-Relation-Preserving (DRP)[12] schemes and compact schemes [13, 14] are discussed in detail and these two schemes are used in the present study.

3.1.1 High-order explicit schemes and the optimizations

The idea of using a finite-difference representation for derivatives can be introduced by a weighted summation of the value at its neighboring points. For sufficient small but finite Δx, a standard central difference scheme with a $(2N+1)$-point stencil can be written as

$$\frac{\partial f}{\partial x}(x) \approx \frac{1}{\Delta x} \sum_{j=-N}^{N} a_j f(x + j\Delta x) \tag{3.1}$$

The standard way of determining the coefficients is two steps: the first step is to perform Taylor expansion at $x = 0$ of each point f_i where $i \in [-N, N]$; the second step is to eliminate high-order terms obtained from Taylor series such that the maximum accuracy of $2N^{th}$-order is obtained. An example of using Taylor expansion at each point using `Mathematica` is given in Figure 3.2.

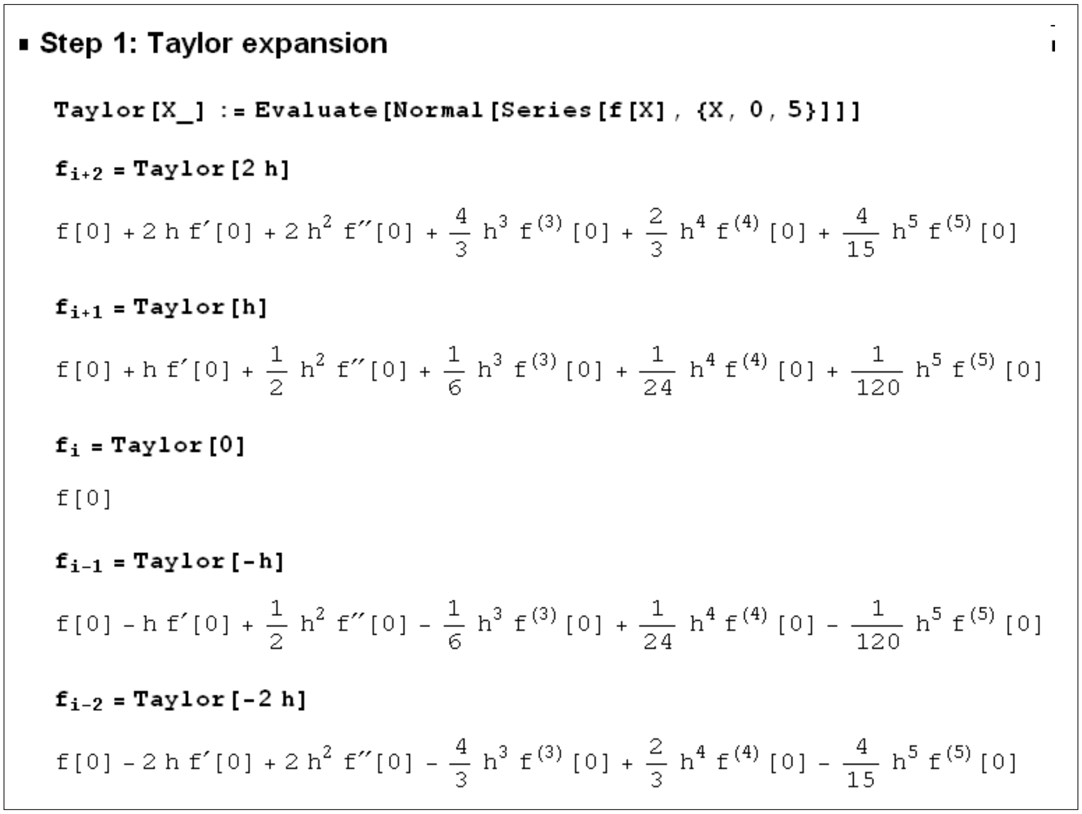

- **Step 1: Taylor expansion**

```
Taylor[X_] := Evaluate[Normal[Series[f[X], {X, 0, 5}]]]
```

f_{i+2} = Taylor[2 h]

$$f[0] + 2\,h\,f'[0] + 2\,h^2\,f''[0] + \frac{4}{3}\,h^3\,f^{(3)}[0] + \frac{2}{3}\,h^4\,f^{(4)}[0] + \frac{4}{15}\,h^5\,f^{(5)}[0]$$

f_{i+1} = Taylor[h]

$$f[0] + h\,f'[0] + \frac{1}{2}\,h^2\,f''[0] + \frac{1}{6}\,h^3\,f^{(3)}[0] + \frac{1}{24}\,h^4\,f^{(4)}[0] + \frac{1}{120}\,h^5\,f^{(5)}[0]$$

f_i = Taylor[0]

$$f[0]$$

f_{i-1} = Taylor[-h]

$$f[0] - h\,f'[0] + \frac{1}{2}\,h^2\,f''[0] - \frac{1}{6}\,h^3\,f^{(3)}[0] + \frac{1}{24}\,h^4\,f^{(4)}[0] - \frac{1}{120}\,h^5\,f^{(5)}[0]$$

f_{i-2} = Taylor[-2 h]

$$f[0] - 2\,h\,f'[0] + 2\,h^2\,f''[0] - \frac{4}{3}\,h^3\,f^{(3)}[0] + \frac{2}{3}\,h^4\,f^{(4)}[0] - \frac{4}{15}\,h^5\,f^{(5)}[0]$$

Figure 3.2: Taylor expansion.

We require that the exact derivative f_i' is identical to the finite difference approximation as shown in Equation (3.1). The difference between the exact and the approximated derivative is the Truncation Error (TE) which represents the accuracy of the approximation. Coefficients for a fourth-order standard finite difference scheme can be determined using the script shown in Figure 3.3. The equations are set up in the manner that all terms lower than fifth-orders must vanish in the TE. Since a symmetric stencil is used, only two equations are needed for solving two unknowns.

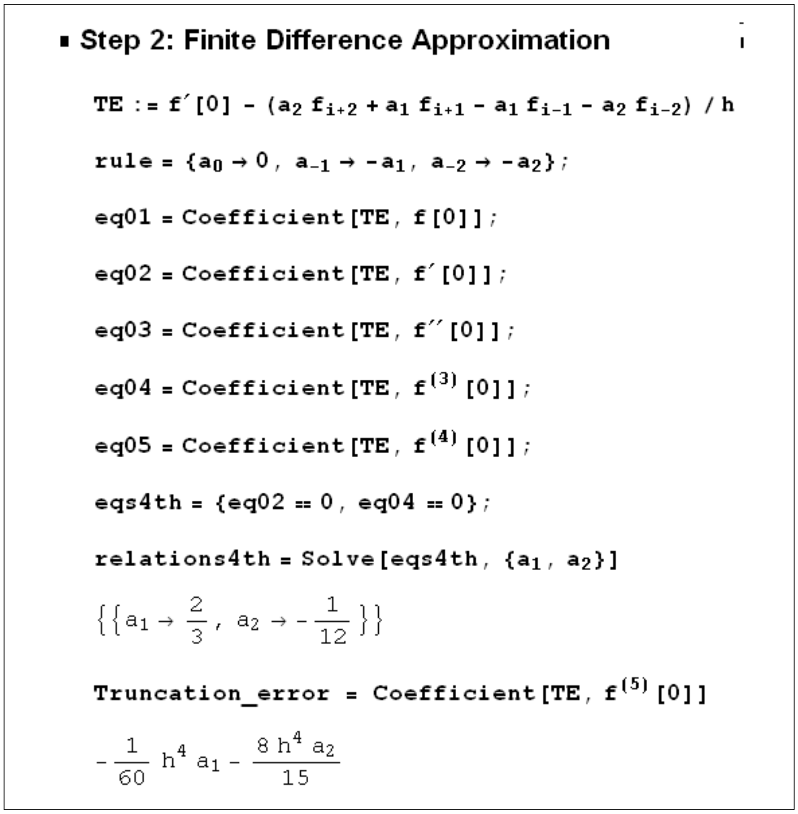

Step 2: Finite Difference Approximation

```
TE := f′[0] - (a2 fi+2 + a1 fi+1 - a1 fi-1 - a2 fi-2) / h

rule = {a0 → 0, a-1 → -a1, a-2 → -a2};

eq01 = Coefficient[TE, f[0]];

eq02 = Coefficient[TE, f′[0]];

eq03 = Coefficient[TE, f″[0]];

eq04 = Coefficient[TE, f(3)[0]];

eq05 = Coefficient[TE, f(4)[0]];

eqs4th = {eq02 == 0, eq04 == 0};

relations4th = Solve[eqs4th, {a1, a2}]
```

$$\left\{\left\{a_1 \to \frac{2}{3},\ a_2 \to -\frac{1}{12}\right\}\right\}$$

```
Truncation_error = Coefficient[TE, f(5)[0]]
```

$$-\frac{1}{60} h^4 a_1 - \frac{8 h^4 a_2}{15}$$

Figure 3.3: Finite difference approximation.

Finite difference approximation such as Equation (3.1) can be alternatively designed to have a minimal dispersion and dissipation errors. Tam and Webb [12] derived a new scheme with fourth-order accuracy using 7-point stencils. The spatial derivatives are approximated in an optimized way such that the new scheme resolves a wider range of wavenumbers which is essential for solving wave equations. In this work, following the technique of Tam and Webb, a series of optimized schemes are constructed using stencil of maximum 17 points.

As an example, here we consider the 7-point scheme which originally is of sixth-order accuracy. The optimized scheme has fourth-order accuracy which is the so called DRP scheme where a 7-point stencil is used. As seen previously in Figure 3.1, fourth-order scheme can be derived using 5-point stencil, therefore the use of 7-point stencil will give us a free parameter a_j. The value a_j is the one to be optimized and the new scheme will have less dispersion error. The starting point is still the same finite difference approximation given in Equation (3.1). By doing Fourier transformation of $f(x)$ and its inverse one gets

$$\tilde{f}(\alpha) = \frac{1}{2\pi}\int_{-\infty}^{\infty} f(x)\mathsf{e}^{-i\alpha x}dx, \qquad f(x) = \int_{-\infty}^{\infty} \tilde{f}(\alpha)\mathsf{e}^{-i\alpha x}d\alpha. \tag{3.2}$$

Applying the Fourier transformation to the finite difference approximation of Equation (3.1) we have

$$i\alpha\tilde{f} \cong \frac{1}{\Delta x}\left[\sum_{-N}^{N} a_j \mathsf{e}^{ij\alpha\Delta x}\right]\tilde{f}, \tag{3.3}$$

and after a little arrangement the relation becomes

$$\bar{\alpha}\Delta x \cong -i\left[\sum_{-N}^{N} a_j \mathsf{e}^{ij\alpha\Delta x}\right] \tag{3.4}$$

where it has to be noticed that $i = \sqrt{-1}$ and j is the index. In fact there is nothing new in Equation (3.4) except that the finite difference approximation in physical space is transformed into the wave space. In this way, the left hand side $\bar{\alpha}\Delta x$ is denoted as the modified wavenumber which is a function of exact wavenumber $\alpha\Delta x$ shown on the right hand side. One of the key issues of solving a wave problem is that the numerical solution in the resolvable wavenumber range should be as close as possible to the exact solution. In other words, the physical shape of a wave should be well represented by numerical simulations. Thus, $\bar{\alpha}\Delta x$ should be as much as possible equal to the exact wavenumber $\alpha\Delta x$. Similar as we define the truncation error, we define an integral error between $\bar{\alpha}\Delta x$ and $\alpha\Delta x$ which reads

$$E = \int_{-\eta}^{\eta} \mid \alpha\Delta x - \bar{\alpha}\Delta x \mid^2 d(\alpha\Delta x) \tag{3.5}$$

where η is the integral range with $\eta = \pi/2$ representing the full wavenumber range. Recall that we have a free parameter a_j which is used here to minimize the integral E. This is done by taking the derivative of E with respect to the only unknown a_j and force the derivative to be zero.

$$\frac{\partial E}{\partial a_j} = 0, \qquad j \in [-N, N]. \tag{3.6}$$

By now, we shall see the last procedure of deriving the wavenumber optimized scheme which is the third step after *Step* 2. The procedure of deriving a_j is shown as *Step* 3 in Figure 3.4. We see that the leading TE is accurate to order of $(h)^4$ implying fourth-order accuracy of the new 7-point scheme. Using such optimization method, schemes with higher order accuracy are also derived, optimized coefficients for up to fourteenth-order are given by Table B.1 in Appendix B.

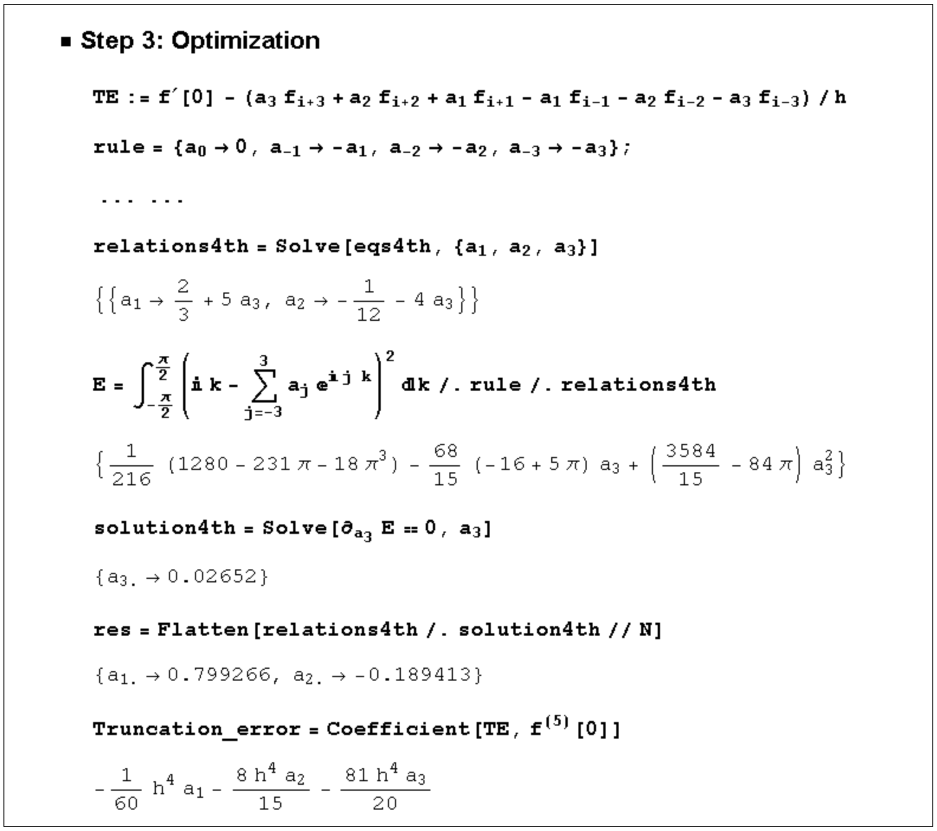

■ **Step 3: Optimization**

$$\mathbf{TE := f'[0] - (a_3\, f_{i+3} + a_2\, f_{i+2} + a_1\, f_{i+1} - a_1\, f_{i-1} - a_2\, f_{i-2} - a_3\, f_{i-3})\ /\ h}$$

$$\mathbf{rule = \{a_0 \to 0,\ a_{-1} \to -a_1,\ a_{-2} \to -a_2,\ a_{-3} \to -a_3\};}$$

... ...

$$\mathbf{relations4th = Solve[eqs4th,\ \{a_1,\ a_2,\ a_3\}]}$$

$$\left\{\left\{a_1 \to \frac{2}{3} + 5\, a_3,\ a_2 \to -\frac{1}{12} - 4\, a_3\right\}\right\}$$

$$\mathbf{E = \int_{-\frac{\pi}{2}}^{\frac{\pi}{2}} \left(i\, k - \sum_{j=-3}^{3} a_j\, e^{i\, j\, k}\right)^2 dk\ /.\ rule\ /.\ relations4th}$$

$$\left\{\frac{1}{216}\,(1280 - 231\,\pi - 18\,\pi^3) - \frac{68}{15}\,(-16 + 5\,\pi)\, a_3 + \left(\frac{3584}{15} - 84\,\pi\right) a_3^2\right\}$$

$$\mathbf{solution4th = Solve[\partial_{a_3} E == 0,\ a_3]}$$

$$\{a_{3.} \to 0.02652\}$$

$$\mathbf{res = Flatten[relations4th\ /.\ solution4th\ //\ N]}$$

$$\{a_{1.} \to 0.799266,\ a_{2.} \to -0.189413\}$$

$$\mathbf{Truncation\_error = Coefficient[TE,\ f^{(5)}[0]]}$$

$$-\frac{1}{60}\, h^4\, a_1 - \frac{8\, h^4\, a_2}{15} - \frac{81\, h^4\, a_3}{20}$$

Figure 3.4: Optimization of finite difference scheme.

Figure 3.5 shows the plots of modified wavenumbers versus exact wavenumber for schemes with different order of accuracy. For the fourth-order optimized scheme, the modified wavenumber $\bar{\alpha}\Delta x$ follows well with the straight line $\bar{\alpha}\Delta x = \alpha\Delta x$ in the range of $\bar{\alpha}\Delta x < 1.5$. At $\bar{\alpha}\Delta x$ greater than 1.5, the modified wavenumber starts to deviate increasingly from the exact line which produces dispersion error to the original PDEs. This limited wavenumber corresponds to a smallest wavelength that can be solved by a given mesh. By noticing that the wavelength λ is calculated as $\lambda = 2\pi/\alpha$ and use the relation that $\bar{\alpha}\Delta x < 1.5$, one immediately finds that the resolvable wavelength is limited at $\lambda > 4.2\Delta x$. To resolve waves with smaller wavelength, either the mesh size needs to be reduced or higher-order schemes have to be employed. Different schemes have different limitations of resolvable short wave components. Here we compare them qualitatively by introducing a new concept: the resolving efficiency. First, it is defined that $\varepsilon \geq \frac{|\bar{\alpha}\Delta x - \alpha\Delta x|}{\alpha\Delta x}$ where ε is the error tolerance such as $\varepsilon = 0.01$. This tolerance represents the error between the wavenumber of the scheme and the exact wavenumber. Each tolerance ε corresponds to a highest modified wavenumber that can be solved by the numerical scheme. For example, if we allow a slightly large error $\varepsilon = 0.1$, the maximum wavenumber can be solved by a fourth-order DRP scheme is $\bar{\alpha}\Delta x = 1.717$, see Table 3.1. For different schemes shown in Figure 3.5, their resolving efficiencies are quantified and tabulated in Table 3.1. It is evident that the optimized schemes stay close to the exact solution over a wider range of wavenumbers. Also, as the order of accuracy increases the scheme is able to resolve shorter waves (larger wavenumbers). As seen in Table 3.1, in case $\varepsilon = 0.001$ the schemes of fourteenth-order accuracy (curve i) resolves the maximum wavenumber about 1.68 which is about 22 times higher than the second-order scheme (curve a).

Schemes	$\varepsilon = 0.1$	$\varepsilon = 0.01$	$\varepsilon = 0.001$
(a) 2nd FD	0.707	0.243	0.075
(b) 4th FD	1.254	0.743	0.417
(c) 6th FD	1.536	1.089	0.731
(d) 4th DRP	1.717	1.509	1.431
(e) 6th DRP	1.834	1.605	1.481
(f) 8th DRP	1.921	1.695	1.525
(g) 10th DRP	1.990	1.776	1.576
(h) 12th DRP	2.045	1.848	1.629
(i) 14th DRP	2.091	1.913	1.682

Table 3.1: Maximum resolvable wavenumber ($\bar{\alpha}\Delta x$) of the schemes shown in Figure 3.5.

The dispersion error can be alternatively described in terms of phase speed error [13, 53]. The phase speed for a given wavenumber $\bar{\alpha}\Delta x$ is defined as $c_p = \bar{\alpha}\Delta x / \alpha\Delta x$. The phase speed of PDEs for all wavenumbers is one. Therefore $c_p - 1$ is a measure of the phase error. Figure 3.6 is a plot of phase speed from finite difference approximations versus the exact phase speed. Similar as before, the optimized schemes have the improved phase error in a wider range.

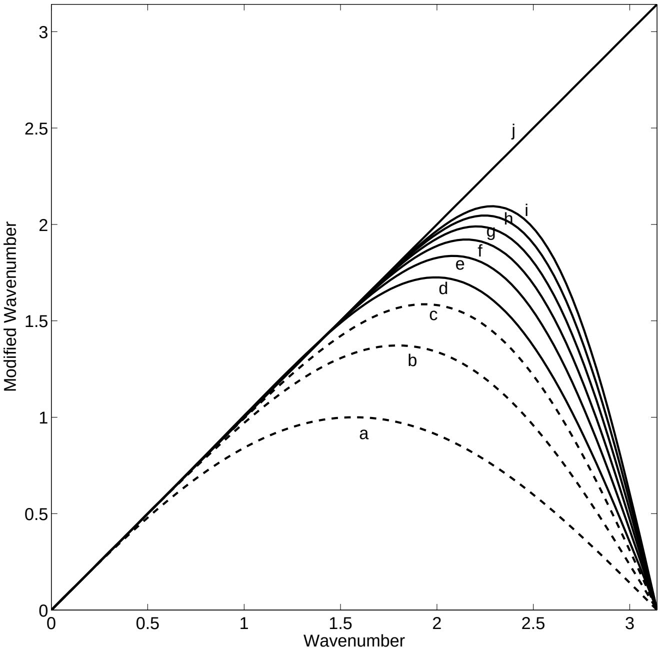

Figure 3.5: Wavenumber versus modified wavenumber for standard and optimized finite difference schemes. Dashed lines: original schemes; Solid lines: optimized schemes. (a) second-order finite difference; (b) fourth-order finite difference; (c) sixth-order finite difference; (d) fourth-order DRP; (e) sixth-order DRP; (f) eighth-order DRP; (g) tenth-order DRP; (h) twelfth-order DRP; (i) fourteenth-order DRP; (j) exact solution.

3.1.2 High-order compact schemes and the optimizations

The Padé type or compact finite difference schemes are different from the explicit schemes. One of the important difference between the two schemes is that the compact schemes approximate derivatives implicitly where the values of f_i' are solved together in the matrix form. Another difference, also is the advantage of compact scheme is that the compact schemes use less stencil points and have less dispersion errors compared to explicit schemes of same order of accuracy. Higher computational costs is the disadvantage of compact schemes since extra efforts are put on solving the matrix which contains all the derivatives. Lele [13] in 1992 showed the spectral-like resolution of the compact schemes for the evaluation of spatial derivatives. The

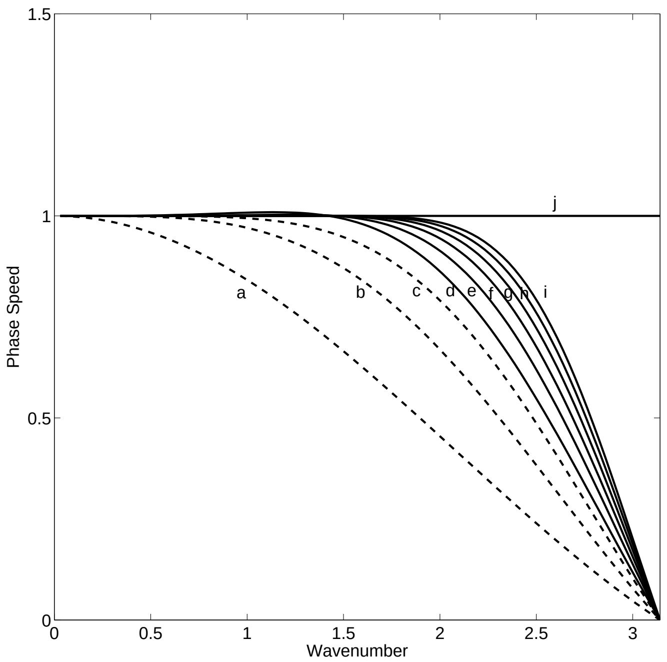

Figure 3.6: Phase speed versus modified wavenumber for standard and optimized finite difference schemes. Dashed lines: original schemes; Solid lines: optimized schemes. (a) second-order finite difference; (b) fourth-order finite difference; (c) sixth-order finite difference; (d) fourth-order DRP; (e) sixth-order DRP; (f) eighth-order DRP; (g) tenth-order DRP; (h) twelfth-order DRP; (i) fourteenth-order DRP; (j) exact solution.

emphasis was on improving a wide range of wavenumbers rather than simply increasing the order of accuracy. A family of compact schemes were derived by matching the Taylor series coefficients of various orders. The first unmatched coefficient is the formal truncation error of the scheme. This is very similar to what was shown in Figure 3.2 and Figure 3.3.

In the present study, following the work of Tam [12], Lele [13] and Kim [14], a series of high-order standard and optimized compact schemes are derived. The schemes are constructed as the following equation

$$\begin{aligned}\alpha f'_{j-1} + f'_j + \alpha f'_{j+1} &= a\frac{f_{i+1} - f_{i-1}}{\Delta x} + b\frac{f_{i+2} - f_{i-2}}{\Delta x} + c\frac{f_{i+3} - f_{i-3}}{\Delta x} \\ &\quad + d\frac{f_{i+4} - f_{i-4}}{\Delta x} + e\frac{f_{i+5} - f_{i-5}}{\Delta x}. \qquad (3.7)\end{aligned}$$

This classical compact scheme has a maximum accuracy of twelfth-order and a maximum 11-point stencil on the right hand side. To derive the coefficients for the compact scheme, an example is shown for a sixth-order scheme. As before, the first step is to carry out Taylor expansion for the finite difference approximation. This time, the derivatives on the left hand side of Equation (3.7) also needs to be expanded into Taylor series. This procedure is shown in Figure 3.7 where all f_i and f_i' in Equation (3.7) are approximated into an eighth-order Taylor series. The next step is to derive a standard sixth-order compact finite difference scheme. As shown in Figure 3.8 the derivatives on the left hand side of Equation (3.7) is moved to the right hand side. Therefore TE contains terms from zeroth to eighth-order. To achieve sixth-order accuracy of the scheme, all terms less than sixth-order in TE should vanish and the rest terms of TE represent higher-order truncation error. As calculated in Figure 3.8 the leading term of TE in this case is $-\frac{h^6}{1260}$ yields sixth-order accuracy of the scheme.

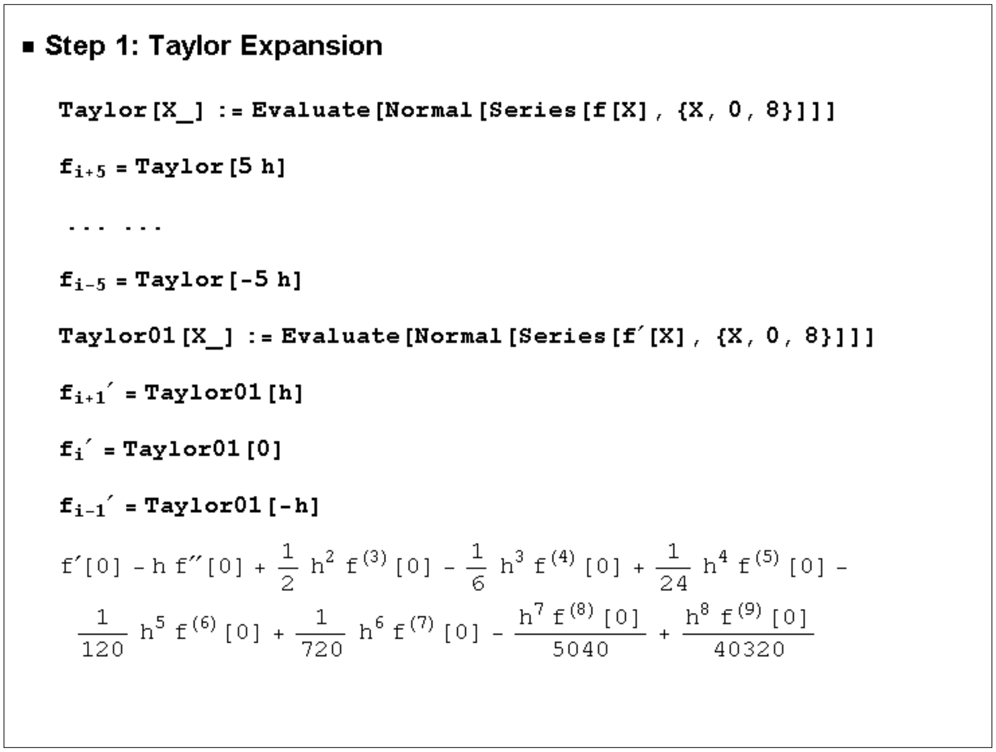

■ **Step 1: Taylor Expansion**

```
Taylor[X_] := Evaluate[Normal[Series[f[X], {X, 0, 8}]]]

fi+5 = Taylor[5 h]

... ...

fi-5 = Taylor[-5 h]

Taylor01[X_] := Evaluate[Normal[Series[f′[X], {X, 0, 8}]]]

fi+1′ = Taylor01[h]

fi′ = Taylor01[0]

fi-1′ = Taylor01[-h]
```

$$f'[0] - h\,f''[0] + \frac{1}{2}\,h^2\,f^{(3)}[0] - \frac{1}{6}\,h^3\,f^{(4)}[0] + \frac{1}{24}\,h^4\,f^{(5)}[0] - \frac{1}{120}\,h^5\,f^{(6)}[0] + \frac{1}{720}\,h^6\,f^{(7)}[0] - \frac{h^7\,f^{(8)}[0]}{5040} + \frac{h^8\,f^{(9)}[0]}{40320}$$

Figure 3.7: Taylor expansion.

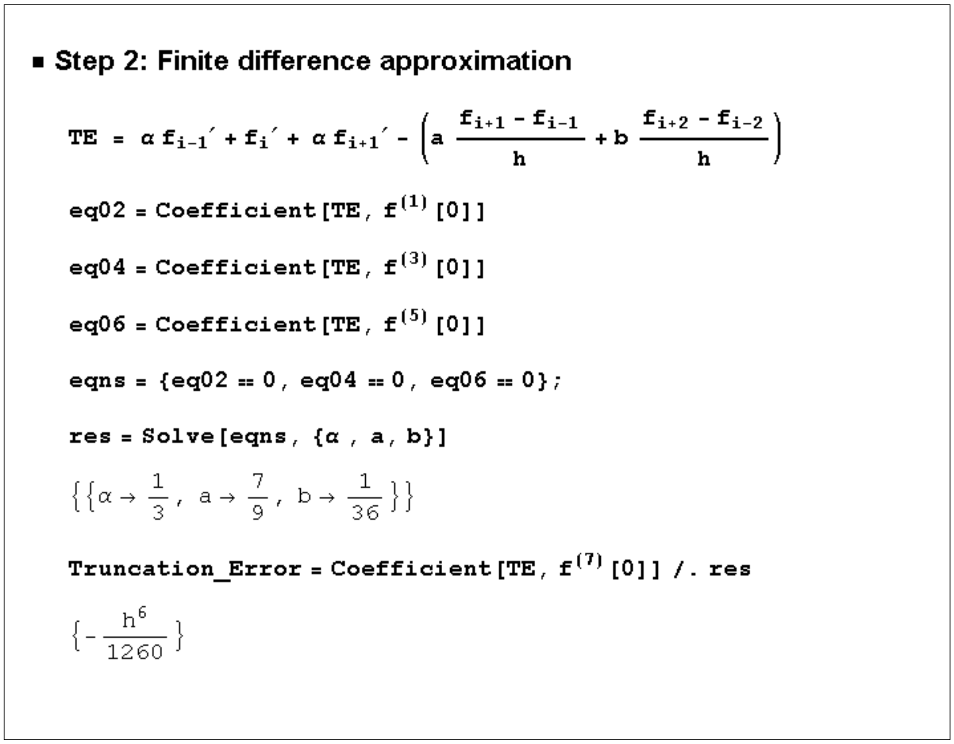

■ **Step 2: Finite difference approximation**

$$\mathbf{TE} = \alpha\, \mathbf{f}_{\mathbf{i-1}}{}' + \mathbf{f}_{\mathbf{i}}{}' + \alpha\, \mathbf{f}_{\mathbf{i+1}}{}' - \left(\mathbf{a}\,\frac{\mathbf{f}_{\mathbf{i+1}} - \mathbf{f}_{\mathbf{i-1}}}{\mathbf{h}} + \mathbf{b}\,\frac{\mathbf{f}_{\mathbf{i+2}} - \mathbf{f}_{\mathbf{i-2}}}{\mathbf{h}}\right)$$

```
eq02 = Coefficient[TE, f(1) [0]]

eq04 = Coefficient[TE, f(3) [0]]

eq06 = Coefficient[TE, f(5) [0]]

eqns = {eq02 == 0, eq04 == 0, eq06 == 0};

res = Solve[eqns, {α , a, b}]
```

$$\left\{\left\{\alpha \to \frac{1}{3},\ \mathrm{a} \to \frac{7}{9},\ \mathrm{b} \to \frac{1}{36}\right\}\right\}$$

```
Truncation_Error = Coefficient[TE, f(7) [0]] /. res
```

$$\left\{-\frac{\mathrm{h}^6}{1260}\right\}$$

Figure 3.8: Finite difference approximation.

The way to obtain an optimized compact scheme is to use the strategy of Tam and Webb [12]. Considering the finite difference approximation in the x-direction, the Fourier transform of the left and right hand side of Equation (3.7) yields

$$\begin{aligned}(i\alpha \mathrm{e}^{-i\bar{\omega}\Delta x} + 1 + i\alpha \mathrm{e}^{i\bar{\omega}\Delta x})i\bar{\omega}\Delta x = \\ a(\mathrm{e}^{i\omega\Delta x} - \mathrm{e}^{-i\omega\Delta x}) + b(\mathrm{e}^{2i\omega\Delta x} - \mathrm{e}^{-2i\omega\Delta x}) + \\ c(\mathrm{e}^{3i\omega\Delta x} - \mathrm{e}^{-3i\omega\Delta x}) + d(\mathrm{e}^{4i\omega\Delta x} - \mathrm{e}^{-4i\omega\Delta x}) + e(\mathrm{e}^{5i\omega\Delta x} - \mathrm{e}^{-5i\omega\Delta x})\end{aligned} \qquad (3.8)$$

where $i = \sqrt{-1}$ and $\alpha\Delta x$ is replaced by $\omega\Delta x$ simply because α is now used as a coefficient. Solving the wavenumber $\bar{\omega}\Delta x$ in Equation (3.8) and simplify the result with trigonometric expression gives

$$\bar{\omega}\Delta x = \frac{2(a\sin(\omega\Delta x) + b\sin(2\omega\Delta x) + c\sin(3\omega\Delta x) + d\sin(4\omega\Delta x) + e\sin(5\omega\Delta x))}{1 + 2\alpha\cos(\omega\Delta x)}. \qquad (3.9)$$

As already defined in Equation (3.4), the modified wavenumber $\omega\Delta x$ is used to minimize the integral error. The compact finite difference approximation produces an error between the exact and modified wavenumbers. Such an error can be written in an integrated form

$$E = \int_0^{r\pi} \mid \omega\Delta x - \bar{\omega}\Delta x \mid^2 W(\omega\Delta x) d(\omega\Delta x). \tag{3.10}$$

In Equation (3.10), r is a factor between 0 and 1 which decides the optimization range, $W(\omega\Delta x)$ is the weighting function. The weighting function is not required for optimization of explicit schemes as this was already done before. However, as the integral term becomes much more complicated it is feasible to introduce the weighting function to make the equation analytically integrable. Such kind of a weighting function was introduced by Kim and Lee [14]. The idea is to eliminate the divisor of the fraction (denominator) in Equation (3.9). Therefore, the weighing function in this case can be written as

$$W(\omega\Delta x) = (1 + 2\alpha\cos(\omega\Delta x))^2. \tag{3.11}$$

By now the standard compact scheme is ready to be optimized. Continue from the second step of Figure 3.8, instead of forcing the leading TE error to be sixth-order accurate we require it only to be fourth-order. This gives us an arbitrary free parameter among a, b and α. The optimization step is briefly shown in Figure 3.9, and it is seen that after matching the Taylor series coefficients of various orders, the coefficients α and a are found as function of b. Hence b is left for optimization using the relation that $\frac{\partial E}{\partial b} = 0$. Following these steps, coefficients for other high-order optimized compact schemes are shown in Table B.2 and B.3 in Appendix B.

Inserting the coefficients of Table B.2 and B.3 into Equation (3.9) results in Figure 3.10 which shows the plots of modified wavenumber versus exact wavenumber for various standard and optimized compact schemes. Recall that the fourth-order optimized explicit scheme (7-point DRP) is not able to solve wavenumber more than 1.5 (page 25). It can be seen in Figure 3.10 that the fourth-order optimized compact scheme (solid line d) has a better resolving ability. The resolvable wavenumber is approximately up to $\bar{\omega}\Delta x = 2$ which means that the scheme can resolve waves with minimum wavelength of $3.2\Delta x$. Thus the use of a high-order optimized scheme has advantageous in problems involving waves at higher frequencies. The resolving efficiency is compared for different compact schemes which is shown in Table 3.2. Once again the optimized schemes are seen to cover a wider range of wavenumbers.

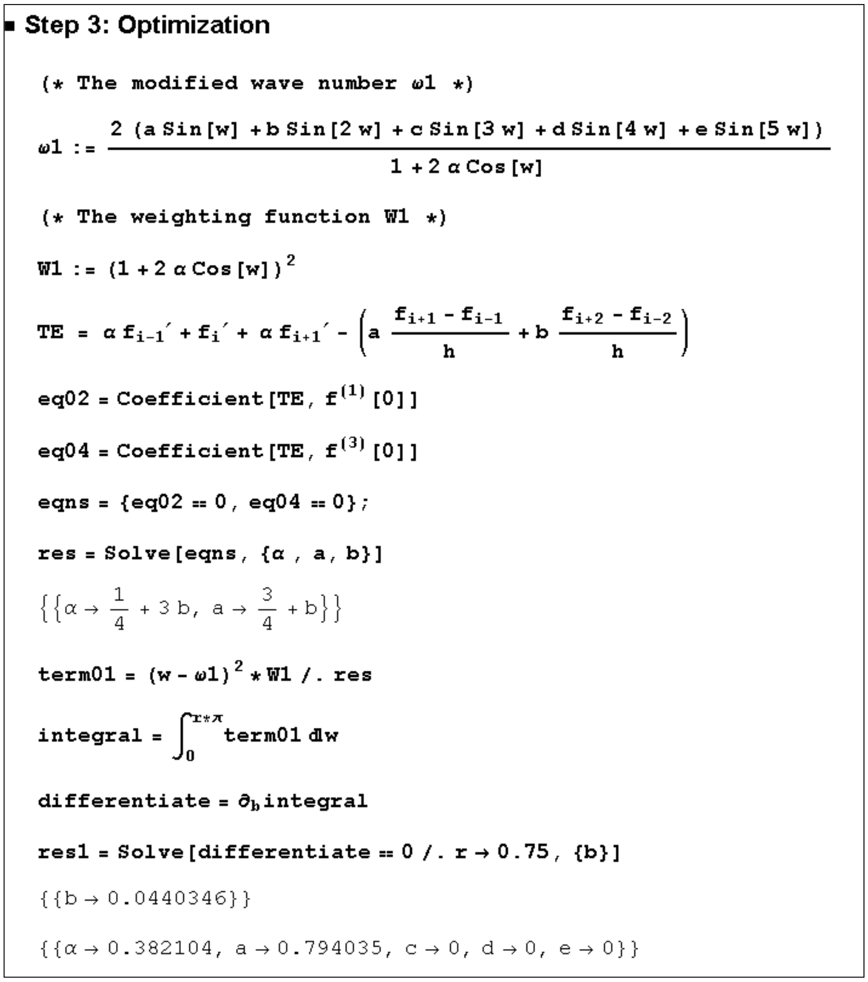

Step 3: Optimization

```
(* The modified wave number ω1 *)

ω1 := 2 (a Sin[w] + b Sin[2 w] + c Sin[3 w] + d Sin[4 w] + e Sin[5 w]) / (1 + 2 α Cos[w])

(* The weighting function W1 *)

W1 := (1 + 2 α Cos[w])^2

TE = α f_{i-1}′ + f_i′ + α f_{i+1}′ - (a (f_{i+1} - f_{i-1})/h + b (f_{i+2} - f_{i-2})/h)

eq02 = Coefficient[TE, f^(1)[0]]

eq04 = Coefficient[TE, f^(3)[0]]

eqns = {eq02 == 0, eq04 == 0};

res = Solve[eqns, {α , a, b}]

{{α → 1/4 + 3 b, a → 3/4 + b}}

term01 = (w - ω1)^2 * W1 /. res

integral = ∫_0^(r*π) term01 dw

differentiate = ∂_b integral

res1 = Solve[differentiate == 0 /. r → 0.75, {b}]

{{b → 0.0440346}}

{{α → 0.382104, a → 0.794035, c → 0, d → 0, e → 0}}
```

Figure 3.9: Optimization of compact scheme.

The same trend is seen in Figure 3.11 where the phase errors of different schemes are shown. It is apparent that as the scheme goes to higher-order it increases its ability of solving short waves. However, one might notice from Figure 3.10, 3.11 and Table 3.2 that the resolving efficiency does not increase linearly with the order of accuracy. For example, in Table 3.2 if we look at the column where $\varepsilon = 0.001$ the tenth-order optimized scheme is just slightly better than the sixth-order optimized scheme, say, $2.231/2.170 - 1 = 2.8\%$ is gained by increasing the order from six to ten. On the other hand the sixth-order optimized compact scheme is a lot better than the standard sixth-order compact scheme, $2.170/1.009 - 1 = 115\%$ is gained by extending only two points of the stencil width. There is no doubt that high-order schemes have better performance, however it is reasonable to find a balance between accuracy and computational cost. The number of stencil points decides both the accuracy of the scheme and the computing time, therefore the use of high-order schemes should be case dependent. In the present study, the sixth-order optimized scheme is normally used for two- and three-dimensional problems.

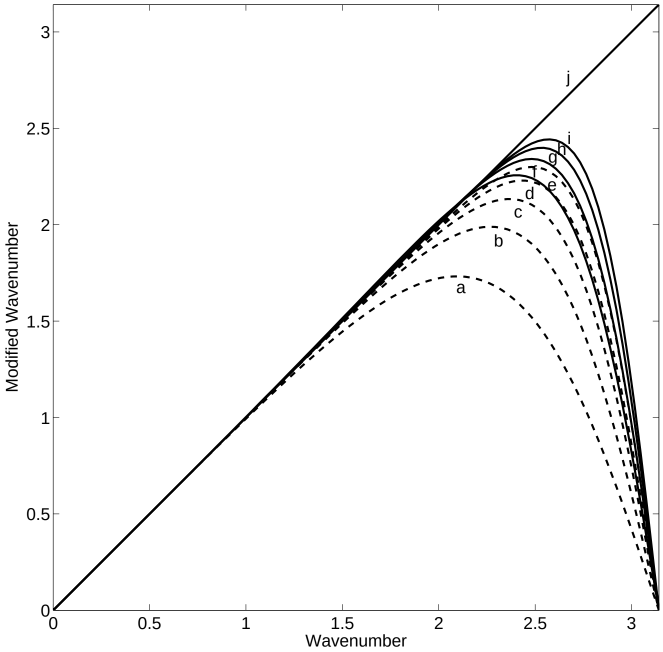

Figure 3.10: Wavenumber versus modified wavenumber for original and optimized compact finite difference schemes. Dashed lines: original schemes; Solid lines: optimized schemes. (a) fourth-order compact; (b) sixth-order compact; (c) eighth-order compact; (d) tenth-order compact; (e) twelfth-order compact; (f) fourth-order optimized compact; (g) sixth-order optimized compact; (h) eighth-order optimized compact; (i) tenth-order optimized compact; (j) exact solution.

3.1.3 Stencils for closures of high-order schemes

The previously introduced schemes are all symmetric and are implemented for the interior numerical domain. One difficulty of applying high-order

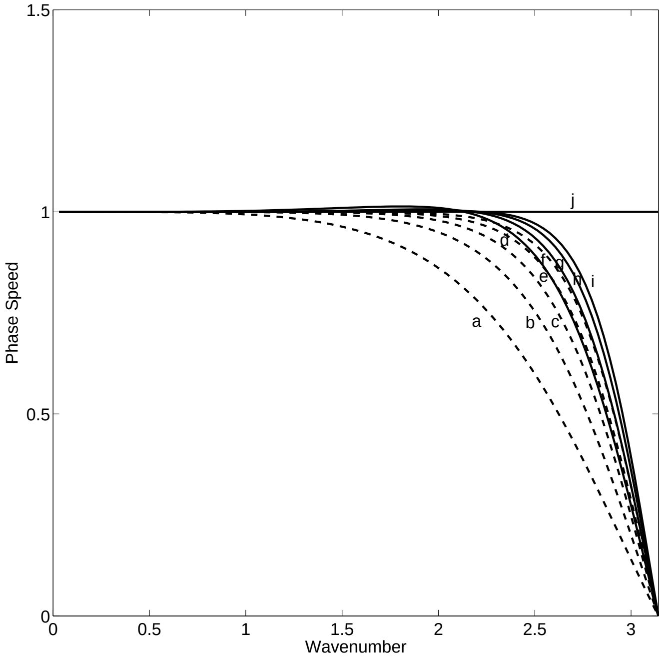

Figure 3.11: Phase speed versus modified wavenumber for original and optimized compact finite difference schemes. Dashed lines: original schemes; Solid lines: optimized schemes. (a) fourth-order compact; (b) sixth-order compact; (c) eighth-order compact; (d) tenth-order compact; (e) twelfth-order compact; (f) fourth-order optimized compact; (g) sixth-order optimized compact; (h) eighth-order optimized compact; (i) tenth-order optimized compact; (j) exact solution.

schemes is to find stable boundary closures which still preserve their formal accuracy. Here it has to be noticed that the boundary closures are differed from the physical boundary conditions which will be discussed in later sections. One typical way to build the boundary schemes is to use non-centered schemes at the edges of the computational domain. Tam et al. [12, 52, 54] applied 7-point backward stencils at the boundaries which have same order of accuracy as the interior schemes (see the backward coefficients in Table B.4, Appendix B). The backward DRP schemes are derived in the same way as those centered schemes. Zhuang et al. [55, 56] derived fourth-order upwind DRP schemes which can alternatively be treated as boundary closures. Other applications of such non-centered optimized boundary schemes are illustrated by Bogey et al. [58], Berland et al. [57] and Marsden et al. [34] where they simulated noise from turbulent jets and airfoils etc. Another

Schemes	$\varepsilon = 0.1$	$\varepsilon = 0.01$	$\varepsilon = 0.001$
(a) 4th-classical	1.674	1.089	0.628
(b) 6th-classical	1.983	1.556	1.099
(c) 8th-classical	2.133	1.805	1.381
(d) 10th-classical	2.229	1.961	1.601
(e) 12th-classical	2.297	2.085	1.726
(f) 4th-optimized	2.242	2.181	2.136
(g) 6th-optimized	2.330	2.246	2.170
(h) 8th-optimized	2.380	2.306	2.228
(i) 10th-optimized	2.425	2.364	2.231

Table 3.2: Maximum resolvable wavenumber ($\bar{\alpha}\Delta x$) of the schemes shown in Figure 3.10.

common practice is to use schemes with less stencil points near the boundaries in order to provide stable centered schemes. In the work of Bogey and Bailly [50], the size of the stencil at the boundary is decreased progressively, e.g, from 11 points in the inner domain to 3 or 5 points at the boundary. Djambazov et al. [60] simulated aerodynamic sound on a staggered mesh where centered schemes are still used on the boundary. To use the same high-order schemes at a boundary, e.g., on a solid wall, the mirroring procedure is applied: symmetry of pressure and parallel velocity components and antisymmetry of perpendicular velocity values.

The use of compact schemes may have the advantage of reducing the number of mesh points near the boundary where different formulations are required. The boundary closures for compact schemes were studied by Carpenter et al. [59] in terms of stability characteristics. The stability analysis of compact schemes and their corresponding boundary closures were carried out using the theory of Gustafsson, Kreiss and Sundstrom [61, 62] which is referred to as GKS stability theory. It is difficult to analyze the stability property for a fully discrete partial differential equations system, especially when non-centered boundary schemes are involved. Based on the GKS theory, Carpenter et al. [59] developed a series of stabilized compact boundary schemes. An example of such a boundary formulation for a sixth-order compact scheme is given in Appendix B. Some other compact near boundary formulations can be found in [13] where Lele proposed a set of compact schemes with spectral-like resolution both for inner and boundary region. Very recently, a new set of optimised boundary closure schemes was presented by Kim [63]. These boundary closures are given in a non-centered compact finite differences form. The near boundary schemes were optimised in the frequency domain and the newly developed schemes achieved the better resolution characteristics than traditional compact schemes. The optimized boundary schemes were derived from extrapolation beyond boundaries from which extra control variables were obtained for use of optimization.

3.1.4 Other high-order schemes

From above, the optimized explicit and compact finite difference schemes were studied and a series of coefficients for those two types of schemes were derived and their coefficients were appended. However, many other high-order finite difference schemes exist and it is therefore worthwhile to mention some of those schemes.

In addition to centered finite difference schemes, upwinding schemes are also very popular. For aeroacoustic simulations, first-order upwind schemes are too dissipative and dispersive, and therefore traditional upwinding schemes have been extended to higher orders using larger stencils. Ekaterinaris [45] used fifth-order upwind schemes to simulate sound field due to a pair of spinning vortices and showed that the solutions exhibited low dissipation and dispersion errors. The upwind finite difference schemes were optimized by Zhuang and Chen [55] based on the strategy of Tam and Webb [12]. The optimized upwind schemes were developed to improve the quality for solving short waves without adding a explicitly artificial damping terms to the finite difference equations. Following the idea of the DRP schemes, the upwind finite difference scheme can be written as

$$\frac{\partial f}{\partial x}(x_0) = \frac{1}{\Delta x}\sum_{j=-N}^{M} a_j f(x_0 + j\Delta x) \tag{3.12}$$

where M is the value to the right and N is the value to the left $(M \neq N)$. The optimization procedure followed the same as for the standard DRP schemes, except that the integrated error E now is defined as

$$\begin{aligned} E = \int_{-\pi/2}^{\pi/2} \mid \bar{\alpha}_r\Delta x - \alpha\Delta x \mid d(\alpha\Delta x) - \lambda \int_{-\pi/2}^{\pi/2} \mid \bar{\alpha}_i\Delta x + \\ \texttt{sgn}(c)\texttt{exp}\left[-\ln 2\left(\frac{\alpha\Delta x - \pi}{\sigma}\right)^2\right] \mid^2 d(\alpha\Delta x) \end{aligned} \tag{3.13}$$

where λ and σ are adjustable positive constants, $\bar{\alpha}_r$ and $\bar{\alpha}_i$ are real and imaginary parts of the wavenumber, and $\texttt{sgn}(c)$ defines the wave propagation direction. The integral error has real and imaginary parts which should both approach zero. By setting $\frac{\partial E}{\partial a_j} = 0$, the optimized upwind schemes are derived for pairs of M and N. A similar work was done by Li [64] using a different approach for optimization. Some other types of upwind high-order schemes can be seen in [65] and [66].

The pre-factored compact finite difference scheme developed by Hixon [67, 68, 69] is a member of compact schemes family. The new type of compact schemes maintain high-order accuracy while using a very small stencil size. Also the smaller boundary stencils make it easier to implement boundary conditions. The general compact finite difference scheme can be written as

$$[B]\{D_i\} = \frac{1}{\Delta x}[C]\{f_i\} \tag{3.14}$$

where D_i is the spatial derivative of f_i, $[B]$ and $[C]$ are coefficient matrices. The forward (D_i^F) and backward (D_i^B) derivative operators are introduced to the classical compact scheme of Equation (3.14) which satisfies

$$D_i = \frac{1}{2}(D_i^F + D_i^B). \tag{3.15}$$

Inserting Equation (3.15) into (3.14), two sets of schemes with forward and backward derivative operators are obtained as

$$\alpha_F D_{i+1}^F + \beta_F D_i^F = \frac{1}{\Delta x}(a_F f_{i+2} + b_F f_{i+1} + c_F f_i + d_F f_{i-1} + e_F f_{i-2}) \tag{3.16}$$

$$\beta_B D_i^B + \gamma_B D_{i-1}^B = \frac{1}{\Delta x}(a_B f_{i+2} + b_B f_{i+1} + c_B f_i + d_B f_{i-1} + e_B f_{i-2}). \tag{3.17}$$

When the two schemes are added the original central compact scheme (Equation (3.14)) must be recovered. The forward and backward coefficients are derived in such a way that the real parts of the numerical wavenumber in Equations (3.16) and (3.17) are identical to the wavenumber of classical compact scheme as Equation (3.14) and the imaginary parts of Equations (3.16) and (3.17) are equal and opposite to Equation (3.14). Followed the work of Hixon, Ashcroft and Zhang [70] optimized the pre-factored schemes using the strategy similar as shown in Equations (3.8-3.11). The modified wavenumber is obtained both for forward and backward schemes. For the forward compact scheme of Equation (3.16), the modified wavenumber satisfies

$$\mathtt{Re}(\bar{\omega}\Delta x) = \frac{(a_F\alpha_F + b_F\beta_F - c_F\alpha_F - d_F\beta_F)\sin(\omega\Delta x)}{\alpha_F^2 + \beta_F^2 + 2\alpha_F\beta_F\cos(\omega\Delta x)} + \frac{(a_F\beta_F - d_F\alpha_F - e_F\beta_F)\sin(2\omega\Delta x) - e_F\alpha_F\sin(3\omega\Delta x)}{\alpha_F^2 + \beta_F^2 + 2\alpha_F\beta_F\cos(\omega\Delta x)}. \tag{3.18}$$

$$\mathtt{Im}(\bar{\omega}\Delta x) = \frac{-(b_F\alpha_F + c_F\beta_F) - (a_F\alpha_F + b_F\beta_F + c_F\alpha_F + d_F\beta_F)\cos(\omega\Delta x)}{\alpha_F^2 + \beta_F^2 + 2\alpha_F\beta_F\cos(\omega\Delta x)} - \frac{(a_F\beta_F + d_F\alpha_F + e_F\beta_F)\cos(2\omega\Delta x) + e_F\alpha_F\cos(3\omega\Delta x)}{\alpha_F^2 + \beta_F^2 + 2\alpha_F\beta_F\cos(\omega\Delta x)} \tag{3.19}$$

Similar relations can be obtained for the backward scheme, as given by Equation (3.17). The integration error is defined in the same way for Equation (3.10) where the weighting function is properly selected to eliminate the divisor of the fraction in Equation (3.18) and (3.19). The optimization is finished by setting $\partial E/\partial\phi = 0$ where ϕ is one of the free coefficient to be optimized.

The third type of high-order schemes to be introduced here is the combined compact finite difference scheme which was developed by Chu and Fan [71, 72]. The novelty of the combined compact difference scheme is due to its combination of the first and second derivatives. The new scheme becomes more compact and more accurate, compared to traditional compact finite difference schemes. Using the same notation as before, let f_i', f_i'' denote the first and second derivatives of f_i in x-direction. The general combined compact scheme are written as

$$f_i' + \alpha_1(f_{i+1}' + f_{i-1}') + \beta_1\Delta x(f_{i+1}'' - f_{i-1}'') = \frac{a_1}{2\Delta x}(f_{i+1} - f_{i-1}) \tag{3.20}$$

$$f_i'' + \alpha_2(f_{i+1}'' + f_{i-1}'') + \frac{1}{2\Delta x}\beta_2(f_{i+1}' - f_{i-1}') = \frac{a_2}{\Delta x^2}(f_{i+1} - 2f_i + f_{i-1}). \tag{3.21}$$

As can be seen in Equation (3.20) and (3.21), the first and second derivatives are coupled which yield a combined compact scheme. This scheme turns out to have a wider range for solving higher wavenumbers. Since the second derivatives are also found together with the first derivatives, the combined compact scheme is interesting for problem involved viscous calculations. The scheme was originally developed for numerically solving flow problems which was not yet applied for aeroacoustic simulations. It is attractive to optimize the scheme to obtain lower dispersion error such as those optimized compact schemes. To derive and optimize such schemes towards higher-orders could be an interesting future work.

3.1.5 The effect of grid non-uniformity

In many cases, grid stretching can not be avoided for simulating flow or acoustic problems, typically for problems involved with turbulence. The standard and optimized high-order schemes are derived on a uniformly spaced computational grid. These schemes are widely used for numerical simulations for non-uniform grids. Therefore it is necessary to investigate the discretization errors introduced by grid stretching.

There exist many different stretching functions for mesh generation, here we select one of them to perform our analysis. Assume that the mesh spacing is Δx at point x_i and the grid is stretched with a ratio γ. Therefore at other neighboring points we have $x_{i+1} = x_i + \gamma \Delta x_i$.

Taking an example of 7-point DRP scheme, to derive the coefficients in this case we first perform Taylor expansion on a non-uniform mesh as shown in Figure 3.12. Then the slightly complicated expression is inserted to the finite difference approximation. Once the stretching rate γ is specified, the coefficients can be solved by minimizing the integral error.

The solution is plotted in Figure 3.13 with different stretching rate. The schemes derived on a non-uniform mesh are compared with standard 7-point schemes on a uniform mesh. It is observed that at a reasonable stretching rate, the schemes on a non-uniform mesh still perform better than a standard finite difference scheme. This case shows that for the stretching rate γ below 10%, the optimized schemes keep better accuracy than the standard ones. A similar study was carried out by Bogey and Bailly [50] where the same trend was found. A study of grid stretching effect was also performed for the optimized compact finite difference schemes. The results are shown in Figure 3.14. It turns out that the optimized compact schemes behave similar as DRP schemes. A more detailed study shows that the compact schemes are more sensitive to grid stretching. Figure 3.15 is the plot of truncation errors and dispersion errors for DRP and compact schemes. Both fourth and sixth-order schemes are shown in order to see the effect of increasing the order of accuracy. It can be seen from Figure 3.15(a) that the truncation error for all schemes is eventually increased to a higher level as the stretching rate increased to 1.2. From this plot, no evident difference can be found between DRP and compact schemes. For Figure 3.15(b) it is clearly seen that as γ increases, the integral of dispersion errors of the compact schemes increases faster than the explicit schemes. This means compact schemes are

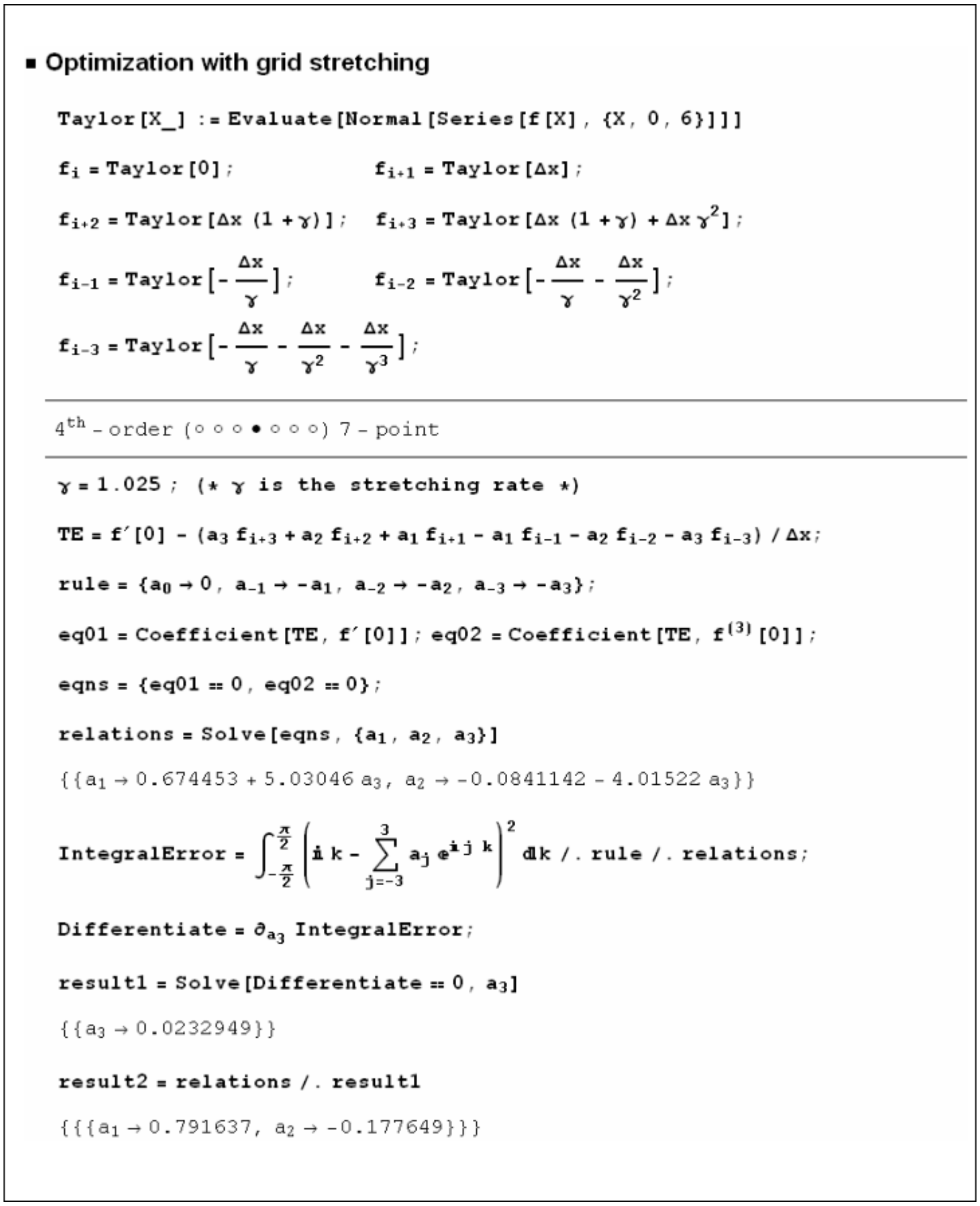

■ Optimization with grid stretching

```
Taylor[X_] := Evaluate[Normal[Series[f[X], {X, 0, 6}]]]

f_i = Taylor[0];                  f_{i+1} = Taylor[Δx];

f_{i+2} = Taylor[Δx (1 + γ)];     f_{i+3} = Taylor[Δx (1 + γ) + Δx γ^2];

f_{i-1} = Taylor[-Δx/γ];          f_{i-2} = Taylor[-Δx/γ - Δx/γ^2];

f_{i-3} = Taylor[-Δx/γ - Δx/γ^2 - Δx/γ^3];
```

4th - order (○ ○ ○ ● ○ ○ ○) 7 - point

```
γ = 1.025 ; (* γ is the stretching rate *)

TE = f'[0] - (a_3 f_{i+3} + a_2 f_{i+2} + a_1 f_{i+1} - a_1 f_{i-1} - a_2 f_{i-2} - a_3 f_{i-3}) / Δx;

rule = {a_0 → 0, a_{-1} → -a_1, a_{-2} → -a_2, a_{-3} → -a_3};

eq01 = Coefficient[TE, f'[0]]; eq02 = Coefficient[TE, f^(3)[0]];

eqns = {eq01 == 0, eq02 == 0};

relations = Solve[eqns, {a_1, a_2, a_3}]

{{a_1 → 0.674453 + 5.03046 a_3, a_2 → -0.0841142 - 4.01522 a_3}}

IntegralError = ∫_{-π/2}^{π/2} (ⅈ k - Σ_{j=-3}^{3} a_j ⅇ^(ⅈ j k))^2 ⅆk /. rule /. relations;

Differentiate = ∂_{a_3} IntegralError;

result1 = Solve[Differentiate == 0, a_3]

{{a_3 → 0.0232949}}

result2 = relations /. result1

{{{a_1 → 0.791637, a_2 → -0.177649}}}
```

Figure 3.12: Optimization of explicit finite difference scheme on non-uniform mesh.

more deteriorated than DRP schemes on the same non-uniform mesh. To sum up, the use of high-order schemes still maintain advantages for regularly stretched grids with not too high stretching rate. With the maximum stretching rate about 10%, the present optimized schemes are shown to be more accurate than the standard schemes with the same stencil size.

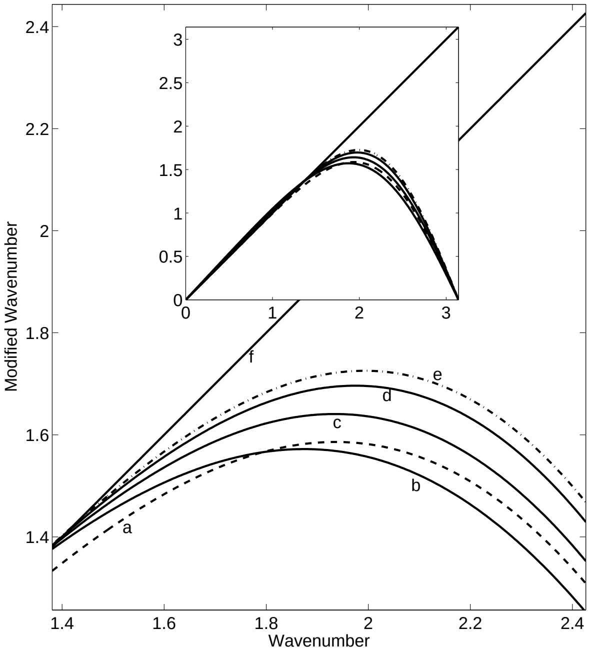

Figure 3.13: Wavenumber versus modified wavenumber. (a) Standard sixth-order finite difference scheme $\gamma = 1.0$; (b) 7-point DRP scheme $\gamma = 1.15$; (c) 7-point DRP scheme $\gamma = 1.075$; (d) 7-point DRP scheme $\gamma = 1.025$; (e) 7-point DRP scheme $\gamma = 1.0$; (f) Exact solution.

3.2 Time integration

Time marching schemes determine the accuracy of propagation characteristic of the governing PDEs. For computational aeroacoustics, an accurate time advancing scheme ensures better numerical solutions over a long time integration. In some cases, the space and time discretization are proceeded directly in the target equations. There are many examples of such methods, for example, Warming-Kutler-Lomax method, two-steps Lax-Wendroff method , MacCormack method and so on. Among the classical methods, the most common schemes are those of low order accuracy, particularly in space discretization. As shown before that we have already spend much effort to derive high-order schemes in space. The next is to find an accurate time marching scheme and then complete the semi-discrete formulation.

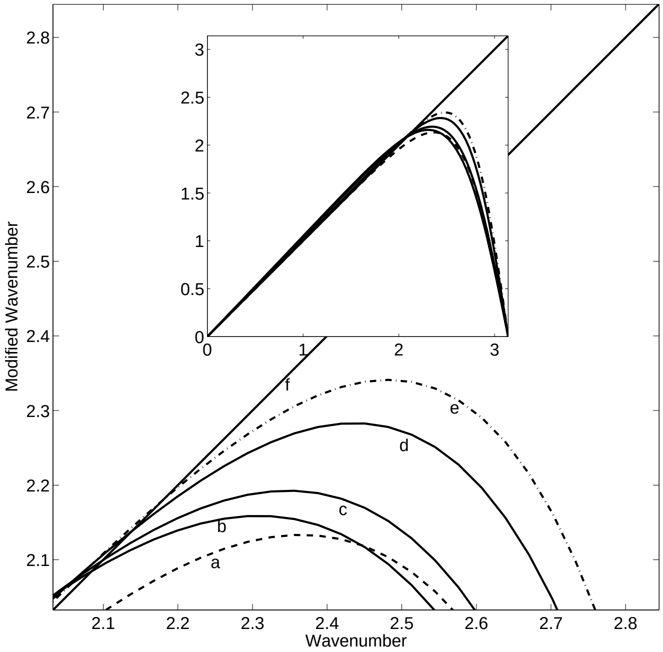

Figure 3.14: Wavenumber versus modified wavenumber. (a) Standard eighth-order compact scheme $\gamma = 1.0$; (b) sixth-order optimized compact scheme $\gamma = 1.15$; (c) sixth-order optimized compact scheme $\gamma = 1.075$; (d) sixth-order optimized compact scheme $\gamma = 1.025$; (e) sixth-order optimized compact scheme $\gamma = 1.0$; (f) Exact solution.

The first time discretization technique to be considered here is the one-step DRP time marching scheme. In the work of Tam and Webb [12], an explicit time integration method was also derived which followed the same idea of deriving space derivatives. Assuming that the solution of a variable f is known up to a time level $t = n\Delta t$, at time step $n+1$ the solution is advanced by a four-level finite difference approximation which takes the form

$$f_{(n+1)} \simeq f_{(n)} + \Delta t \sum_{j=0}^{3} b_j \left[\frac{df}{dt}\right]_{(n-j)} . \tag{3.22}$$

The formulation is fully explicit which is based on the knowledge at previous three time levels. At $t = 0$, $f_{(0)} = f_{initial}$ and $f_{(-1)}, f_{(-2)}, f_{(-3)}$ are set to zero. The coefficients b_j $(j = 0, 1, 2, 3)$ are determined by Taylor expansion and ensure that Equation (3.22) is accurate to order $(\Delta t)^3$. After matching

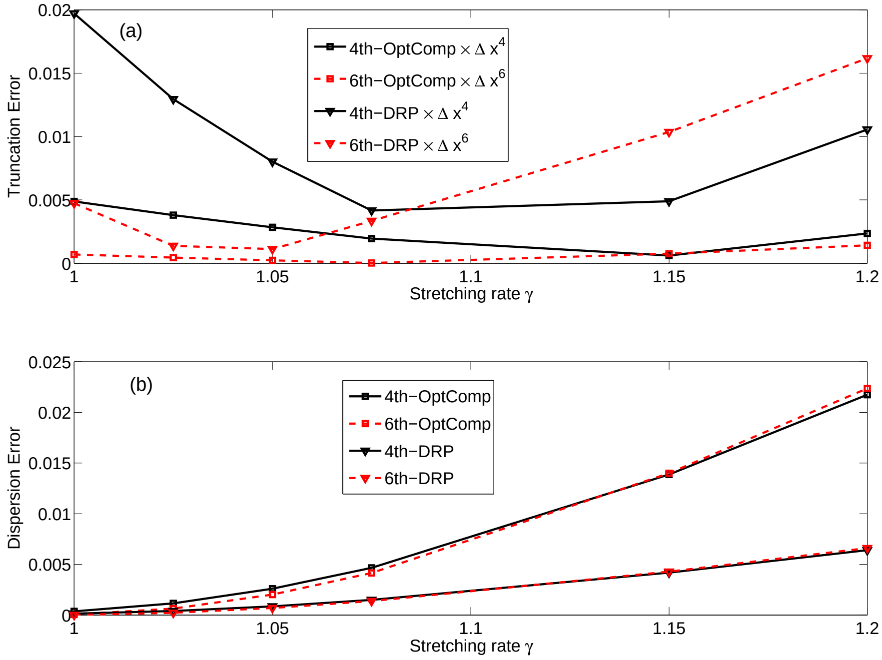

Figure 3.15: Truncation errors and integrated dispersion errors on a non-uniform grid with different stretching rates.

the coefficients of the Taylor expansion and solving the system of equations, one free parameter is left for optimization. For example, if b_0 is the free parameter the relations of the coefficients are

$$b_1 = -3b_0 + \frac{53}{12}, \qquad b_2 = 3b_0 - \frac{16}{3}, \qquad b_3 = -b_0 + \frac{23}{12}. \tag{3.23}$$

Applying Laplace transform $f(t) = \int_0^\infty \tilde{f}(\omega)\exp(i\omega t)d\omega$ to Equation (3.22), the following relation can be obtained

$$\frac{d\tilde{f}}{dt} \simeq -i\frac{i(\mathrm{e}^{-i\omega\Delta t} - 1)}{\Delta t\sum_{j=0}^{3} b_j \mathrm{e}^{ij\omega\Delta t}}\tilde{f} \tag{3.24}$$

where the tilde represents the Laplace transform. Using the knowledge that the Laplace transform of the time derivative is identical to $-i\omega\tilde{f}$, the above equation is rearranged as

$$\bar{\omega} = i\frac{i(\mathrm{e}^{-i\omega\Delta t} - 1)}{\Delta t\sum_{j=0}^{3} b_j \mathrm{e}^{ij\omega\Delta t}} \tag{3.25}$$

where $\bar{\omega}$ is the effective angular frequency of the finite difference approximation shown in Equation (3.22).

The last procedure is to determine the minimum integral error. Unlike those symmetric schemes, both real and imaginary part of the error appear in the integrated equation.

$$E = \int_{-\eta}^{\eta} \{\sigma[\mathtt{Re}(\bar{\omega}\Delta t - \omega\Delta t)]^2 + (1-\sigma)[\mathtt{Im}(\bar{\omega}\Delta t - \omega\Delta t)]^2\} d(\omega\Delta t) \quad (3.26)$$

By setting the integral rage $\eta = 0.5$ and the weighting parameter $\sigma = 0.36$, the root of equation $\partial E/\partial b_0 = 0$ is found to be $b_0 = 2.30255809$. The full set of coefficients are thus known from Equation (3.23).

Another time integration method received a lot of the attention in computational aeroacoustic is the Runge-Kutta (RK) method. The method was originally proposed by Runge in 1895 and further developed by Kutta in 1901. Due to the high-order accuracy, even after hundred years, the RK method is still popularly used in many applications. The classical RK method has the order of accuracy equal or less to the number of stages. Consider the time derivative $\frac{\partial f}{\partial t} = R(f)$, a p-stage RK method advance the solution from t_n to $t_n + \Delta t$ can be written as

$$f_{(0)} = f_{(n)} \quad (3.27)$$

$$f_{(l)} = f_{(n)} + \alpha_l \Delta t R(f_{(l-1)}) \quad (l = 1, ..., p) \quad (3.28)$$

$$f_{(n+1)} = f_{(p)}. \quad (3.29)$$

The standard p-stage RK method can be obtained with Taylor series expansion of $f(t_n + \Delta t)$. To illustrate the method, we derive in the following the two-stage RK scheme.

Using the notation $f_{(n+1)}$ to represent the value f at time $t_n + \Delta t$ and $h = \Delta t$, the Taylor series expansion of $f_{(n+1)}$ gives

$$f_{(n+1)} = f_{(n)} + hf'_{(n)} + \frac{1}{2}h^2 f''_{(n)} + ... + \frac{1}{q!}h^q f^{(q)}_{(n)} + \mathcal{O}(h^{q+1}). \quad (3.30)$$

Since $f' = \frac{\partial f}{\partial t} = R(f)$, Equation (3.30) is identical to

$$f_{(n+1)} = f_{(n)} + hR_{(n)} + \frac{1}{2}h^2 R'_{(n)} + ... + \frac{1}{q!}h^q R^{(q-1)}_{(n)} + \mathcal{O}(h^{q+1}). \quad (3.31)$$

To derive a second-order scheme we truncate Equation (3.31) up to third-order such that

$$f_{(n+1)} = f_{(n)} + hR_{(n)} + \frac{1}{2}h^2 R'_{(n)} + \mathcal{O}(h^3). \tag{3.32}$$

By noticing that R is a function of t and f, the time derivative of R is

$$R'_{(n)} = \left(\frac{\partial R}{\partial t}\right)_{(n)} + \left(\frac{\partial R}{\partial f}\right)_{(n)} \left(\frac{\partial f}{\partial t}\right)_{(n)} = \left(\frac{\partial R}{\partial t}\right)_{(n)} + \left(\frac{\partial R}{\partial f}\right)_{(n)} R_{(n)}. \tag{3.33}$$

Inserting Equation (3.33) into Equation (3.32) gives the Taylor series expansion of $f_{(n+1)}$ which will be compared to the result obtained from the RK method.

$$f_{(n+1)} = f_{(n)} + hR_{(n)} + \frac{1}{2}h^2 \left(\left(\frac{\partial R}{\partial t}\right)_{(n)} + \left(\frac{\partial R}{\partial f}\right)_{(n)} R_{(n)} \right) + \mathcal{O}(h^3). \tag{3.34}$$

A two-step RK method is formulated as

$$f_{(n+1)} = f_{(n)} + h(\omega_1 k_1 + \omega_2 k_2) \tag{3.35}$$

where ω_1, ω_2 are unkown coefficients and k_1, k_2 are given as

$$k_1 = R(t_{(n)}, f_{(n)}) \tag{3.36}$$

$$k_2 = R(t_{(n)} + \alpha h, f_{(n)} + \beta h k_1) \tag{3.37}$$

To determine the four unknowns ω_1, ω_2, α and β, we first expand k_2 as following

$$\begin{aligned} k_2 &= R(t_{(n)} + \alpha h, f_{(n)} + \beta h k_1) \\ &= R(t_{(n)}, f_{(n)} + \beta h k_1) + \alpha h \frac{\partial}{\partial t} R(t_{(n)}, f_{(n)} + \beta h k_1) + \mathcal{O}(h^2) \\ &= R_{(n)} + \alpha h \left(\frac{\partial R}{\partial t}\right)_{(n)} + \beta h \left(\frac{\partial R}{\partial f}\right)_{(n)} R_{(n)} + \mathcal{O}(h^2). \end{aligned} \tag{3.38}$$

Inserting Equation (3.36) and (3.38) into Equation (3.35) the final two-stage RK approximation is obtained

$$f_{(n+1)} = f_{(n)} + (\omega_1 + \omega_2) h R_{(n)} + \omega_2 h^2 \left(\alpha \left(\frac{\partial R}{\partial t} \right)_{(n)} + \beta \left(\frac{\partial R}{\partial f} \right)_{(n)} R_{(n)} \right) + \mathcal{O}(h^3). \tag{3.39}$$

By comparing Equation (3.39) with the exact Taylor expansion of Equation (3.34), it is not hard to find the following relations

$$\begin{cases} \omega_1 + \omega_2 = 1 \\ \alpha \omega_2 = \frac{1}{2} \\ \beta \omega_2 = \frac{1}{2} \end{cases} . \tag{3.40}$$

It is seen that the equation system is over-determined since there are four unknowns and only three equations. Theoretically, one of those four coefficients can be given with an arbitrary real value. The worst case occurs when ω_2 becomes zero since the two-step scheme returns to traditional first-order Euler forward method.

Since RK time marching methods cause additional dispersion and dissipation errors, it is attractive to do optimizations. As shown before for the two-stage RK scheme, it is possible to utilize the free coefficient(s). The optimization usually decreases the formal order of accuracy as compared to the classical RK schemes using the same number of stages, but it will be more accurate in terms of wave propagation over a wide range of frequencies. The optimization of time marching scheme is very similar to optimization of spatial schemes. A typical example has been previously shown in this section for deriving DRP time advancing scheme. Hu et al. [73] optimized a series of RK schemes with 4, 5 and 6 stages by minimizing the numerical error in the RK schemes. Some similar work can be seen from Bogey et al. [50] and Berland et al. [74]. For RK schemes with a maximum stage of $p \leq 4$, it holds true that the order of accuracy is equal to the number of stages. However, to achieve fifth-order accuracy one has to add two more stages and seven stages are required for a sixth-order RK scheme. This explains why the fourth-order RK time advancing method is the most popular one.

To ensure that the time integration is stable, the time step needs to be carefully selected. For the classical RK schemes, the maximal time step is determined by the eigenvalues of $R(f)$. If the centered finite difference spatial discretization method is used and we disregard the effect from boundary schemes, the maximum time step is related to the well-known Courant-Friedrichs-Levy (CFL) condition

$$CFL = \frac{c_0 \Delta t}{h} < \frac{c_1}{K_{max}} \tag{3.41}$$

where c_0 is the wave propagation speed, c_1 is a constant specified by the RK scheme and K_{max} is the maximum effective wavenumber of a given finite difference scheme. The constant for c_1 is 1.73 and 2.83 for three- and four-stage RK schemes [73, 48]. The maximum resolvable wavenumbers K_{max} of finite difference schemes are already obtained, see Table 3.1 for DRP schemes and Table 3.2 for optimized compact schemes. Therefore, the CFL numbers can be readily calculated. Consider three- and four-stage RK time advancing schemes and combine K_{max} of DRP and compact schemes, the CFL numbers can be shown in a matrix form, as seen in Table 3.3 and 3.4. From the CFL numbers listed in the tables, it is seen that for finite difference schemes, a smaller time step is required as the order of accuracy increases. And it is in general such that time steps for compact schemes (Table 3.4) are more restricted than for explicit schemes (Table 3.3).

Explicit	RK3			RK4		
Schemes	$\varepsilon = 0.1$	$\varepsilon = 0.01$	$\varepsilon = 0.001$	$\varepsilon = 0.1$	$\varepsilon = 0.01$	$\varepsilon = 0.001$
(a)	2.45	7.12	23.07	4.00	11.65	37.73
(b)	1.38	2.33	4.15	2.26	3.81	6.79
(c)	1.13	1.59	2.37	1.84	2.60	3.87
(d)	1.01	1.15	1.21	1.65	1.88	1.98
(e)	0.94	1.08	1.17	1.54	1.76	1.91
(f)	0.90	1.02	1.13	1.47	1.67	1.86
(g)	0.87	0.97	1.10	1.42	1.59	1.80
(h)	0.85	0.94	1.06	1.38	1.53	1.74
(i)	0.83	0.90	1.03	1.35	1.48	1.68

Table 3.3: CFL numbers. (a) second-order finite difference; (b) fourth-order finite difference; (c) sixth-order finite difference; (d) fourth-order DRP; (e) sixth-order DRP; (f) eighth-order DRP; (g) tenth-order DRP; (h) twelfth-order DRP; (i) fourteenth-order DRP.

We close this section by briefly noting the CFL restrictions of Tam and Webb's [12] time marching scheme. It is attractive to know the time step limits for the DRP time marching method since it evaluates variables only once per time level and therefore it might be more effective. The CFL cri-

Compact	RK3			RK4		
Schemes	$\varepsilon = 0.1$	$\varepsilon = 0.01$	$\varepsilon = 0.001$	$\varepsilon = 0.1$	$\varepsilon = 0.01$	$\varepsilon = 0.001$
(a)	1.03	1.59	2.75	1.09	1.68	2.91
(b)	0.87	1.11	1.57	0.92	1.18	1.67
(c)	0.81	0.96	1.25	0.86	1.01	1.33
(d)	0.78	0.88	1.08	0.82	0.93	1.14
(e)	0.75	0.83	1.00	0.80	0.88	1.06
(f)	0.77	0.79	0.81	0.82	0.84	0.86
(g)	0.74	0.77	0.80	0.79	0.81	0.84
(h)	0.73	0.75	0.78	0.77	0.79	0.82
(i)	0.71	0.73	0.77	0.75	0.77	0.82

Table 3.4: CFL numbers. (a) fourth-order compact; (b) sixth-order compact; (c) eighth-order compact; (d) tenth-order compact; (e) twelfth-order compact; (f) fourth-order optimized compact; (g) sixth-order optimized compact; (h) eighth-order optimized compact; (i) tenth-order optimized compact.

terion of the one-stage four-level time advancing scheme plus seven-point DRP space discretization method was studied by Tam and Webb [12]. As proposed in [12], the time step criterion was originally written as

$$\Delta t = \frac{\Omega}{1.75[M + (1 + (\Delta x/\Delta y)^2)^{1/2}]} \frac{\Delta x}{c_0}. \tag{3.42}$$

In case that the denominator $1.75[M + (1 + (\Delta x/\Delta y)^2)^{1/2}] = 1.75$, Δt has its maximum value. The maximum value of Ω proposed in [12] is 0.4, therefore the DRP scheme has a up limit of CFL $= 0.4/1.75 = 0.23$. If one uses a four-stage RK scheme plus seven-point DRP space discretization method, the maximum CFL number can be seen from Table 3.3. For instance, if we fix the tolerance $\varepsilon = \frac{|\bar{\alpha}\Delta x - \alpha\Delta x|}{\alpha\Delta x} = 0.1$ and find the seven-point DRP scheme (at row (d)), the criterion is CFL$= 1.65$. From this point of view, the one-stage DRP time marching method is still more costly than a four-stage RK method.

3.3 Numerical filters and artificial damping

In numerical simulations of fluid dynamics and aeroacoustics, numerical oscillations are often experienced which comes as spurious solutions. These spurious oscillations are directly responsible for numerical convergence and usually lead to failure of the simulation. Centered finite difference schemes are dissipation free which yield spurious solutions with high frequencies. The use of high-order schemes or larger stencils will not reduce such numerical errors. The remedy is based on smoothing of the spurious waves by using filtering schemes or artificial damping (artificial dissipation) techniques. High-order filtering method ought to be used for aeroacoustic simulations to prevent extra damping of physical waves after thousands of time iterations. We shall see the effect of using high-order filtering schemes during the following discussions.

3.3.1 Explicit filters

In principle, the amount of damping depends on the wavenumbers such that only short waves are damped out. In aeroacoustic simulations time dependent signals are often recorded during the numerical simulation which is used to analyze the sound spectrum at given receiver locations. The use of filtering schemes should not smooth out the time dependence of variables after long time simulation. High-order filter schemes are used for such purpose.

For a centered filter scheme containsing 2N+1 points, the equations is written as

$$u_f(x_0) = u(x_0) - \sigma D(x_0) \tag{3.43}$$

with

$$D(x_0) = \sum_{j=-N}^{N} d_j u(x_0 + j\Delta x) \tag{3.44}$$

where u_f is the filtered value and u is the value at previous time level. The coefficients d_j are such that $d_j = d_{-j}$ and σ is the damping coefficient between 0 and 1. For determining coefficients of high-order explicit filter schemes, the standard approach [75] is to use Taylor series of Equations (3.43) and matching the corresponding coefficients. Based on the standard centered explicit high-order filters and the optimization strategy of Tam and Webb [12], a series of optimized selective filters were developed by Bogey and Bailly [50]. The coefficients of optimized explicit filter schemes are given in Table B.6 of Appendix B. For the boundaries, non-centered high-order optimized schemes with seven- and eleven-point stencils were proposed by Berland et al. [76]. The non-centered filters were tested with a two-dimensional benchmark problem of waves scattering by a cylinder. They showed that for reflection problems the non-centered filters provided better results than the centered filters.

An example is shown to highlight the influence of difference filter schemes. Consider a Gaussian type function as in Equation (3.45). We define two type of waves in this function, a short wave ($b_1 = 2$) and a long wave ($b_2 = 10$). Let the initial locations $x_1 = 50$ and $x_2 = 150$, we apply explicit second-, fourth- and twelfth-order filters to the two waves.

$$u = \exp(-(\ln 2)(x - x_1)^2/b_1^2) + \exp(-(\ln 2)(x - x_2)^2/b_2^2). \tag{3.45}$$

As plotted in Figure 3.16, the filtered solutions are obtained after one thousand iterations. The effect of the twelfth-order filter scheme is almost negligible to the original function. The fourth-order filter scheme has a weak effect on the longer wave (the right one) but the short wave (the left one) is apparently damped for almost thirty percent of the amplitude. The behavior of the second-order filter scheme is unfortunately not satisfactory for both short and long waves.

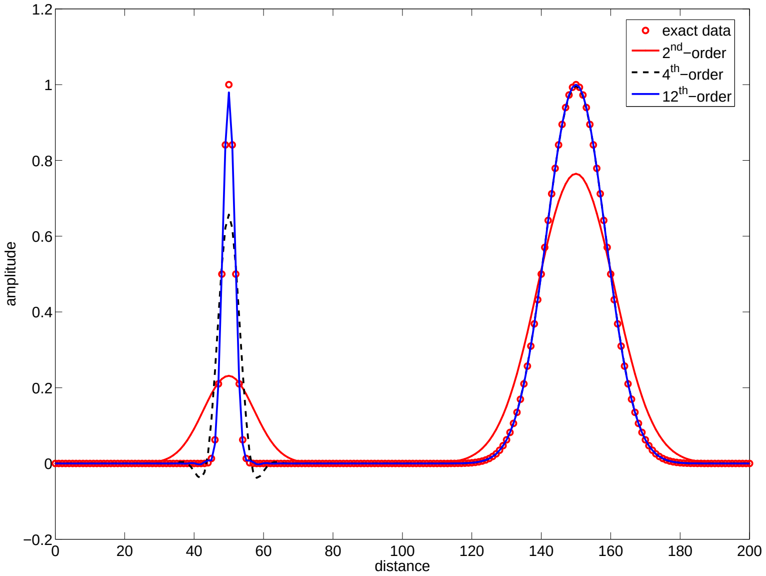

Figure 3.16: Effect of filtering schemes.

3.3.2 Implicit filters

The standard formulation of compact finite difference filters can be seen in Lele [13] where pentadiagonal filter schemes were formulated. The compact filters considered in the work of Visbal and Gaitonde [51] are based on Padé-type formulations which are tridiagonal systems of equations. The centered interior filtering scheme in compact form is written as

$$\alpha_f \tilde{f}_{j-1} + \tilde{f}_j + \alpha_f \tilde{f}_{j+1} = \sum_{n=0}^{N} \frac{a_n}{2}(f_{j+n} + f_{j-n}) \tag{3.46}$$

where $\tilde{f}$ is the value after filtering, α_f is the free parameter and a_n are the coefficients determining the order of accuracy. These compact filters are derived up to tenth-order of accuracy and their coefficients are listed in Table B.7, Appendix B. A few test cases were carried out by Visbal and Gaitonde [51, 78] using Padé-type spatial differencing formulas and filters. The computations were performed on stretched grid and high-frequency oscillations were successfully eliminated by high-order filters. At near boundary points, high-order non-centered compact filters were developed by Gaitonde and Visbal [77] which retain the tridiagonal form of the filters. The formulation of the boundary filters are given by

$$\alpha_f \tilde{f}_{j-1} + \tilde{f}_j + \alpha_f \tilde{f}_{j+1} = \sum_{n=0}^{N} a_n f_n. \tag{3.47}$$

Numerous steady and unsteady, viscous and invicid flow computations were performed on curvilinear meshes using domain-decomposition strategies which demonstrated the accuracy of new type of boundary filter schemes.

3.3.3 The artificial damping zone

Another technique called damping zone (sponge zone) can be used in combination with the high-order filtering schemes. In aeroacoustic simulations, this method is often favorable to be applied together with the far field boundary conditions to decrease the amount of reflection. As it can be seen sometimes in numerical simulations, the amplitude of turbulent structures are still large at outflow boundaries (See Figure 3.1 for example). The reason could be that the computational domain is not large enough or that the grid density at the outflow boundary were not coarse enough to numerically dissipate the small structures. In case the outflow area is not of our interest and numerical problems arise from there, a sponge zone can be defined and waves travel into this area will be heavily damped. Damping zones of this kind can be seen from Bogey and Bailly [79] and it is formulated as follows

$$f_i = f_i - \alpha \left(\frac{x(i) - x_1}{x_2 - x_1} \right)^{\beta} [3d_0 f_i + d_1(f_{i+1} + f_{i-1})] \tag{3.48}$$

where α defines the amplitude of the filtering, β takes values between 1 and 2 and $d_0 = 0.5$, $d_1 = -0.25$. The sponge zone has a length of $x_1 \leq x \leq x_2$. The second type of damping function we introduce here is seen from Israeli et al. [80] and Adams [81]

$$f_i = f_i - \sigma(i) f_i \tag{3.49}$$

$$\sigma(i) = A_s(N_s+1)(N_s+2)\frac{(x(i)-x_1)^{N_s}(x_2-x(i))}{(x_2-x_1)^{N_s+2}} \tag{3.50}$$

where the sponge region is again $x_1 \leq x \leq x_2$ and A_s, N_s are adjustable parameters such as $A_s = 4$ and $N_s = 3$.

To show the impact of the sponge zone, we let a sinusoidal wave travel into the sponge zone. The sponge zone is depicted in Figure 3.17 with a length about 1/3 of the domain. The above mentioned two types of damping methods applied in this case are named as damping1 and damping2. Both of the damping functions effectively absorbed waves in the defined damping region while a smooth connection between filtered and non-filtered parts are still maintained.

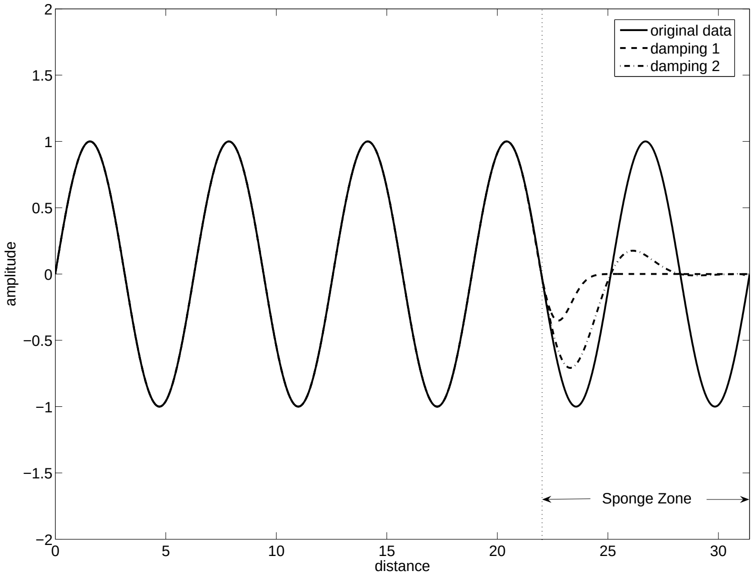

Figure 3.17: Damping effects at out boundary.

3.4 Acoustic boundary conditions

Boundary conditions play an important role in CAA. Any waves reflected by the computational boundaries will travel back and forth in the domain and interact with other physical waves until they dissipate after long time period. The desire to develop stable and accurate boundary conditions makes it an interesting research area. In the following, solid wall and far field conditions will be studied. The acoustic radiation and outflow boundary conditions are focused in this section since in the present work we consider exterior flow and CAA problems.

3.4.1 Wall conditions

In this part, a few methods that treat solid wall boundary conditions are introduced and tested in our numerical simulations to be stable. There exist many other methods and the common difficulty is the proper use of ghost points extended outside of the computational domain.

The DRP schemes proposed by Tam and Webb [12] provide a wide opportunity to build high-order boundary schemes as those we introduced before. In connection with the backward DRP schemes, Tam and Dong [82] proposed a set of numerical wall boundary conditions using a minimum number of ghost values. Any of the numerical values outside the physical domain are ghost values. These ghost values are often calculated by extrapolation, mirroring of inner points or from other physical conditions. The idea of Tam and Dong [82] is to use one ghost point inside the wall surface and use the backward schemes to simulate the normal derivatives on the wall. The near boundary stencils are sketched in Figure 3.18. Assume that the inviscid fluid is bounded by the wall at $x = 0$ (see Figure 3.18) and seven-point DRP schemes are used for calculating derivatives $\partial/\partial x$ and $\partial/\partial y$. If u, v are velocity components in x and y directions, the wall condition for the normal velocity component is $u = 0$ at $x = 0$. In the work of Tam and Dong the condition $u = 0$ is implicitly used to calculate the ghost value of pressure p inside the wall. All normal derivatives near the wall are calculated by non-centered DRP schemes (see Table B.4). The quantities $\partial u/\partial x$, $\partial v/\partial x$ and $\partial \rho/\partial x$ are computed using values lying inside the domain and $\partial p/\partial x$ is found by using the stencil extend to the ghost point below the wall.

In case of using compact finite difference schemes, the same inviscid wall condition is employed. Non-centered compact boundary stencils are applied at near wall region. The u-velocity is set to zero on the wall and the pres-

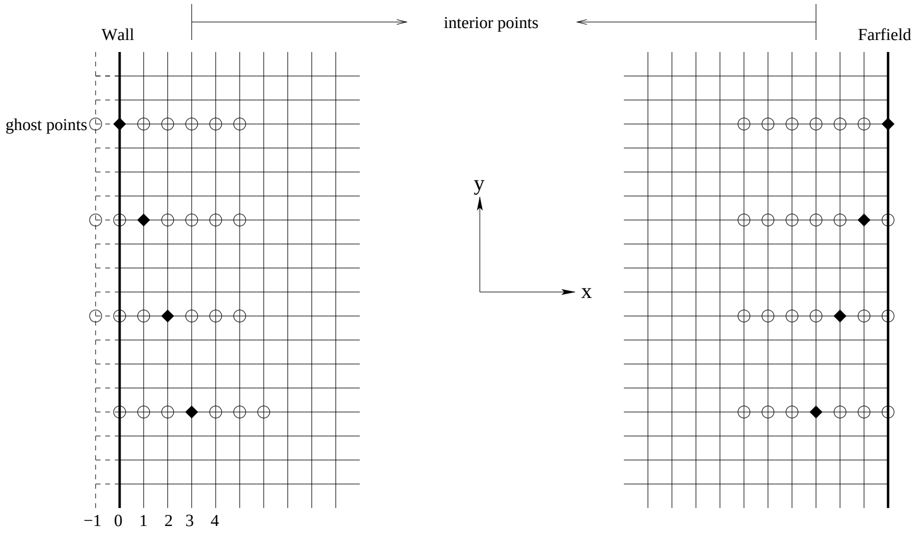

Figure 3.18: Stencils used in interior, wall and farfield regions.

sure, density and tangential velocity components are extrapolated. Their normal derivatives near the wall are approximated to high-order accuracy using non-centered high-order compact formulas. Application of such type of wall boundary treatment can be found in Visbal et al. [51] where a few acoustic scattering problems were studied. To achieve even lower dispersive error, the boundary derivatives can be alternatively calculated using optimized non-centered compact schemes as proposed by Kim [63].

Another wall boundary condition was discussed by Djambazov et al. [60]. A body-fitted staggered mesh was used in their numerical simulations. For invisid problems, solid walls are modeled as symmetric surfaces. Therefore, on the wall surface normal component of velocity is zero and the normal derivatives of pressure and other velocity component are set to zero. The centered finite difference scheme is used on the wall with a number of ghost points in the wall. The cell-centered ghost points are found in the way that the pressure and parallel velocity values are mirrored with the values in the fluid, and the normal velocities take the antisymmetric value in the fluid. This method is convenient for staggered mesh since the same differencing schemes can be used all over the domain. However, this method may not keep the same high-order accuracy on the wall boundary as in the inner domain since mirroring procedure is a non-physical model.

3.4.2 Acoustic farfield conditions

Since the domain for numerical computation is finite, appropriate boundary conditions must be supplied at farfield boundaries. The inflow/outflow conditions are developed to produce a non-reflective boundary or smoothly radiate out the waves. These boundary conditions are derived as a combination of physical models and mathematical approximations. In this section, three types of inflow/outflow boundary conditions are introduced. The first class of farfield conditions is called characteristic boundary conditions which was developed by Thompson [83, 84]. The second group uses the asymptotic solutions to the exterior problems and assumes that the boundaries are located far from the sources or disturbances. This kind radiation boundary condition was suggested by Bayliss et al. [85] and Tam et al. [12]. The third type of condition is the perfectly matched layer (PML) boundary condition. The method was proposed by Hu [86, 87] where spacial PML equations are solved in a buffer zone to minimize the reflections at outflow.

Characteristic boundary conditions:

The characteristic boundary condition is one of the popular methods in computational fluid dynamics. The method is based on the decomposition of hyperbolic equations into different wave modes. The resulting system contains incoming and outgoing waves. Here we first look at the Thompson's approach [83, 84] which is based on analyzing the Euler equations. One dimensional analysis is performed on the Euler equations to distinguish which are the directions of wave propagation on the farfield boundaries. The amplitude of the outgoing waves is determined from the values inside the domain by using non-centered schemes (see Figure 3.18). The amplitude of the incoming waves is set to zero for nonreflective case. Let's consider the non-linear Euler equations in cylindrical coordinates and to demonstrate the Thompson's approach.

$$\frac{\partial Q}{\partial t} + A\frac{\partial Q}{\partial r} + B\frac{\partial Q}{\partial x} + C = 0 \tag{3.51}$$

where $Q = [\rho, u, v, p]'$ is the primitive variables and matrices A, B and C are given as

$$A = \begin{pmatrix} v & 0 & \rho & 0 \\ 0 & v & 0 & 0 \\ 0 & 0 & v & 1/\rho \\ 0 & 0 & \gamma p & v \end{pmatrix}, B = \begin{pmatrix} u & \rho & 0 & 0 \\ 0 & u & 0 & 1/\rho \\ 0 & 0 & u & 0 \\ 0 & \gamma p & 0 & u \end{pmatrix}, C = \begin{pmatrix} \frac{\rho v}{r} \\ 0 \\ 0 \\ \frac{\gamma p v}{r} \end{pmatrix} \tag{3.52}$$

If we focus boundaries only along the x-axis, Equation (3.52) can be written in another form

$$\frac{\partial Q}{\partial t} + B\frac{\partial Q}{\partial x} + K = 0 \tag{3.53}$$

where the radial derivatives and the source term C are grouped together as a new term K. The matrix B can be diagonalized such that $SBS^{-1} = \Lambda$ with the diagonal element $\Lambda = diag(u-1, 1, u+1)$. Applying this to Equation (3.53) gives

$$S\frac{\partial Q}{\partial t} + \mathcal{L}_i + SK = 0 \tag{3.54}$$

where

$$\mathcal{L}_i = \begin{cases} \Lambda S\frac{\partial Q}{\partial x} & \text{for outgoing waves} \\ 0 & \text{for incoming waves} \end{cases} \tag{3.55}$$

To understand these characteristic waves $\mathcal{L}_i$, Equation (3.54) can be expanded as

$$\begin{aligned} \frac{\partial p}{\partial t} - \rho c_0\frac{\partial u}{\partial t} &= -\mathcal{L}_1 - K_4 + \rho c_0 K_2 = R_1 && (3.56)\\ c_0^2\frac{\partial \rho}{\partial t} - \frac{\partial p}{\partial t} &= -\mathcal{L}_2 - c_0^2 K_1 + K_4 = R_2 && (3.57)\\ \frac{\partial v}{\partial t} &= -\mathcal{L}_3 - K_2 = R_3 && (3.58)\\ \frac{\partial p}{\partial t} + \rho c_0\frac{\partial u}{\partial t} &= -\mathcal{L}_4 - K_4 - \rho c_0 K_2 = R_4. && (3.59) \end{aligned}$$

The time derivatives $(\frac{\partial \rho}{\partial t}, \frac{\partial u}{\partial t}, \frac{\partial v}{\partial t}, \frac{\partial p}{\partial t})$ are therefore obtained by

$$\begin{aligned} \frac{\partial \rho}{\partial t} &= \frac{1}{c_0^2}\left(\frac{1}{2}(R_1 + R_4) + R_2\right) && (3.60)\\ \frac{\partial u}{\partial t} &= \frac{1}{2}\rho c_0 (R_4 - R_1) && (3.61)\\ \frac{\partial v}{\partial t} &= R_3 && (3.62)\\ \frac{\partial p}{\partial t} &= \frac{1}{2}(R_1 + R_4) && (3.63) \end{aligned}$$

and the boundary points are updated using these time derivatives. The same procedure can be repeated for the radial direction. If the $\mathcal{L}_1$ wave is the incoming wave (velocity=u-c < 0) and $\mathcal{L}_2, \mathcal{L}_3, \mathcal{L}_4$ are outgoing waves, the amplitude of these characteristic waves given by Thompson [83, 84] are

$$\mathcal{L}_1 = 0 \tag{3.64}$$

$$\mathcal{L}_2 = u(c_0^2 \frac{\partial \rho}{\partial x} - \frac{\partial p}{\partial x}) \tag{3.65}$$

$$\mathcal{L}_3 = u \frac{\partial v}{\partial x} \tag{3.66}$$

$$\mathcal{L}_4 = (u + c_0)(\frac{\partial p}{\partial x} + c_0 \rho \frac{\partial u}{\partial x}). \tag{3.67}$$

The Thompson's approach is intrinsically one-dimensional and is suited for flow perpendicularly reaching the outer boundaries. Giles [88] improved the Thompson's approach by considering the more generalized case of oblique incidences. The first step of Giles approach is to perform the Fourier analysis in space and Laplace transform in time along boundary directions. The second step is to decompose the resulting system into incoming and outgoing waves. The last step is to inverse the transformed boundary equations back to real space and determine the amplitudes of the characteristic waves $\mathcal{L}_i$. A similar improvement was done by Kim and Lee [89] where soft inflow boundary conditions are implemented to maintain the mean flow velocity at the inlet boundary. The improved boundary conditions were tested by Kim and Lee where flow and sound field around cylinder was simulated by using high-order compact schemes.

Radiation and outflow boundary conditions:
The second class of boundary conditions are based on asymptotic analysis of the linearized Euler equations. This approach was originally proposed in a uniform mean flow condition [85, 90, 12]. In the work of Tam and Webb [12] the Fourier and Laplace transforms were performed on linearized Euler equations for the disturbances in two dimensions. The transformed equations are decomposed into solutions of the entropy wave (only consisting of density fluctuations, $u = v = 0$), the vorticity wave (only consisting of velocity fluctuations $p = \rho = 0$) and the acoustic wave (including all physical variables). At inflow boundaries only outgoing acoustic waves are presented, the boundary condition is written as

$$\left(\frac{1}{V(\theta)} \frac{\partial}{\partial t} + \frac{\partial}{\partial r} + \frac{1}{2r} \right) \begin{pmatrix} \rho \\ u \\ v \\ p \end{pmatrix} = 0 + \mathcal{O}(r^{-5/2}) \tag{3.68}$$

where $V(\theta) = c_0\left(M\cos(\theta-\varphi) + (1 - M^2\sin^2(\theta-\varphi))^{\frac{1}{2}}\right)$, $M = \frac{\sqrt{u_0^2+v_0^2}}{c_0}$, $c_0 = \sqrt{\gamma p_0/\rho_0}$ is the sound speed and φ is the mean flow angle. The accuracy of the boundary condition is proportional to the radial length of the computational domain. In cartesian coordinates the equations at inflow boundaries are

$$\frac{1}{V(\theta)}\frac{\partial\rho}{\partial t} + \cos(\theta)\frac{\partial\rho}{\partial x} + \sin(\theta)\frac{\partial\rho}{\partial y} + \frac{\rho}{2r} = 0 \tag{3.69}$$

$$\frac{1}{V(\theta)}\frac{\partial u}{\partial t} + \cos(\theta)\frac{\partial u}{\partial x} + \sin(\theta)\frac{\partial u}{\partial y} + \frac{u}{2r} = 0 \tag{3.70}$$

$$\frac{1}{V(\theta)}\frac{\partial v}{\partial t} + \cos(\theta)\frac{\partial v}{\partial x} + \sin(\theta)\frac{\partial v}{\partial y} + \frac{v}{2r} = 0 \tag{3.71}$$

$$\frac{1}{V(\theta)}\frac{\partial p}{\partial t} + \cos(\theta)\frac{\partial p}{\partial x} + \sin(\theta)\frac{\partial p}{\partial y} + \frac{p}{2r} = 0. \tag{3.72}$$

Equations (3.69-3.72) are modified at outflow boundary since the outgoing disturbances contain acoustic, entropy and vorticity waves. It appears that the total pressure fluctuation comes only from the acoustic disturbances, thus the outgoing boundary condition for pressure is the same as radiation boundary condition. The complete set of outflow boundary conditions are given as

$$\frac{\partial\rho}{\partial t} + u_0\frac{\partial\rho}{\partial x} + v_0\frac{\partial\rho}{\partial y} = \frac{1}{c_0^2}\left(\frac{\partial p}{\partial t} + u_0\frac{\partial p}{\partial x} + v_0\frac{\partial p}{\partial y}\right) \tag{3.73}$$

$$\frac{\partial u}{\partial t} + u_0\frac{\partial u}{\partial x} + v_0\frac{\partial u}{\partial y} = -\frac{1}{\rho_0}\frac{\partial p}{\partial x} \tag{3.74}$$

$$\frac{\partial v}{\partial t} + u_0\frac{\partial v}{\partial x} + v_0\frac{\partial v}{\partial y} = -\frac{1}{\rho_0}\frac{\partial p}{\partial y} \tag{3.75}$$

$$\frac{1}{V(\theta)}\frac{\partial p}{\partial t} + \cos(\theta)\frac{\partial p}{\partial x} + \sin(\theta)\frac{\partial p}{\partial y} + \frac{p}{2r} = 0. \tag{3.76}$$

The asymptotic boundary conditions of Tam and Webb [12] are used to develop the non-uniform [92] and non-homogeneous [93] radiation, inflow and outflow boundary conditions which produce more accurate incoming acoustic and vorticity waves. From our numerical experiences, in case that the disturbance at the outflow region is not strong the difference of inflow and outflow conditions is found to be very little. It was also shown that a larger computational domain with a relative coarser mesh at farfield boundaries produces better results.

Absorbing boundary conditions using PML:
The PML method proposed by Hu [86, 87] was originally formulated for electromagnetic problems [91]. The idea of PML approach is to divide the computational domain into two parts, the interior part and a PML (buffer layer) area around the computational edges. The acoustic, vorticity and entropy waves are supposed to be absorbed in this buffer layer. The amount of absorption depends on the thickness of the PML domain and the absorption coefficients. The theory behind the PML method is also based on analyzing the linearized Euler equation. Assume a two-dimensional uniform flow of Mach number M in the x-axis direction, buffer layers are defined at the four edges of a rectangular computational domain. For the buffer layers in x- and y-directions, the absorption coefficients are defined as σ_x and σ_y, respectively. At the four corners of computational domain, buffer layers in x- and y-directions are overlapped and the effect of σ_x and σ_y are all taken into account. In the linearized Euler equations, the primitive variables u, v, p and ρ are split into two parts (u_1, v_1, p_1, ρ_1) and (u_2, v_2, p_2, ρ_2). The equations for PML domains are defined as

$$\frac{\partial\binom{u_1}{v_1}}{\partial t} + \begin{pmatrix}\sigma_x\\ \sigma_y\end{pmatrix}\begin{pmatrix}u_1\\ v_1\end{pmatrix} = -\frac{\partial(p_1+p_2)}{\partial\binom{x}{y}} \tag{3.77}$$

$$\frac{\partial\binom{u_2}{v_2}}{\partial t} + \begin{pmatrix}\sigma_x\\ \sigma_x\end{pmatrix}\begin{pmatrix}u_2\\ v_2\end{pmatrix} = -M\frac{\partial\binom{u_1+u_2}{v_1+v_2}}{\partial x} \tag{3.78}$$

$$\frac{\partial\binom{p_1}{\rho_1}}{\partial t} + \begin{pmatrix}\sigma_x\\ \sigma_x\end{pmatrix}\begin{pmatrix}p_1\\ \rho_1\end{pmatrix} = -\frac{\partial(u_1+u_2)}{\partial x} - M\frac{\partial\binom{p_1+p_2}{\rho_1+\rho_2}}{\partial x} \tag{3.79}$$

$$\frac{\partial\binom{p_2}{\rho_2}}{\partial t} + \begin{pmatrix}\sigma_y\\ \sigma_y\end{pmatrix}\begin{pmatrix}p_2\\ \rho_2\end{pmatrix} = -\frac{\partial(v_1+v_2)}{\partial y}. \tag{3.80}$$

It is noted that these equations are reduced to the Euler equations when $\sigma_x = \sigma_y = 0$ and the spatial derivative in these equations involve only total variables u, v, p and ρ which ensure smooth connection at interfaces. Assuming that a plane wave propagates into the PML domain, then the wave can be written as an exponential function. For example, the u_1 component is written as $u_1 = u_0 \exp(i(xk_x + yk_y - \omega t))$ where u_0 is the amplitude. Inserting such plane waves into the PML Equations (3.77 - 3.80) yields plane wave solutions for (u_1, v_1, p_1, ρ_1) and (u_2, v_2, p_2, ρ_2).

As a closure of this section, we review some previous works where numerical experiments were done for different boundary conditions. Hixon et al. [94] investigated the characteristic boundary conditions of Thompson and Giles, and the radiation boundary conditions from Tam and Webb in uniform flow. According to their comparative performance some conclusions were drawn: The Tam and Webb's approach is the most acceptable performance for outflow boundary treatment; The performance of characteristic boundary conditions might be acceptable only when the flow is nearly one-dimensional and normal to the boundary. For inflow boundaries, Giles boundary condition and Tam and Webb's approach were acceptable. The Thompson's approach resulted some reflection near the inflow boundary. Colonius and Lele [41] performed a study on the boundary conditions of Thompson, Giles, Tam and Webb, and PML. Results showed that Tam and Webb's radiation boundary condition are the best at early times which has a maximum error about half of PML methods. Further, they reported that there is a slow long-time instability of Tam and Webb's radiation boundary condition. The characteristic boundary conditions are about an order of magnitude higher than Tam and Webb's radiation condition. The PML layers with more points produce less error.

3.5 Numerical features applied for current study

The in-house CFD code EllipSys has been used for flow simulations. The code was developed in co-operation between DTU[1] [95] and RISØ[2] [96]. The EllipSys code is based on a multi-block and cell-centered finite volume discretization of the steady and unsteady incompressible NS equations in primitive variables (pressure-velocity coupling). A predictor-corrector method is used. In the predictor step, the momentum equations are discretized using a second-order backward differentiation scheme in time and second-order central differences in space, except for the convective terms that are discretized by the QUICK upwind scheme. In the corrector step, the improved Rhie-Chow interpolation developed by Shen et al. [97] and the modified SIMPLEC scheme on the collocated grids [98] are used in order to avoid numerical oscillations from pressure decoupling. The obtained pressure Poisson equation can be solved by a five-level multigrid technique. Since the EllipSys3D code is programmed using a multi-block topology, it can be parallelized relatively easy using the Message Passing Interface (MPI).

The acoustic code is one of the auxiliary model of the EllipSys program. In EllipSys, each auxiliary model has its interface. The interface routines are called from the main program. The acoustic model is solved in the main iteration loop which solves the flow field. The flow solution obtained after each iteration will be used for acoustic simulation. At the same time level, the acoustic variables are solved by acoustic equations using high-order finite

---

[1] Fluid Mechanical Section, Department of Mechanical Engineering, Technical University of Denmark, Lyngby, Denmark.

[2] Department of Wind Energy, Risø National Laboratory, Roskilde, Denmark.

difference schemes. In the input data, explicit/implicit schemes from second-order up to tenth-order can be selected for solving the acoustic equations. The filter schemes are also specified in the same way in the input file. At walls, standard inviscid conditions are employed together with necessary backward high-order schemes. The Tam and Webb's radiation and outflow conditions are applied at outer boundary. The multi-block topology was also used for acoustic computation but a special routine was built such that each blocks can receive necessary information from their neighboring blocks. Considering a stencil width of 2N+1 points, such a scheme at its block interfaces (not including the physical boundaries) has N points extending outside which is in its neighboring blocks. The MPI routine was so created that there is a N-point overlapping at each block interfaces such that Nth-order accuracy is maintained everywhere.

Part II

Applications

Chapter 4

Validation Cases

A few numerical test cases are shown in this chapter. The first case is the one-dimensional wave convection problem which is used to validate the optimized explicit and implicit finite difference schemes. The second case concerns sound scattering problem from a circular cylinder and it's used to test DRP schemes and the wall, farfield boundary conditions on curvilinear mesh. In the last case, sound field generated by a pair of co-rotating vortex is simulated with optimized compact schemes.

4.1 Wave convection problem

In this example a one-dimensional convective wave equation is solved by explicit and compact finite difference schemes. The one-dimensional wave equation is given as

$$\frac{\partial u}{\partial t} + \frac{\partial u}{\partial x} = 0. \tag{4.1}$$

In this case, we consider the initial disturbance at t = 0 as a Gaussian type equation such as

$$u = \exp\left(-\ln(2)(x - x_0)^2/b^2\right). \tag{4.2}$$

The value b in Equation (4.2) defines the wavelength. The wavelength increases as b increases. In the present case, $b = 3$ and $b = 1.5$ are selected as long and short waves respectively. The wave is initially located at $x_0 = 50$. All simulations are performed using an equally spaced mesh with $\Delta x = 1.0$ and a CFL number of 0.1. The standard fourth-order Runge-Kutta scheme is used for time integration. The space discretization is performed by four different schemes: 7-point central difference scheme (sixth-order), 7-point DRP scheme (fourth-order), 5-point standard compact scheme (sixth-order) and 5-point optimized compact scheme (fourth-order). These schemes are selected such that they are comparable in terms of stencil points and order of accuracy.

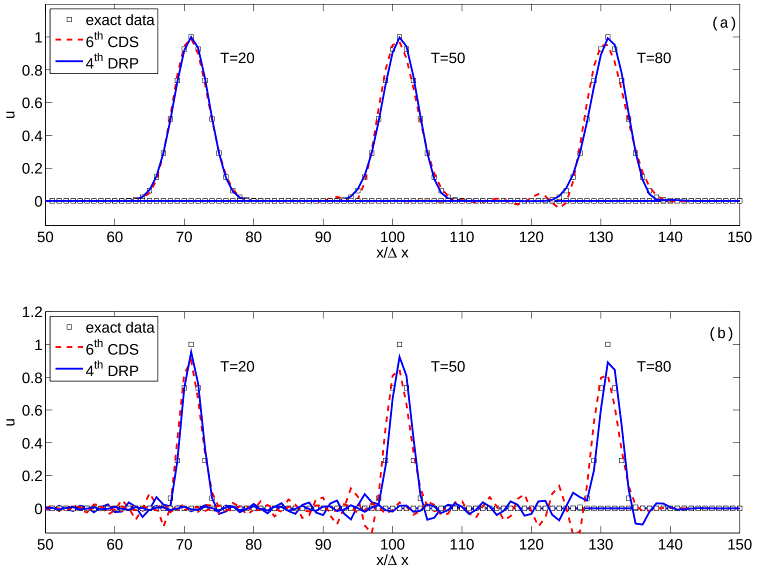

Figure 4.1: Propagation of waves at three time instant, T = 20, 50 and 80. Simulated by sixth-order standard center difference scheme and fourth-order DRP scheme. (a) b=3; (b) b=1.5.

In Figure 4.1 (a) and (b), results from 7-point explicit schemes are compared for long and short wave cases. For the long wave case of $b = 3$, result from the fourth-order DRP scheme fits well with exact data after some distance of propagation, as seen from Figure 4.1 (a). In general, result from the standard scheme performs well until T = 80 where it becomes less accurate as compared to DRP scheme. Larger difference are seen in the short wave case for $b = 1.5$ where both of the two explicit schemes are not acceptable. As seen in Figure 4.1 (b), the considerably strong oscillations are produced by the two explicit schemes but DRP scheme still performs better. Examples of using standard and optimized compact scheme are also shown in Figure 4.2 (a) and (b). For the long waves case, the results are well-fitted with exact data by using the two types of compact schemes. In Figure 4.2 (b) for the short wave case, it can be noticed from the plot that the optimized compact scheme produce more accurate result with less dispersion error as compared to standard compact scheme. The one-dimensional test cases has

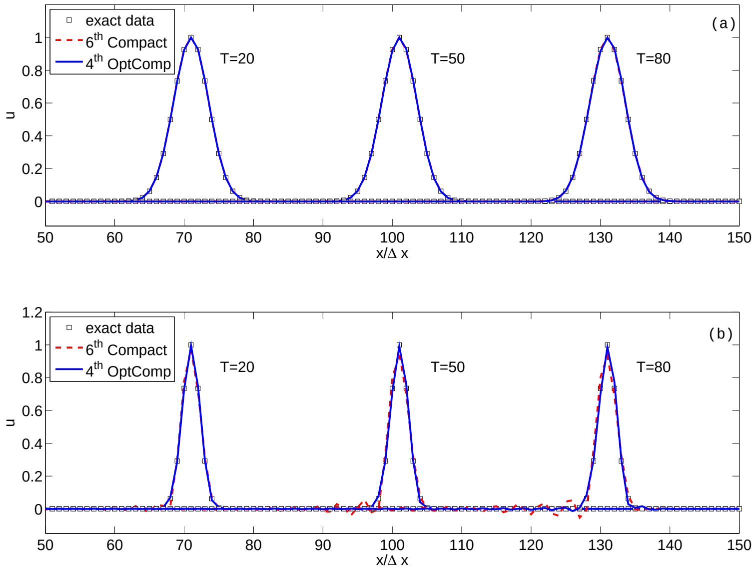

Figure 4.2: Propagation of waves at three time instant, T = 20, 50 and 80. Simulated by sixth-order standard compact scheme and fourth-order optimized compact scheme. (a) b=3; (b) b=1.5.

shown that compact schemes are able to provide more accurate solutions with the cost of longer computational time.

This one dimensional test case clearly demonstrated that compact schemes perform better than explicit schemes at the same order of accuracy. And more importantly, for both explicit and compact schemes, better solution can be achieved by using the optimized schemes where computational cost remains the same since the same stencil size is kept. However, at the same order of accuracy, the price of using compact schemes is usually higher than the explicit schemes. Some extra time is spent on inverting the matrix.

4.2 Sound scattering from circular cylinder

The second test case is selected from the second computational aeroacoustic workshop on benchmark problems [99] (problem 2 in Category I). The problem is considered as a simplified model in which the sound source generated by a propeller is scattered off by the fuselage of an aircraft. The problem is two-dimensional based on the assumption that the fuselage has a cylindrical shape and the noise from propeller is a line source. This problem requires finding the time history of acoustic pressure fluctuation $p(t)$ at three points A($r = 5, \theta = 90^0$), B($r = 5, \theta = 135^0$), C($r = 5, \theta = 180^0$).

The circular cylinder has a radius of $r = 0.5$ and is located at the center of computational domain. The numerical calculation is carried out in a domain between two concentrical cylinders of $r = 0.5$ and $r = 10.5$. Since the problem is symmetric, only half of the computational plane ($\theta = 0 \rightarrow \pi$) is considered instead of using the entire azimuthal plane. The computational grid contains 201×201 cells that are equidistant both in the radial and azimuthal direction. This is also a good case to test both wall and far field boundary conditions on a curvilinear mesh.

At time $T = 0$, the initial pressure pulse is located at the position $x = 4$, $y = 0$ and generated by Equation (4.3).

$$p(x, y, 0) = \exp\left[-\ln(2)\frac{(x-4)^2 + y^2}{0.2^2}\right] \tag{4.3}$$

The initial velocities in the radial and azimuthal directions are set to zero such as $v_r = v_\theta = 0$. The linearized Euler equations in a polar frame of reference is written as

$$\frac{\partial}{\partial t}\begin{pmatrix} v_r \\ v_\theta \\ p \end{pmatrix} + \frac{\partial}{\partial r}\begin{pmatrix} p \\ 0 \\ v_r \end{pmatrix} + \frac{1}{r}\frac{\partial}{\partial \theta}\begin{pmatrix} 0 \\ p \\ v_\theta \end{pmatrix} + \frac{1}{r}\begin{pmatrix} 0 \\ 0 \\ v_r \end{pmatrix} = 0 \tag{4.4}$$

In this example, the spatial derivatives are calculated using the fourth-order DRP schemes with seven-point stencils. At the farfield and wall boundaries, the seven-point backward difference DRP schemes are applied. The farfield radiation boundary condition is written as

$$\frac{\partial}{\partial t}\begin{pmatrix} v_r \\ v_\theta \\ p \end{pmatrix} + \frac{\partial}{\partial r}\begin{pmatrix} v_r \\ v_\theta \\ p \end{pmatrix} + \frac{1}{2r}\begin{pmatrix} v_r \\ v_\theta \\ p \end{pmatrix} = 0 \tag{4.5}$$

The radiation boundary conditions are used for three layers of the computational mesh near the farfield boundary, see Figure 3.18. No-slip boundary conditions are applied on the wall boundary where the normal velocity on the wall is set equal to zero. The normal derivatives $\partial v_r/\partial r$ near the wall are also computed by backward schemes. Instead of using entire interior values for evaluating the derivatives, one ghost point is included for each backward scheme near the wall. The computational domain is therefore extended to one ghost point inside the physical wall. The ghost values are calculated by extrapolation using the physical conditions that the normal component of velocity on the wall and the pressure gradient normal to the wall are zero. At the plane $\theta = 0$ and $\theta = \pi$ symmetric conditions are used such as

$$\frac{\partial v_r}{\partial \theta} = 0 \tag{4.6}$$

$$v_\theta = 0 \tag{4.7}$$

$$\frac{\partial p}{\partial \theta} = 0 \tag{4.8}$$

Their derivatives near the symmetric plane are treated as interior points with

$$\begin{pmatrix} v_r \\ v_\theta \\ p \end{pmatrix}_{-j} = \begin{pmatrix} v_r \\ -v_\theta \\ p \end{pmatrix}_{+j} . \tag{4.9}$$

where j represents the azimuthal direction. The instantaneous snapshots of this simulation are shown in Figure 4.3. At time $T = 2$ and $T = 3$ waves propagate in free space without touching any boundary. At time $T = 4$ the wave front reaches the cylinder surface and generates a smaller reflected wave which propagates in the opposite direction as the main wave front. At $T = 6$ the reflected wave is clearly seen, and besides this a third wave is observed near the cylinder which is due to the diffraction of the first wave. At $T = 8$ and $T = 10$ the initial pulse has already reached the out boundary and as expected a smooth transition towards outside is seen.

The time history data of the pressure is compared to the analytical solution from the second CAA workshop [99] at three locations. To obtain the analytical solution of the problem, the velocity potential $\phi(x, y, t)$ is introduced

$$u = \frac{\partial \phi}{\partial x}, \qquad v = \frac{\partial \phi}{\partial y}, \qquad p = -\frac{\partial \phi}{\partial t}. \tag{4.10}$$

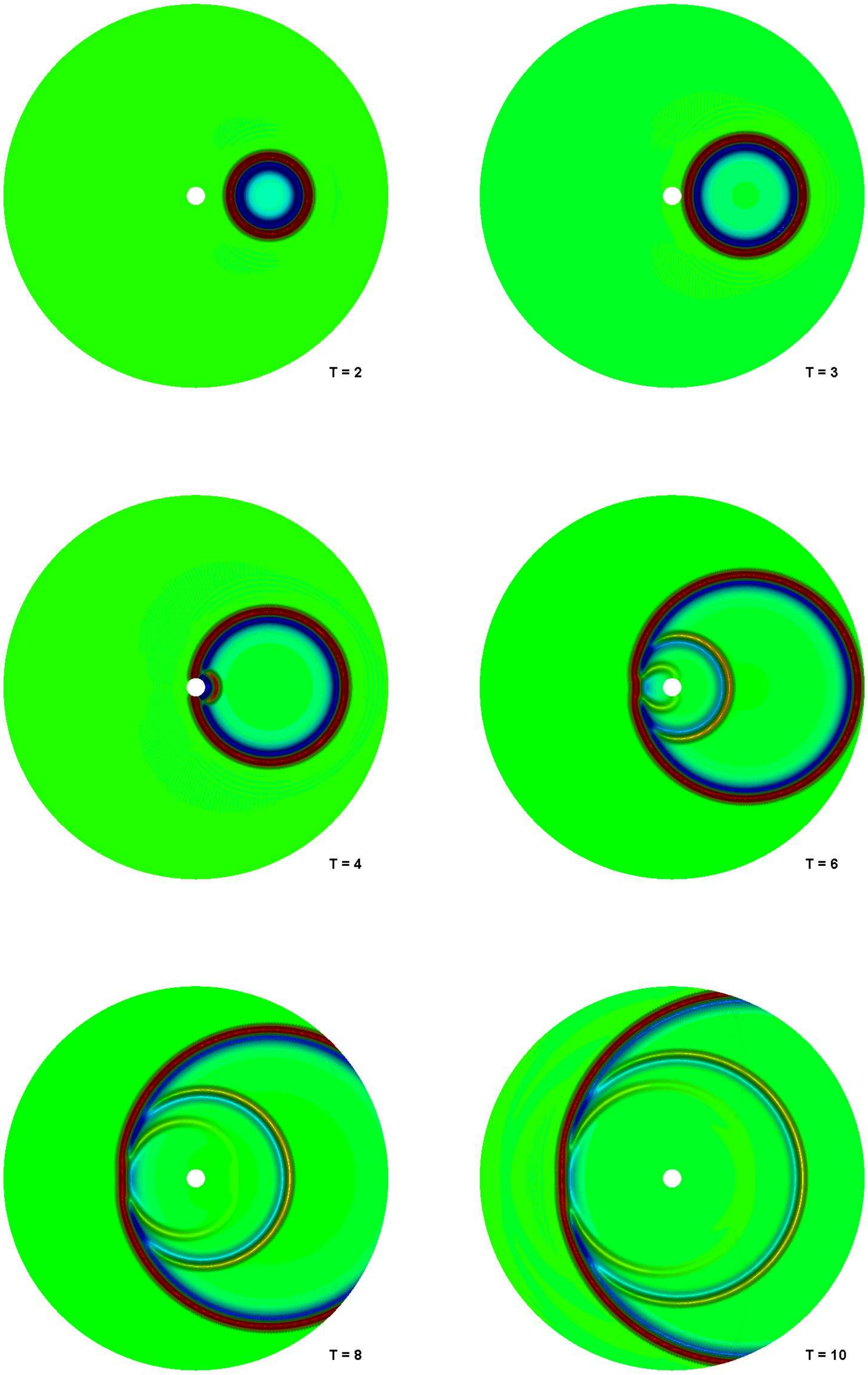

Figure 4.3: Instantaneous acoustic pressure contours at time T = 2, 3, 4, 6, 8 and 10. Contour level ± 0.025.

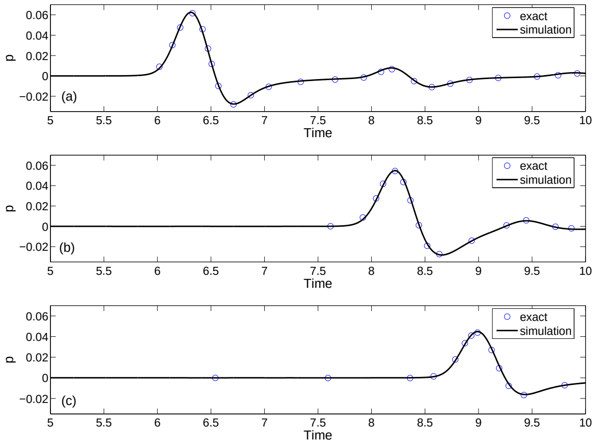

Figure 4.4: Comparisons between computed and exact data. (a) Acoustic pressure at point A ($r = 5, \theta = 90^0$). (b) Acoustic pressure at point B ($r = 5, \theta = 135^0$). (c) Acoustic pressure at point C ($r = 5, \theta = 180^0$).

By using this relation to the governing equation in a polar frame (Equation (4.4)), the wave equation based on the velocity potential is obtained

$$\frac{\partial^2 \phi}{\partial t^2} - \left(\frac{\partial^2 \phi}{\partial r^2} + \frac{1}{r}\frac{\partial \phi}{\partial r} + \frac{1}{r^2}\frac{\partial^2 \phi}{\partial \theta^2} \right) = 0. \tag{4.11}$$

The equation was solved by the method of superposition by letting

$$\phi(r, \theta, t) = \phi_i(r, \theta, t) + \phi_r(r, \theta, t). \tag{4.12}$$

where ϕ_i and ϕ_r are the incident wave and the reflected waves. The solution of the velocity potential is given in [99] and the sound pressure field is calculated as $p(r, \theta, t) = -\frac{\partial \phi}{\partial t}$.

In Figure 4.4, it is seen that at the three reference points A, B and C, good agreement is obtained between the simulated and the exact data. In Figure 4.4 (a), the wave crest indicates the arrival of the incident wave from the initial position $x = 4$ and $y = 0$. At time about $T = 8.2$, the reflected wave arrives at the receiver point A. Very similar situation is shown in Figure 4.4 (b) where the receiver is located at $\theta = 135^0$. In Figure 4.4 (c), one might observe that the wave amplitude is much decreased as compared to point A and B. This is due to the effect of wave reflection and diffraction while the initial wave approaches the cylinder. Since the total sound energy must be conserved, the incident wave (at $\theta = 180$) will lost part of energy to produce the other two smaller waves.

4.3 Sound generation by a co-rotating vortex pair

In this test case, sound generation from co-rotating vortices is simulated. The co-rotating vortices constitute a simple model of sound generation from vortical flows. Vortical flows such as vortex shedding behind cylinders and airfoils are typical examples of noise sources. For instance, wake behind a circular cylinder contains vortex pairs and they are noise sources.

Since it is the vortical flow which is responsible for the sound generation, the flow field needs to be studied first. The schematic of two point vortices is given in Figure 4.5. The circulation of the vortices is Γ which indicates the strength of the vortices. The vortices are spinning around each other on a circle with a radius of r_0. The angular rotational speed is $\omega = \Gamma/(4\pi r_0^2)$, the period of rotation is $T = 8\pi^2 r_0^2/\Gamma$, and the rotating Mach number is $M_a = \Gamma/(4\pi r_0 c_0)$.

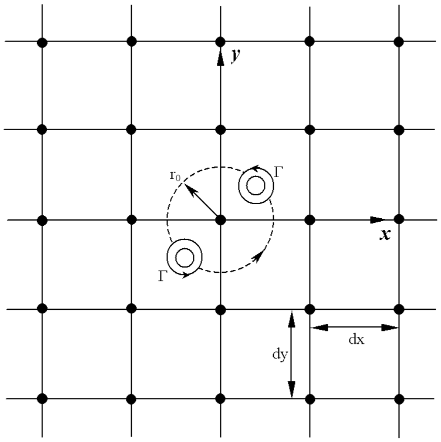

Figure 4.5: Sketch of the vortex pair.

The theory of vortex induced sound has been studied by Powell [100] early in 1964. Later on, the analytical solution of acoustic pressure field was given by Müller and Obermeier [101] using the method of matched asymptotic expansions (MAE). Some numerical simulations were carried out in recent years, among those, Lee et al. [102] and Ekaterinaris [103] did the calculation using MacCormack's predictor corrector scheme and high-order upwind scheme, respectively. In the present numerical study, sixth-order optimized compact schemes are applied for two dimensional acoustic equations which is given as

$$\frac{\partial}{\partial t}\begin{pmatrix}\rho' \\ \rho u' + \rho' U \\ \rho v' + \rho' V \\ p'\end{pmatrix} + \frac{\partial}{\partial x}\begin{pmatrix}\rho u' + \rho' U \\ \rho(2Uu' + u'^2) + \rho' U^2 + p' \\ \rho(Vu' + Uv' + u'v') + \rho' UV \\ c^2(\rho u' + \rho' U)\end{pmatrix}$$

$$+\frac{\partial}{\partial y}\begin{pmatrix}\rho v' + \rho' V \\ \rho(Vu' + Uv' + u'v') + \rho' UV \\ \rho(2Vv' + v'^2) + \rho' V^2 + p' \\ c^2(\rho v' + \rho' V)\end{pmatrix} = \begin{pmatrix}0 \\ 0 \\ 0 \\ -\frac{\partial P}{\partial t}\end{pmatrix}. \tag{4.13}$$

The acoustic equations were derived by incompressible/acoustic splitting technique [1, 2], see also Section 2.7. Therefore the present study is a numerical test for both high-order compact schemes and the incompressible/acoustic splitting method. In Equations (4.13) , U, V and P are incompressible parameters that are required as input for the acoustic equations. These flow variables are usually obtained by solving the incompressible flow field. However, in this case the incompressible flow field is described analytically as shown below

$$U - iV = \frac{\Gamma}{i\pi}\frac{z}{z^2 - b^2} \tag{4.14}$$

$$P = P_0 + \rho_0\frac{\Gamma\omega}{\pi}\Re\left(\frac{b^2}{z^2 - b^2}\right) - \frac{1}{2}\rho_0(U^2 + V^2). \tag{4.15}$$

The incompressible velocities and pressure field are given in Equations (4.14-4.15) and they are used as the inputs to the acoustic Equation (4.13) at each time iterations. In Equation (4.14) and (4.15), $z = x + iy = re^{i\theta}$, $b = re^{i\omega t}$ are complex functions and $\Re$ indicates the real part of the complex number.

A plot of the incompressible U velocity field is shown in Figure 4.6 and the plots for V and P are quite similar to U. Figure 4.7 is the resulting sound pressure field. It is seen that there is a large extend of acoustic field compare to the flow field. It is natural that the flow field is solved with a mesh that clustered to the vortex pairs. However, it can be seen from sound pressure plot that sound waves extended throughout the computational domain and nearly have same order of magnitudes. Therefore, the mesh should not be too coarse in the farfield region to maintain wave propagation. Also what can be seen in the acoustic pressure plot is that the amount of energy of sound field is relatively small. Errors can easily arise due to numerical discretization or boundary conditions which may become new sound source.

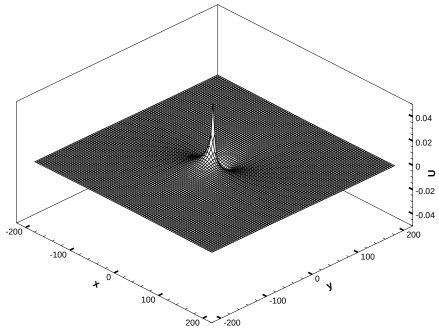

Figure 4.6: Incompressible velocity U.

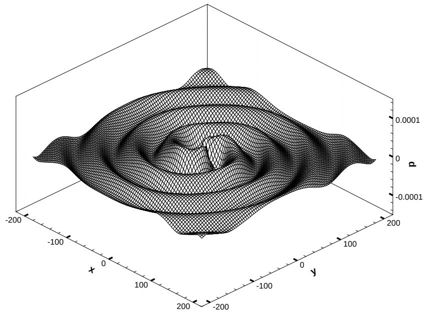

Figure 4.7: Sound pressure p'.

The computational domain is covered with a equi-distant Cartesian mesh, as shown in Figure 4.5. In this case, farfield boundaries are located at the four edges of the computational domain. At the far field boundaries, the radiation boundary conditions of Tam and Webb [12] are used, see Equation (3.69) to Equation (3.72). The group velocity in this case is

$$V_\theta = (U + u')\cos(\theta) + (V + v')\sin(\theta) + c_0 \tag{4.16}$$

where θ is the polar angle and c_0 is the sound speed.

The analytic solution by Müller and Obermeier [101] are used to validate the numerical simulation, the fluctuating pressure is given by

$$p' = \frac{\rho_0 \Gamma^4}{64\pi^3 r_0^4 c_0^2}\left[J_2(kr)\cos(2(\omega t - \theta)) - Y_2(kr)\sin(2(\omega t - \theta))\right] \tag{4.17}$$

where k is the wave number, J_2 and Y_2 are the second-order Bessel function of first and second kind, respectively. In the present numerical simulation, the circulation of the vortices Γ is chosen as $2\pi/10$, and both the sound speed c_0 and the core radius r_0 are set to one. The numerical and analytic solutions are plotted together in Figure 4.8 which shows data along the diagonal direction. General agreement is found between simulated and analytic data except at locations near vortex core where a singular point exists ($1/r \to \infty$). However, the near core region can not be accurately simulated due to the singularities of flow field and the analytical solution (Equation (4.17)) is

$p' = -\infty$ at the core center, see Figure 4.8. In some other numerical studies, vortex core models are used to simulate the core region to obtain smooth solutions, such core models are referred to in [104, 105]. Another comparison is shown in Figure 4.9 where the sound pressure plot shows good agreement between simulated (lower half the domain) and analytic results (upper half of the domain) both in magnitude and phase.

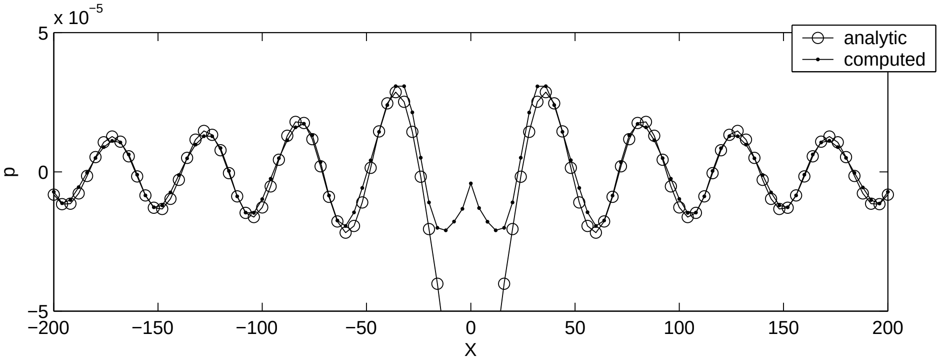

Figure 4.8: Comparison of acoustic perturbation between simulation and analytic data along diagonal direction.

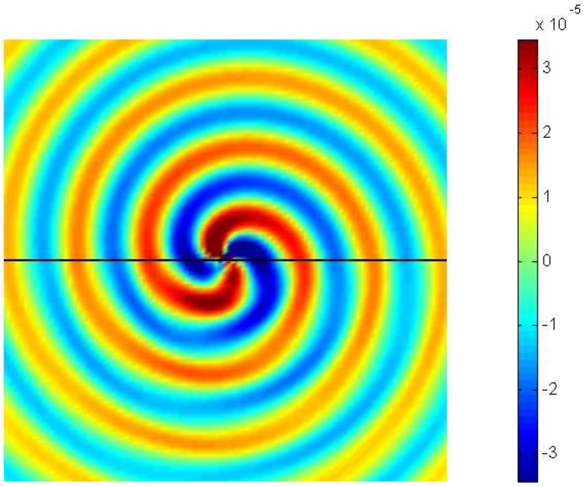

Figure 4.9: Comparison of the analytic (upper) and computed (lower) sound pressure field.

Chapter 5

2D flow and acoustic analysis

In this chapter, the two-dimensional flows and acoustic wave generation for flow past a circular cylinder are solved with EllipSys2D code. Both circular cylinder in a uniform mean flow and in an oscillatory flow are studied separately. The study is continued with noise generation from a two-dimensional NACA 0012 airfoil due to both laminar and turbulent flows.

5.1 Circular cylinder in a uniform mean flow

The flow around a circular cylinder is a problem of interest in fundamental fluid mechanics and experimental studies of cylinder flow are still one of the popular topics. Study of the flow and acoustic field around cylinder was pioneered by Strouhal [106] early in 1878. It was found in his experiments that the sound frequency from the cylinder is related to the Strouhal number defined as $S_t = fD/U_\infty$. If the cylinder diameter $D = 1$ and free stream velocity $U_\infty = 1$, the sound frequency f should take the same value as Strouhal number. Later in this section it will be shown that the sound generation of a circular cylinder is mainly due to the fluctuating lift which has the same frequency as the Kármán vortex street. Recent studies of low Reynolds number flow and acoustics around a circular cylinder have been carried out by Shen and Sørensen [9, 11], Kim and Lee [89], Inoue and Hatakeyama [8], Ewert and Schröder [108], Seo and Moon [109, 110].

In the present numerical simulation, flow past a circular cylinder at a Reynolds number $Re = 200$ and a Mach number $M = 0.2$ is considered. The computational domain extends radially away from the cylinder walls about 50 cylinder diameters. The O-mesh consists of 256 cells in the circumferential direction and 128 cells in the radial direction given a total 32768 grid points. The mesh is equally spaced in the circumferential direction and exponentially stretched in the radial direction. Time integration method for the acoustic field is fixed to a fourth-order Runge-Kutta method for all simulations and various high-order spatial schemes are analyzed. For convenience both the cylinder diameter, the free stream velocity in x-direction and fluid density is set to unity.

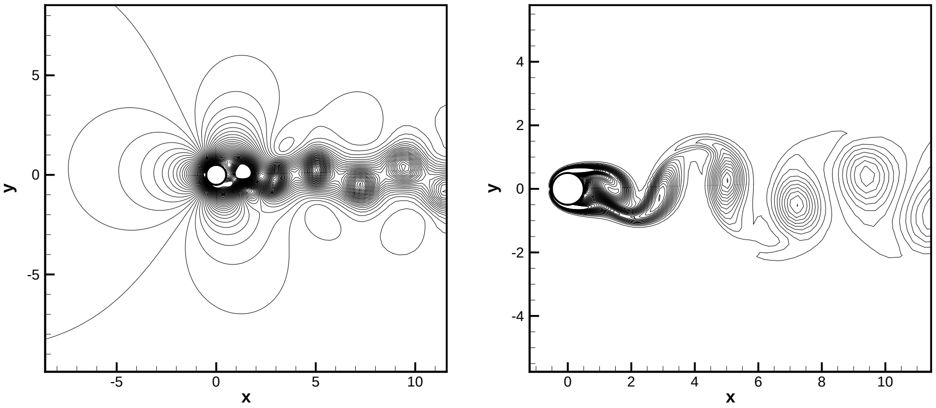

Figure 5.1: Incompressible pressure (left) and vorticity field (right).

The resulting flow field is shown in Figure 5.1 which are the incompressible pressure and vorticity contours. The forces acting on the cylinder surface are shown in Figure 5.2 in terms of lift and drag as function of time, these are calculated by integrating the pressure and shear stress distributions along the cylinder surface. The vortex shedding does not occur for a considerable long time. At non-dimensional time about 100 the shedding initiated and flow entered into a periodic state. After the periodic mode is set in, the Strouhal number is found to be $S_t = 0.1936$. For vortex shedding from a circular cylinder, an empirical relation was proposed by Fey et al. [107] which is given as

$$S_t = 0.2684 - 1.0356/\sqrt{Re}. \tag{5.1}$$

From this relation the Strouhal number is found to be 0.195 at $Re = 200$ which is quite close to the computed value.

The instantaneous contour plot of the fluctuating pressure p' is shown in Figure 5.3 at T = 200. The acoustic waves are seen to propagate in the direction normal to the mean flow which is related to the lift force on the cylinder. Time histories of the acoustic pressure are shown in Figure 5.4. The signal with higher magnitude (solid line) is measured at about 10 diameters away from cylinder along the y-direction. The dashed line has smaller magnitude which is measured at the same distance but an angle

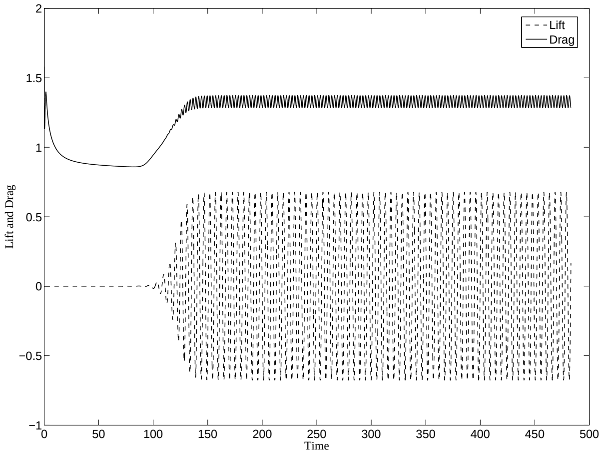

Figure 5.2: Time history data of lift and drag for flow past a circular cylinder at Re=200.

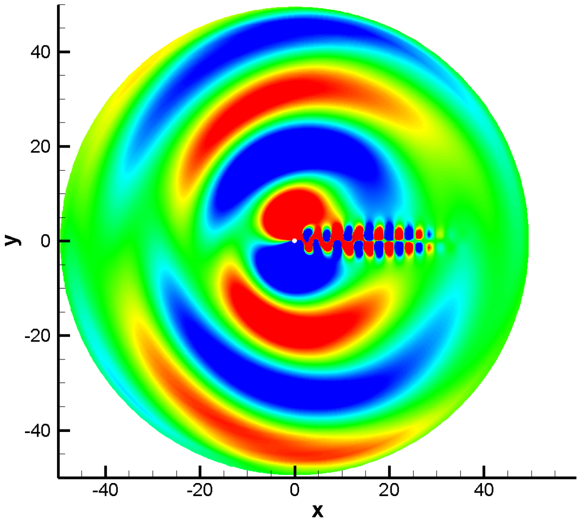

Figure 5.3: Snapshot of fluctuating pressure p' for flow past a circular cylinder at Re=200, M=0.2.

of 45 degrees with respect to y-axis. It is seen that the recorded acoustic signals propagate periodically and conserves the amplitude even after quite long time. The time series data are used for Fourier analysis to investigate their relation with unsteady forces. Figure 5.5 shows the spectra for lift, drag and acoustic signal. For comparison purposes, the magnitudes are normalized and it is the frequency band of interest here. First we see that the frequency of lift (shedding frequency) is about 0.194 and the drag frequency is about 0.385. The drag frequency is double of the frequency of lift force which is consistent with theory. Secondly, for the acoustic signal, the first two frequency modes clearly match the frequency of lift and drag signal. According to Strouhal [106], the dominant frequency of acoustic radiation is the Strouhal number which is verified in the present simulation. Moreover, the contribution of drag force is negligibly small as depicted in Figure 5.5. The solution obtained with the sixth-order optimized compact scheme is compared with a second-order finite difference/finite volume solution by Shen and Sørensen [9, 11]. In Figure 5.6, it is seen that solution of the high-order scheme has a amplitude about 5% higher than the second-order scheme. Also there is a phase difference of the two solutions due to the use of different time marching schemes (RK4 for the high-order scheme and Crank-Nicolson for the second-order method). A comparison using different high-order finite difference schemes are also compared, see Figure 5.7. Three schemes are selected for comparison, the fourth-order DRP schemes (7-point stencil), the tridiagonal eighth-order standard compact scheme (7-point stencil on right hand side) and the tridiagonal optimized sixth-order compact scheme (7-point stencil on right hand side). The performance of three schemes is similar where advantage of higher-order scheme can be seen.

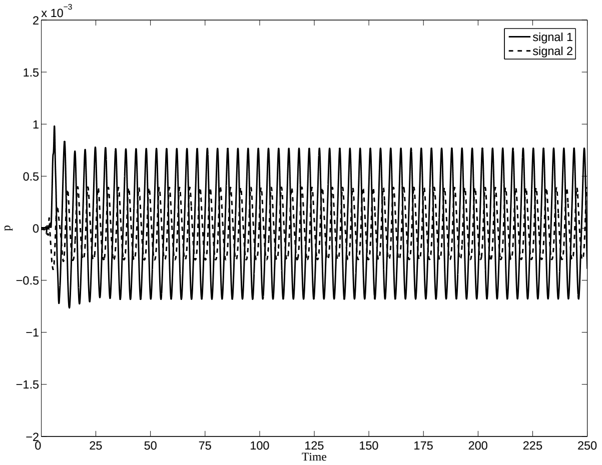

Figure 5.4: Time history of acoustic pressure for flow past a circular cylinder at Re=200, M=0.2.

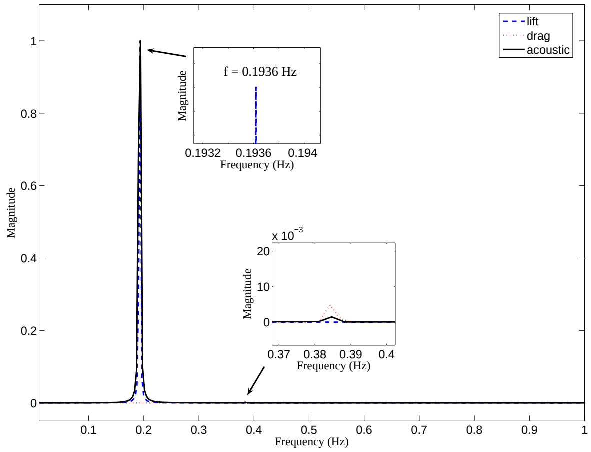

Figure 5.5: Aerodynamic force and acoustic pressure spectrum.

The dimensionless time step $\Delta t = 0.001$ is generally used in the present simulation. The effect of using different time step is shown in Figure 5.8 where solutions obtained by $\Delta t = 0.002$ and $\Delta t = 0.0005$ are compared. The effect of increasing time step by four times larger does not significantly affect the solution, the amplitude of the acoustic wave is decreased about 2.5%.

In case of high Reynolds number flow, the grid size can be significantly smaller, so the time step for acoustic simulation also becomes quite small. One way to make the simulation more efficient is to use a few subiterations for the acoustic simulation. For example, a time step Δt is used for flow simulation and n-iteration is performed for acoustic calculation with a time step $\Delta t/n$. In this way the flow equations does not need to be solved with the same time step as for the acoustic equations. The assumption is made that the required flow quantities at time $t + \Delta t/n$ are calculated by linear interpolations. The application of using acoustic subiteration is seen in Figure 5.9 where solutions from the two cases are very close. Different high-order filter schemes are available in the acoustic solver, the acoustic time history data show that the wave amplitudes are weakly affected by filter schemes. A closer look of filter schemes is shown in Figure 5.10 where both the sixth-order and tenth-order filters produce very similar results. Finally, the directivity pattern of cylinder noise is measured at a radius of about $r = 15$. From the figure, the radiation is mainly in y-direction and the effect from the fluctuating drag is small.

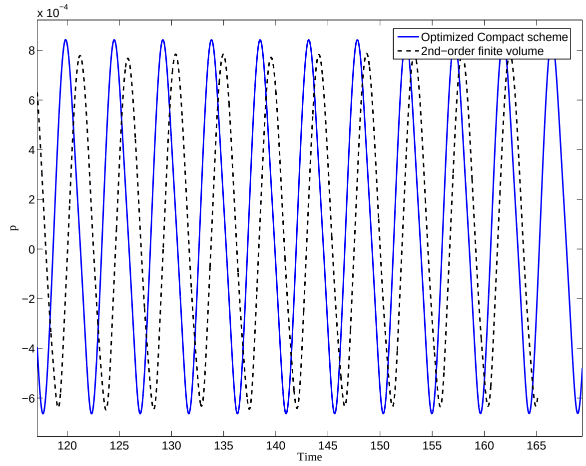

Figure 5.6: Time history acoustic pressure calculated with: (1) sixth-order optimized compact schemes and (2) second-order finite volume method.

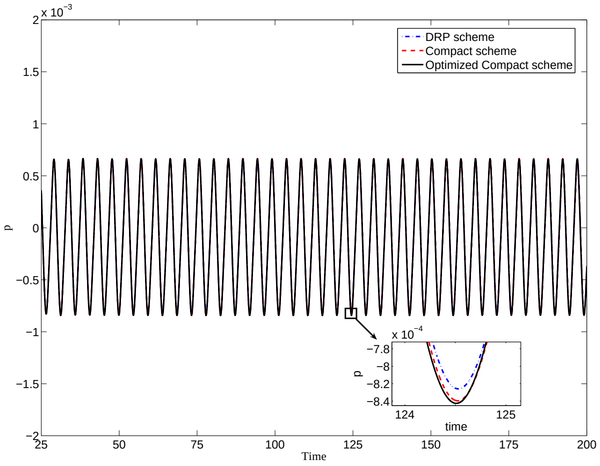

Figure 5.7: Time history acoustic pressure calculated with: (1) Fourth-order DRP scheme; (2) Eighth-order compact scheme; (3) Sixth-order optimized compact scheme.

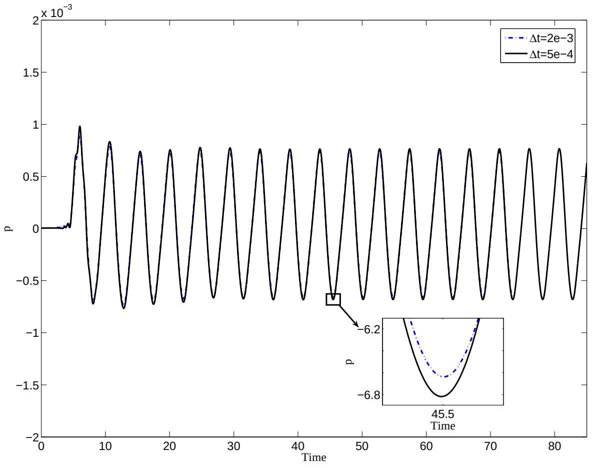

Figure 5.8: Time history acoustic pressure with two different time steps.

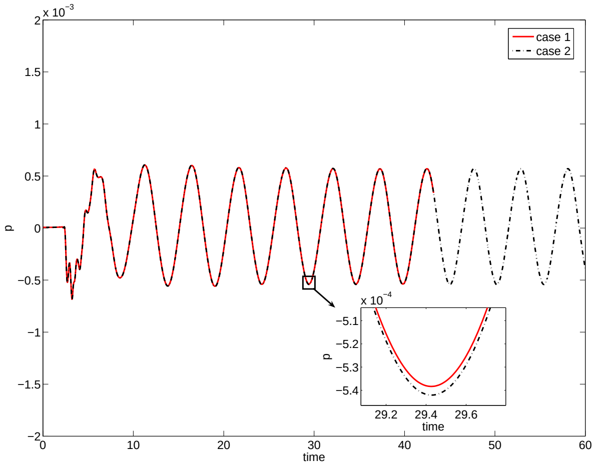

Figure 5.9: Time history acoustic pressure. (case 1) acoustic iteration = 1 and (case 2) acoustic iteration = 2.

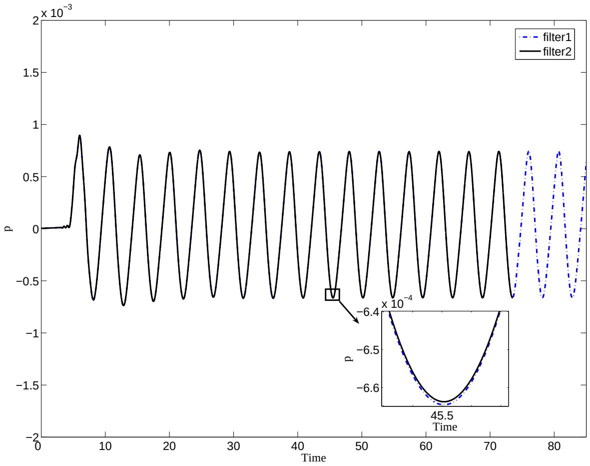

Figure 5.10: Time history acoustic pressure. (filter 1) sixth-order filter and (filter 2) tenth-order filter.

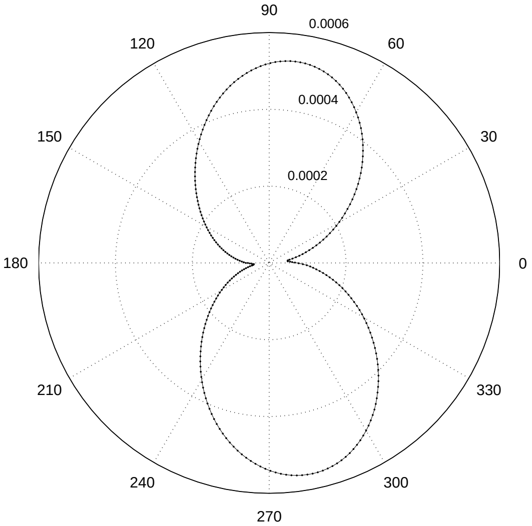

Figure 5.11: Sound directivity.

5.2 Circular cylinder in an oscillatory flow

In this section, flow and acoustic simulations are carried out by considering a two-dimensional flow past a cross-flow oscillating circular cylinder (inflow direction is orthogonal to the oscillating direction). The study is an extension of previous section and the relation of excitation frequency and acoustic spectra are of our interest here.

Low-Reynolds-number flow around an oscillating circular cylinder has been a popular fluid mechanics topic for the last few years. A physical model could be involved with the offshore engineering, such as tower-water interaction of an offshore wind turbine tower. It has been recognized for many years that the frequency of the external oscillation has a significant influence on the vortex shedding frequency on the cylinder and therefore changes the dynamic force behavior on the cylinder. These phenomena were documented by many researchers such as numerical study by Gu et al. [111], Lu & Dalton [112], Blackburn & Henderson [113] and Uzunoğlu et al. [114], and experimental study by Ongoren & Rockwell [115], Williamson & Roshko [116] and Blackburn & Melbourne [117]. The focus of the present study is the associated sound generation of oscillating cylinder, a subject that has not been treated in the previous studies.

Here we consider a flow at a Reynolds number of 500 and with a fix motion of amplitude of $A_e = 0.25D$ where $D = 1$ is the cylinder diameter. The simple harmonic cross-flow oscillation is given as

$$y_e = A_e \cos(2\pi f_e t) \tag{5.2}$$

where f_e is the oscillating frequency. Therefore, the excitation velocity is defined as

$$U_e = dy_e/dt \tag{5.3}$$

For a body moving in an incompressible fluid, Price and Tan [118] showed that the Navier-Stokes equations formulated in a moving frame reference attached to the body are given in terms of disturbed fluid velocity and the mean pressure such as

$$\frac{\partial U_i}{\partial t} + \frac{(\partial U_i \tilde{U_j})}{\partial x_j} = -\frac{1}{\rho_0}\frac{\partial P}{\partial x_i} + \nu \frac{\partial^2 U_i}{\partial x_i \partial x_j} \tag{5.4}$$

$$\frac{\partial U_i}{\partial x_i} = 0. \tag{5.5}$$

This formulation is quite similar as the standard incompressible equation such as Equation (2.21). In Equation (5.2), P, ρ_0 and U_i are the incompressible pressure, the density and the velocity components, respectively. And $\tilde{U_j} = U_j - U_e$ is the relative velocity seen from the body.

First, flow around a stationary cylinder at $Re = 500$ is simulated and a Strouhal number of $f_o = 0.218$ is found. Next, flow around an oscillating cylinder is simulated for three oscillating frequencies, $f_e = 0.22, 0.23$ and 0.25, corresponds to $f_o/f_e = 1.009, 1.055, 1.147$. If in such cases the Strouhal frequency is not the dominant frequency, then we shall see the changes of acoustic spectra. The results of the flow simulations are presented by time history data of lift and drag. These flow simulations were performed for a dimensionless time of 1000 which is quite long. The long time period of simulations are necessary since C_d and C_l never appear periodic, see Figure 5.12 and Figure 5.13. In the case that the oscillating frequency is very close to the vortex shedding frequency ($f_o/f_e = 1.009$), the fluctuation of lift and drag is most distinguishable. For all the three cases, the flow fields are slightly chaotic seen by the force signals. As the oscillating frequency increases, lift and drag signals tend to be periodic since the external force becomes the driving force.

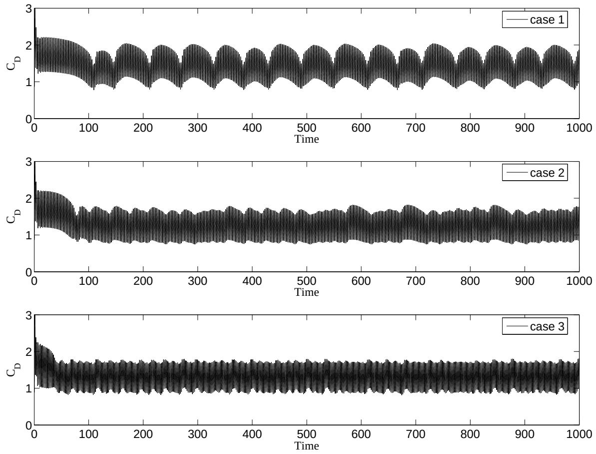

Figure 5.12: Time history drag. case 1: $f_e = 0.22$ Hz; case 2: $f_e = 0.23$ Hz; case 3: $f_e = 0.25$ Hz.

The acoustic pressure signals are recorded at 10 diameters way from cylinder along the y-direction for three oscillating cylinder cases. The time

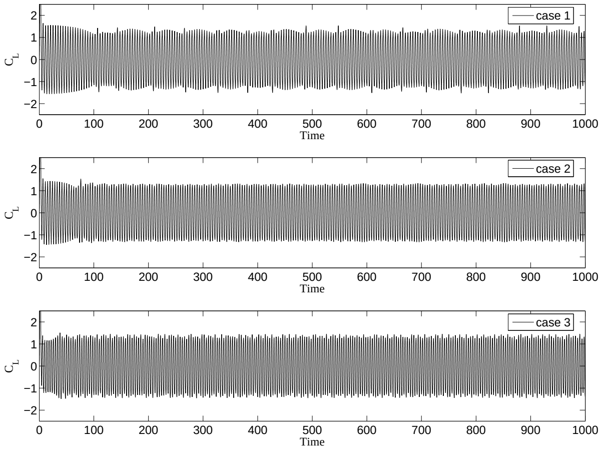

Figure 5.13: Time history lift. case 1: $f_e = 0.22$ Hz; case 2: $f_e = 0.23$ Hz; case 3: $f_e = 0.25$ Hz.

history acoustic pressure values are plotted in Figure 5.14. Again the acoustic signals are non-periodic as expected. The acoustic signals are in the same range while in the case $f_e = 0.23$ the amplitude is slightly higher which implies stronger second harmonics as compared to other two cases.

As an example, the acoustic pressure contour at $f_e = 0.25$ is shown in Figure 5.15. The sound still propagates radially away from the cylinder and new contribution is the down wash and up wash of the waves which can be seen from the plot. The vorticity contours are shown in Figure 5.16 at the maximum and minimum excursion positions of the cylinder. It can be seen that with the external excitation the wake vorticity moved closer to the cylinder which was also discussed by [112]. It may also be noted that the vorticity are not alined in the wake such as in a classical Kármán vortex streets.

We also look at acoustic spectra to see the effects of external oscillation. Such an example is given at $f_e = 0.25$ where acoustic signals at four positions ($\theta = 0, \pi/2, \pi, 3\pi/2$) are recorded. The frequency distribution is the same for all the four signals, see Figure 5.17. The figure clearly shows that the first harmonic has the same frequency as the oscillation frequency, and that the second and the third harmonic exists at a frequency of 0.5 Hz and 0.75 Hz, respectively. Therefore it can be concluded that the dominant frequency is not the Strouhal frequency but the oscillating frequency.

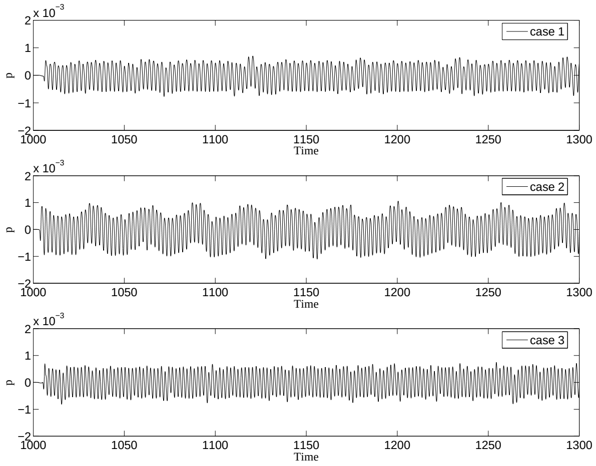

Figure 5.14: Time history acoustic pressure. case 1: $f_e = 0.22$ Hz; case 2: $f_e = 0.23$ Hz; case 3: $f_e = 0.25$ Hz.

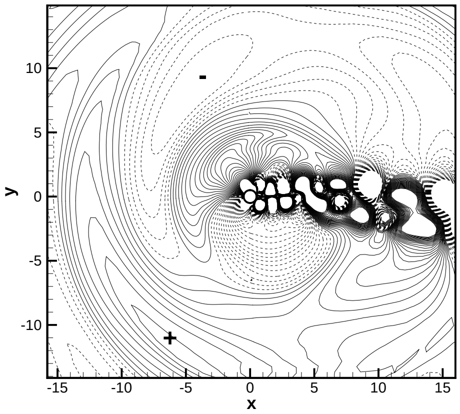

Figure 5.15: Acoustic pressure contour at $f_e = 0.25$.

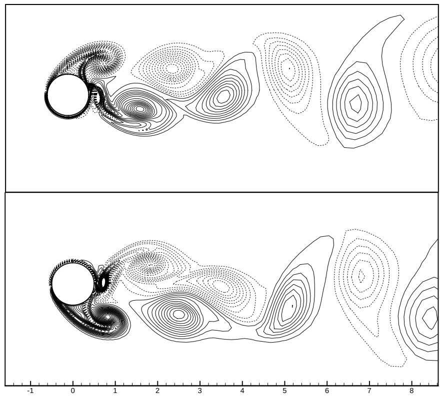

Figure 5.16: Vorticity field at $f_e = 0.25$.

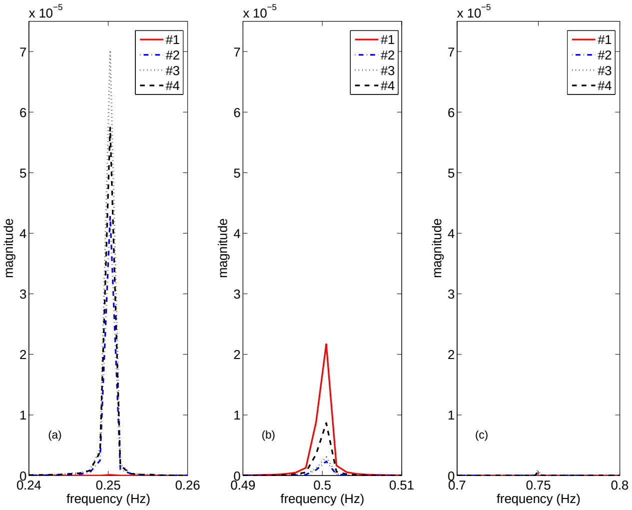

Figure 5.17: Acoustic pressure spectra at four receiver points with external oscillation $f_e = 0.25$ Hz.

Figures 5.18, 5.19 and 5.20 show more information about the correlation between the spectra of forces and acoustic signals. The general trend is that the oscillating frequency dominates both the flow and the acoustics behavior. Moreover, the second harmonics are quite strong, as compared to the non-oscillating case (see Figure 5.5 for comparison). Since the second harmonic of the flow is not negligible, the influence must be shown on the acoustic solution. In Figure 5.18, we see that at frequency of 0.44 Hz the second harmonic of acoustic signal has the energy about nearly 60% of the first harmonic which produced a totally different acoustic field.

A short conclusion from two-dimensional flow and acoustic study is that the acoustic solution is closely correlated with unsteady forces on the cylinder. The dominant unsteady forces (lift or drag) created by the flow field also dominate the acoustic field. The main part of the acoustic energy comes from the dominant force and the rest of the energy is from other sub-harmonics. The magnitude of sub-harmonics were negligible in the case of a flow over a stationary cylinder (see Figure 5.5). By introducing an external oscillation to the cylinder, the second harmonic can be easily distinguished on the sound spectrum (see Figure 5.17). The reason was found by comparing the force spectra to the sound spectra (see Figure 5.18-5.20) where the magnitudes of drag forces have increased significantly. Therefore the distribution of sound energy is proportional to the energy of force distribution.

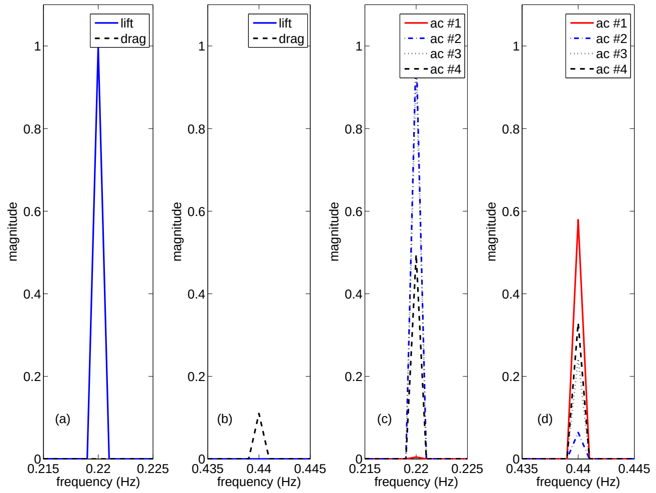

Figure 5.18: Comparison of lift, drag and acoustic pressure spectra with external oscillation $f_e = 0.22$ Hz.

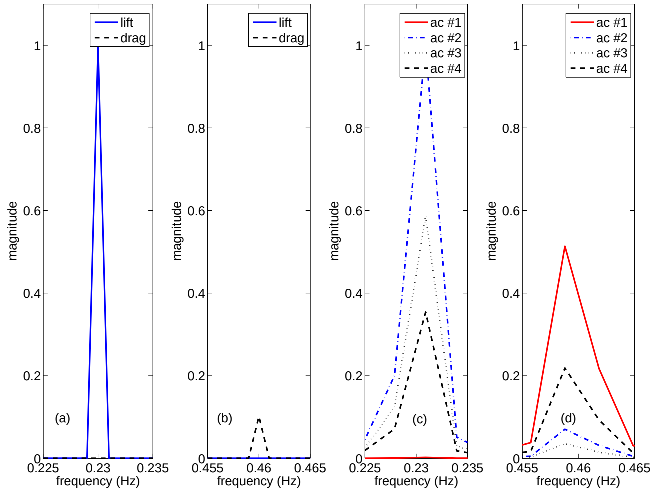

Figure 5.19: Comparison of lift, drag and acoustic pressure spectra with external oscillation $f_e = 0.23$ Hz.

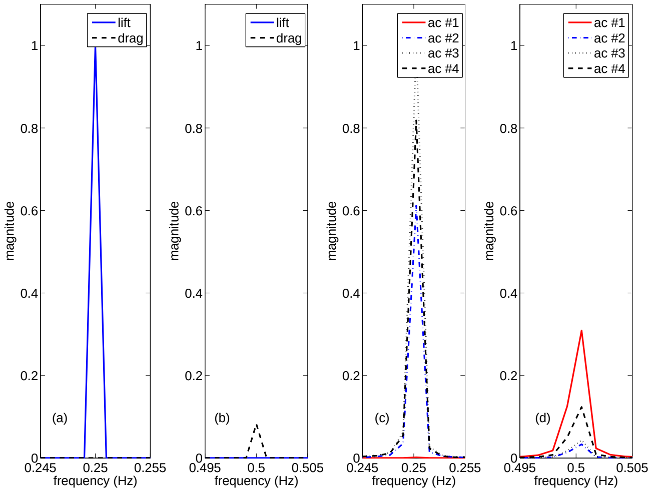

Figure 5.20: Comparison of lift, drag and acoustic pressure spectra with external oscillation $f_e = 0.25$ Hz.

5.3 Low Reynolds number airfoil flow

Airfoil noise prediction is generally of more interests in practice. Numerical simulations of noise from aircraft, wind turbine and turbo-machinery are based on information of sound generation from single airfoils. The computational case considered in this section is flow past a 2D NACA 0012 airfoil at a Reynolds number 200. The angle of attack is 20 degrees and the flow Mach number is 0.2. The flow solver is again a second-order finite volume method. The acoustic computations are performed with the sixth-order optimized compact finite difference scheme and for time advancement the fourth-order Runge-Kutta method is used. A 2D structured body-fitted O-mesh is generated with 9 blocks and 64×64 mesh points in each block. The computational domain extends 50-chord length radially away from the airfoil. The computational grids in the radial direction are exponentially clustered on the airfoil surface and the orthogonal O-grid is constructed by using a conformal mapping, see Shen and Sørensen [119].

The development of the acoustic pressure field is shown in Figure 5.21. Figure 5.21 (a-c) show the initial state of sound fields. The acoustic computation was started at a certain time when flow around the airfoil was fully established. In such a way, the initial acoustic pattern was produced by the sudden impact of flow field. The periodic acoustic waves appear in Figure 5.21 (c) where a positive and a negative noise sources are seen on the airfoil surface. This is due to waves which propagate at opposite phase on the upper and lower side. Figure 5.21 (d) illustrates the fully developed acoustic pressure field at T=20. There are about four wave crests in the computational domain and each wave has a wavelength approximately of 14 chord lengths (see also [11]).

The time history of acoustic pressure signals are plotted in Figure 5.22 at two receiver points ($\theta = 0, 90$ degrees and $r = 10$). After a short period of transients, the acoustic signals became periodic, as also seen in the former case of flow past a circular cylinder. A guess could be that the acoustic frequency is close to or identical with the vortex shedding frequency. This is proved in Figure 5.23 where the non-dimensional lift and acoustic signals are plotted together. Even without performing Fourier transform, it is seen that the two signals have a same frequency (f=0.35). One can also see a small phase lag between the force and the acoustic signals. Since the forces are measured on the airfoil surface, while the acoustic signal are recorded a few chord lengths away from the surface, therefore the time delay (phase lag) is exactly the distance (from the receiver to airfoil surface) divide by the sound speed.

The sound directivity in Figure 5.24 shows that the current directivity

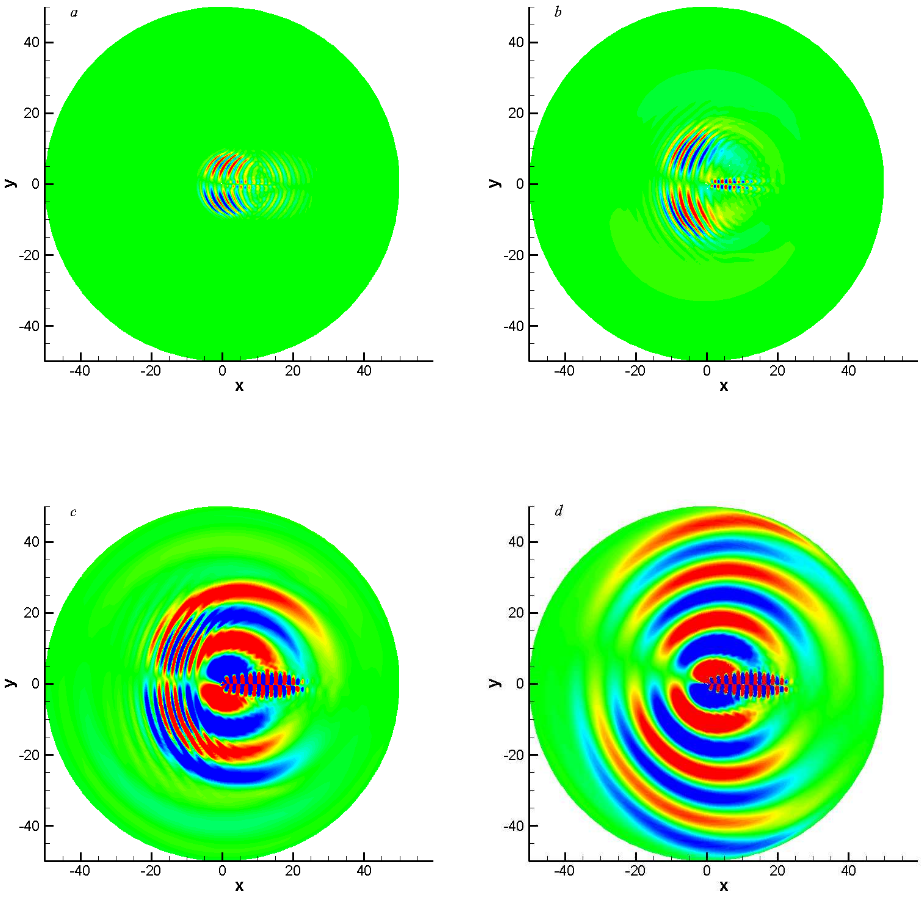

Figure 5.21: Development of acoustic field of NACA 0012 airfoil at Re = 200, M = 0.2. (a) t=2; (b) t=4; (c) t=6; (d) t=20.

pattern is skewed about 20 degrees due to the effect of angle of attack. In Figure 5.25, we show the sound pressure along a straight line $x = 0$. As mentioned earlier there are four wave crests visible and at $y = 0$ the pressure data is discontinues where the airfoil is located. The purpose is to show that the wave amplitudes decay as a function of $r^{-\frac{1}{2}}$ which fits quite well with the two-dimensional acoustic propagation theory. This figure alternatively shows that the acoustic prediction is accurate in the farfield with the present mesh quality. For example, at the region between $r = -40$ and $r = -50$ there are about 10 mesh points supplying one acoustic wave and the wave amplitude still obeys the acoustic theory (the peak fits well with the dashed line).

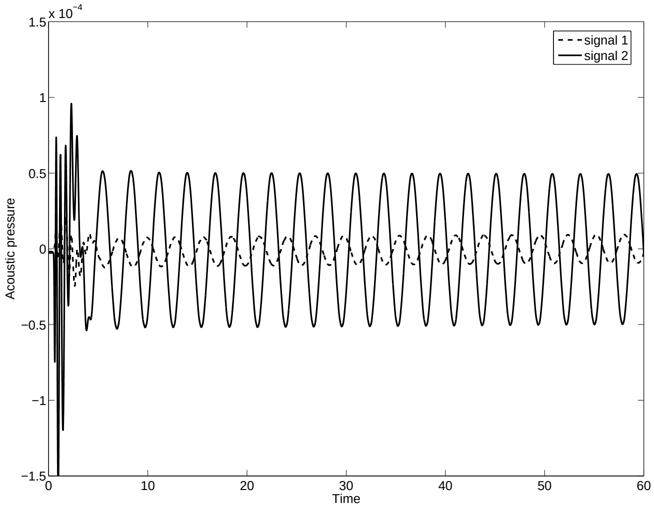

Figure 5.22: Time history of acoustic pressure for flow past NACA 0012 at Re=200, M=0.2.

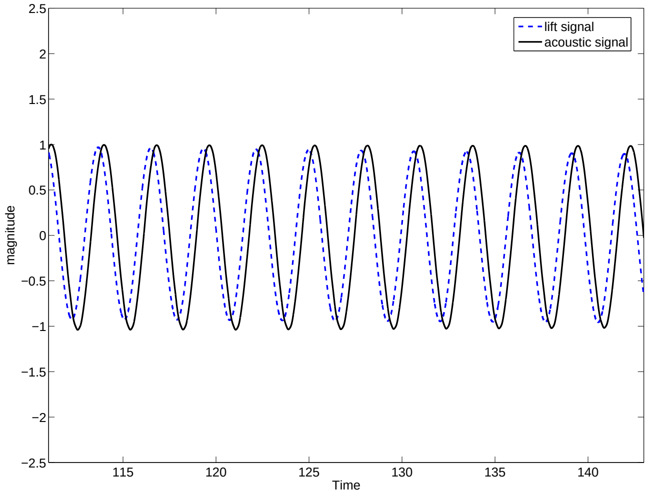

Figure 5.23: Time history of unsteady lift and acoustic pressure for flow past NACA 0012 at Re=200, M=0.2.

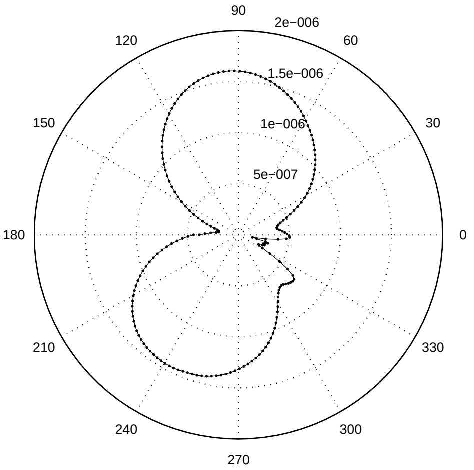

Figure 5.24: Sound directivity of NACA 0012 airfoil.

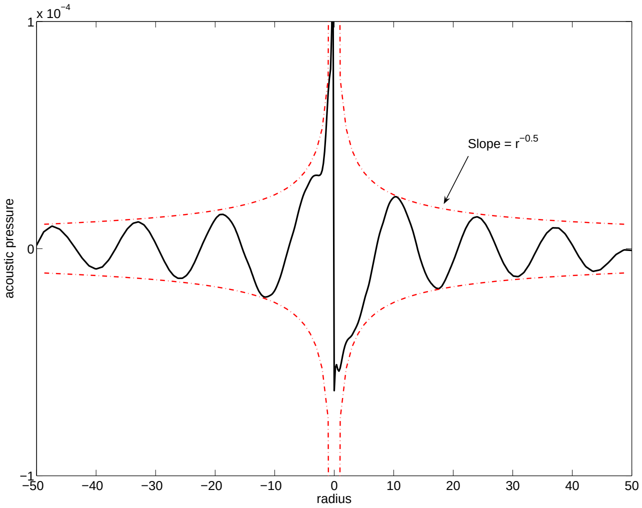

Figure 5.25: Acoustic pressure along x = 0 line, the dashed line shows the law of cylindrical propagation.

5.4 Turbulent airfoil flow

The second case concerns the flow at a Reynolds number 100 000. The angle of attack is 5 degrees and the Mach number is 0.2. The two-dimensional O-mesh is about 20-chord length in radius and contains 96×64×64 mesh points where 96 is the number of blocks, with 64×64 mesh points in each block. There are 8 blocks in the radial direction with the grids clustered on the airfoil surface. The first point way from the airfoil is approximately 10^{-5} of the chord length. The number of blocks in the circumferential direction is 12 with equidistantly distributed meshes. The attempt is first to use a very fine mesh which makes it possible to apply direct simulation of the incompressible NS equations instead of using a turbulence model. Also it ensures that the mesh quality fits the requirement of acoustic computations. As a comparison, another computation was performed on a mesh with only half as many cells and use LES turbulence model. The resulted flow field is almost the same and the acoustic spectra are found similar.

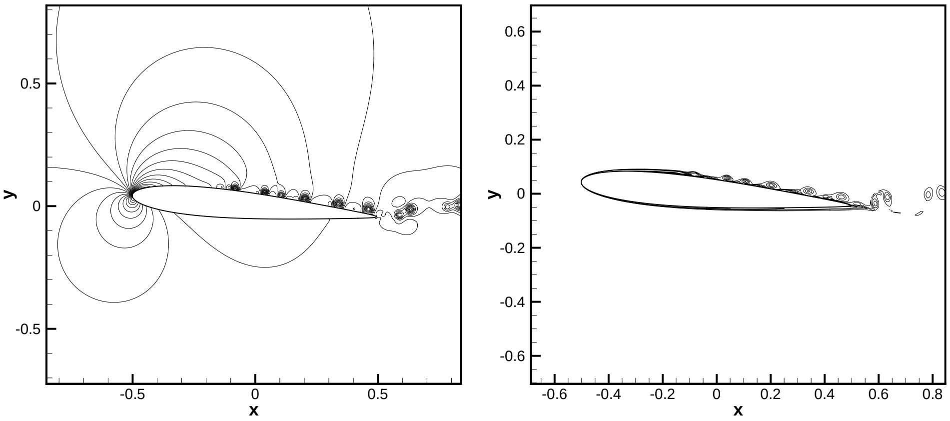

Figure 5.26: Incompressible pressure (left) and vorticity field (right).

The incompressible pressure and vorticity plots are shown in Figure 5.26. It can be noticed that the separation from laminar state to turbulent occurs at the region between $x/c = 0.3$ and $x/c = 0.4$. From the left plot of Figure 5.27 it is seen that the acoustic source regions are closely matched with the separation region where flow is most unsteady. The right hand side of Figure 5.27 shows the snapshot of fully developed acoustic pressure field. The color scale shown in 5.27 is between -10^{-3} and 10^{-3}. Comparing the results to the laminar flow, it is found that there are more wave crests in the turbulent case, indicates noise is generated at higher frequency band. A three-dimensional contour plot of acoustic pressure is shown in Figure 5.28. Noise sources can be seen near the center of the domain and acoustic waves propagate radially towards the outer boundary. Both flow and acoustic simulations are carried out in a non-dimensional way, with the Reynolds number and Mach number as input information and other quantities set equal to unit. Fourier transformation of the acoustic signal is performed at a selected receiver point with real dimensions. Assuming that sound speed is known, e.g. $340m/s$, the dimensional inflow speed U is known based on the given Mach number. The actual chord length is therefore calculated with $c = Re \cdot \nu / U$. Finally, dimensional time is obtained by scaling with a factor of U/c. In such a way the sound pressure level can be computed as

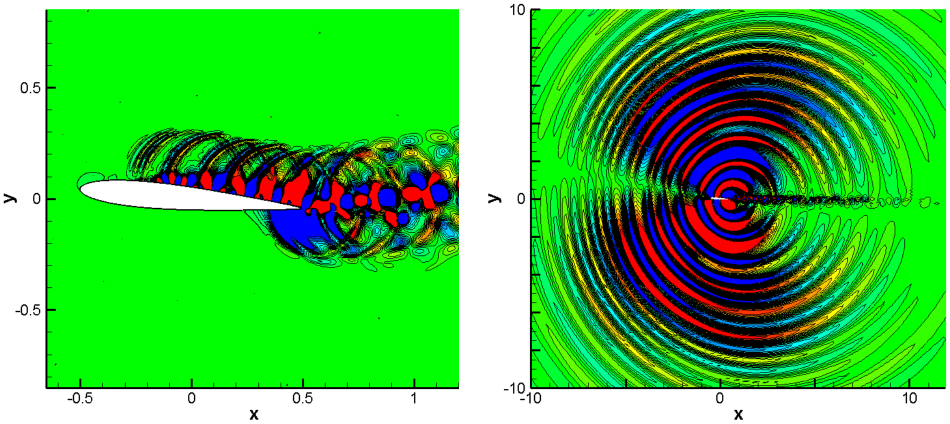

Figure 5.27: Acoustic pressure contour at initial time (left) and after fully developed (right).

$$SPL = 20 \log 10(S/N/P_{const} \cdot 1bar/\sqrt{2}/P_{ref}) \qquad (5.6)$$

where S is the magnitude obtained from Fourier transform of the acoustic time history signal at a receiver point, N is the number of sampling points, $P_{ref} = 2 \times 10^{-5}$ is the reference pressure for noise propagation in a standard atmosphere and $P_{const} = \rho/(\gamma \cdot M^2)$, where γ denotes the specific heat ratio. In the frequency domain, the acoustic spectrum (recorded at a position of $x = 0.5$ and $y = 2.5$) is compared with the force spectrum, see Figure 5.29. In order to compare the spectra in the same plot, the noise and force amplitudes are non-dimensionalized with their maximum values, respectively. Although the lift and acoustic signals are obtained by different sets of equations: the incompressible NS equations and the acoustic equations, their

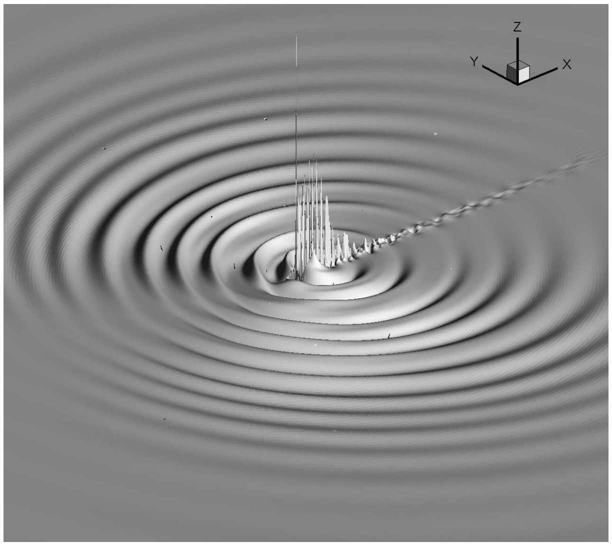

Figure 5.28: Three-dimensional view of acoustic pressure field for flow past NACA 0012 at Re=100 000, M=0.2.

spectra are quite similar, indicating that the dependence between the force fluctuation and the sound generation. It is possible to see from Figure 5.29 that the energy distribution in the acoustic spectrum is very close to that in the lift spectrum particularly at those highest peaks. This proves that in this case the generation of noise is due to the lift force fluctuation on the body surface. According to the theories of Curle [4], turbulent flow produces fluctuating lift on solid bodies and should result in the generation of sound. It is noted that if the unsteady loading acting on a solid body is known as a function of time, the sound frequency distribution can be also estimated. In the present case the drag force is rather small compared to the lift force, therefore the fluctuating lift is the dominant noise source and the contribution from the drag force is negligible small.

The computation was also performed on a coarser mesh with 48×64×64 grid cells, with 6 blocks in the radial direction and 8 blocks in the circumferential direction. The flow field was found to be extremely close for two mesh types where the time average of aerodynamic lift is $C_l = 0.608$. However, in Figure 5.30 difference can be found from acoustic solutions where the dashed line indicates the spectrum obtained by using coarser mesh. The difference is smaller at low frequencies and becomes more significant as frequency increases. The knowledge behind this is that the finer the computational mesh, the more accurate solutions are expected. However, for flows at high Reynolds numbers it is hard to create a mesh that resolves all structures in detail. For three-dimensional acoustic simulations, a balance between grid size and computational costs need to be found.

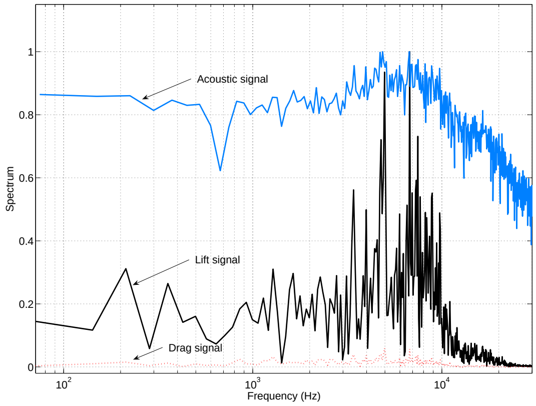

Figure 5.29: Comparison of non-dimensional noise spectrum with lift and drag spectrum ($\alpha = 5^0$).

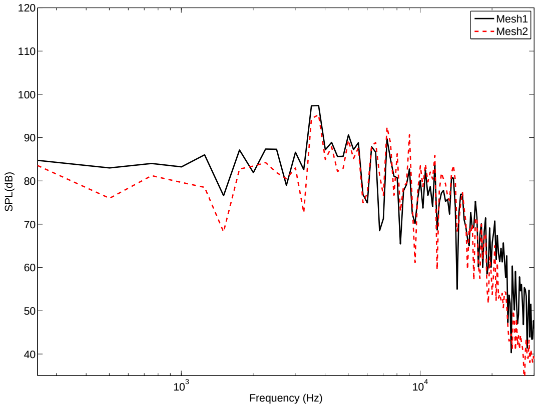

Figure 5.30: Acoustic spectra obtained from two meshes ($\alpha = 5^0$).

In the previous section it has been found that at Re = 200 and $\alpha = 20^0$, only tonal noise is generated by the vortex shedding. And in the present turbulent case, we observed a broad band noise distribution as shown in Figure 5.29 and Figure 5.30. It is understood that the broad band noise was contributed by unsteady flows at different airfoil locations (see Figure 5.26). However, for turbulent flow over a symmetric airfoil at zero incident angle the noise generation was found to be different. We repeat the computation with an angle of attack zero degree instead of five degrees and still keep the same Reynolds number. The sound pressure field is plotted in a square domain of five chord lengths, see Figure 5.31. The sound waves propagate radially away from the airfoil and the wave patterns are seen to be symmetric. The FFT analysis proved that there is only one tonal noise observed from the sound spectrum. In Figure 5.32, the dashed line indicates the scaled lift spectrum and the line with square markers was obtained from the experimental data of Brooks et al. [125]. There is a coincidence of vortex shedding frequency (the lift spectrum) and the acoustic tonal frequency (at 8.2 kHz). This indicates that the mechanism of sound generation in this case is purely due to the vortex shedding and there is no other source which contributes to noise generation. The solution was also compared with experimental data (in ref. [125], Figure 71(b)) with similar conditions (Re = 96000) as our numerical simulation. By comparing the two sound spectra in Figure 5.32, it is seen that there is a general agreement of the peak frequencies. The predicted tonal noise has a very narrow frequency band width and the experimental data covered a wider frequency range. The turbulent inflow is known to be able to generate broad band noise which might be the reason that the experimental data has a wider band width. Such

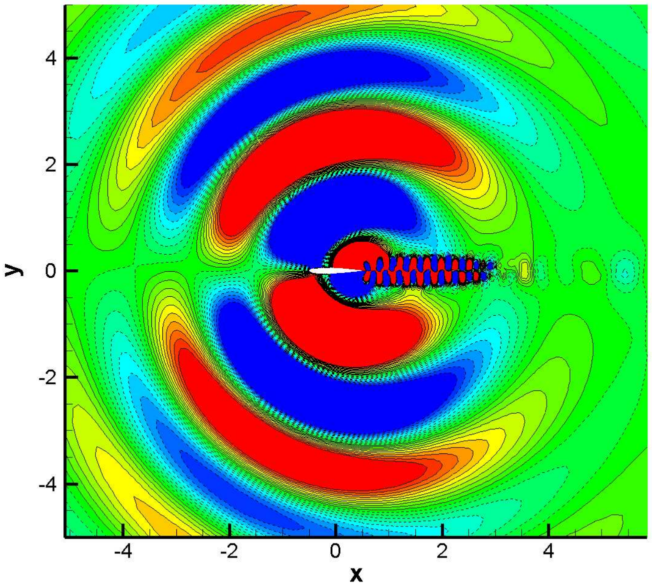

Figure 5.31: Acoustic pressure field ($\alpha = 0^0$).

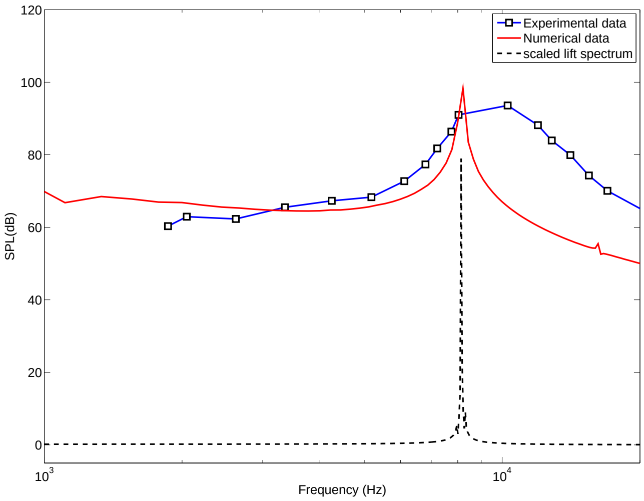

Figure 5.32: Comparison of acoustic spectra to lift spectrum ($\alpha = 0^0$).

kind of tonal noise was reported by Brooks et al. [125] which was named as laminar boundary layer vortex shedding (LBLVS) noise. The tonal noise was discovered for a untripped (smooth) airfoil as shown in reference [125], Figure 71. However, the sound spectrum was found broadband for a tripped (with a strip at 30% chord) airfoil seen in Figure 38, reference [125]. The numerical and experimental studies indicate that sound generation is very sensitive to the flow field. There might be significant changes of sound field even by changing a little of the attack angle or the surface roughness.

Chapter 6

3D flow and acoustic analysis

In this chapter, three-dimensional flow and acoustic simulations are carried out for three cases. The first simulation is the low Reynolds number flow around circular cylinder. The second case studies the turbulent airfoil flow at Reynolds number of 10^5 using LES. Finally, flow and acoustic analysis were performed for a large wind turbine using RANS.

6.1 Low Reynolds number cylinder flow

Simulation of a three-dimensional cylinder will be considered as a check of the three-dimensional code for flow and acoustics. At a Reynolds number of 200, there should be no three-dimensional effect or their effect would be extremely weak. If the flow appears only two-dimensional we can expect that the acoustic solution is also two-dimensional.

The cylinder diameter is $D = 1$ and the length of the cylinder is $L = 5D$. The computational domain extends radially outwards and the outer boundary is bounded at $r = 50$. The total number of grid point is about 0.88 million with 192 points in the circumferential direction, 96 points in the radial direction and 48 points in the spanwise direction. The flow Mach number of is 0.2. The periodic boundary conditions is set in the spanwise direction. Dimensionless time step of 0.001 is used for the acoustic simulation. In order to make the computation more efficient, the flow simulation was carried out without the acoustic part until flow is stabilized. Flow and acoustic computation were then restarted based on the stabilized flow solution till dimensionless time of about 30. The iso-surface plot of acoustic pressure is shown in Figure 6.1. The sound sources are generated from the top and bottom side of the cylinder surface and they are opposite in phase. More importantly, the sound waves are in fact purely two-dimensional as can be seen in Figure 6.1 that it is constant along the spanwise direction. The acoustic signals of two- and three-dimensional simulations are compared and

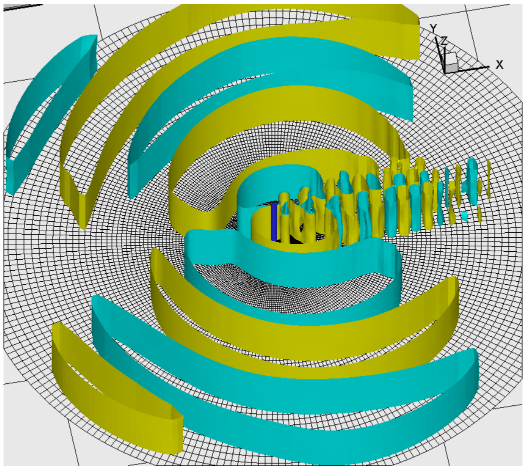

Figure 6.1: Iso-surface plot of acoustic pressure distribution from a 3D circular cylinder at Re=200, M=0.2.

results are shown in Figure 6.2. In the ideal case we should see that the two acoustic signals fit together since the third velocity component (in spanwise direction) of flow and acoustic are expected to be zero. This is almost true as demonstrated in Figure 6.2 where the difference is quite small. Our experience is that at Reynolds number up to a few thousands even though flow is fully three-dimensional the acoustic solution still has two-dimensional behavior. However, in the next simulation we shall see that for the turbulent case, the acoustic field is strongly affected in the spanwise direction.

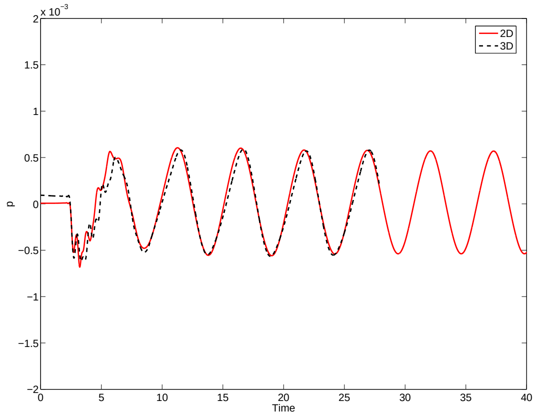

Figure 6.2: Comparison of the acoustic pressure signals for 2D and 3D case flows past a circular cylinder at Re = 200, M = 0.2.

6.2 High Reynolds number airfoil flow

In this case, flow past a NACA 0012 airfoil at a Reynolds number of 10^5 is considered. The angle of attack is set at 5^0 and flow Mach number is 0.2. The total number of grid points is 2.6 million and the O-type domain is divided into 24 blocks. There are 192 points in the circumferential direction, 96 points in the radial direction and 48 points in the spanwise direction. The size of the smallest grid near the wall surface is about 10^{-4} of the airfoil chord. The dimensionless time step for acoustic simulation is set to be 10^{-4} which corresponds to a CFL number of one. The trend is that as the Reynolds number goes higher, the grid size needs to be smaller therefore the time step for acoustic simulation is more restricted. Since the number of grids are also increased, the computational cost becomes much higher. The present flow and acoustic simulation took about one and half months with 24 processors at 2.4GHz and the CPU efficiency is around 85%.

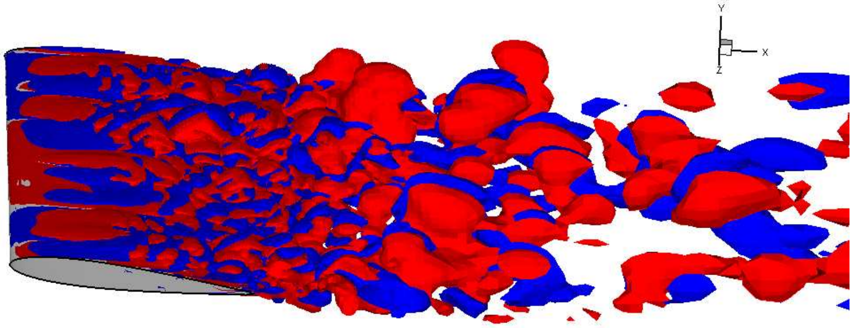

Figure 6.3: Iso-surface plot of streamwise vorticity Ω_x for flow past a NACA 0012 airfoil at Re=100 000, M=0.2 and $\alpha = 5^0$.

Flow simulation was first run until dimensionless time about 45. The three-dimensional NS equations were solved together with LES turbulence model. The eddy viscosity ν_t is determined by the mixed turbulent model developed by Ta Phuoc [120]

$$\nu_t = C \mid \overline{\vec{\omega}} \mid^{\alpha} k^{(1-\alpha)/2} \Delta^{(1+\alpha)}. \tag{6.1}$$

In Equation (6.1), C is a constant which is set to 0.02 in the present numerical study, $\vec{\omega}$ is the curl of velocity (i.e. the vorticity), k is the turbulent kinetic energy, Δ is the grid size and α is a free parameter taken a value in the range between 0 and 1. The mixed model of Ta Phuoc [120] reduces to the vorticity model in the case when $\alpha = 1$ and becomes the Bardina model [121] as $\alpha = 0$. In the present study, $\alpha = 0.5$ is used which was also proved to be an optimum value [120, 122]. The resulted vorticity iso-surface plot is shown in Figure 6.3. The small turbulence scales are seen on the airfoil surface and the eddy size becomes larger in the wake which is affected by the coarser mesh. These small eddies are never seen by two-dimensional simulations for lack of mixing of positive and negative vorticies. The mean lift coefficient is found to be $C_l = 0.586$ and the two-dimensional computation gives over predicted result of $C_l = 0.608$. As shown in Figure 6.4, the computed C_l value is very close to the experimental data by Sheldahl and Klimas [123]. Validations of the present turbulence model were performed by Shen and Sørensen [124]. By comparing the calculated lift and drag coefficients to the experiment data, good agreement was obtained for angle of attacks b

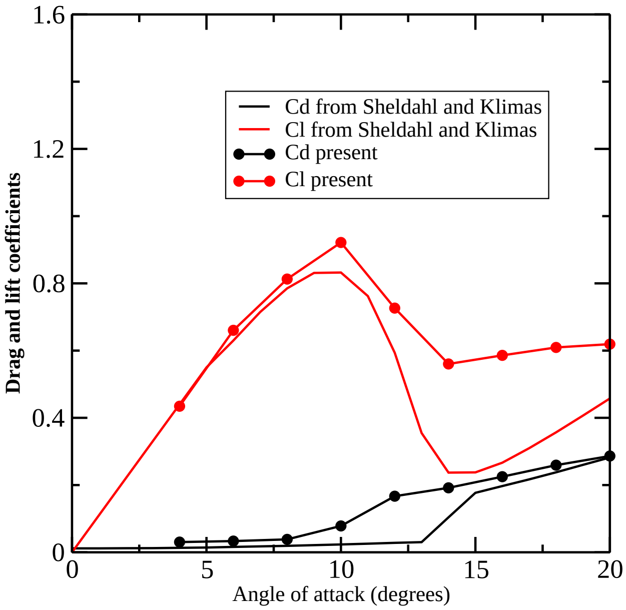

Figure 6.4: Comparison of lift and drag coefficients to the data from Sheldahl and Klimas [123].

The acoustic pressure field is shown in Figure 6.5 at dimensionless time about 10. The propagation is still in the radial direction and the phases of the waves are opposite on the pressure and suction sides of the airfoil. The

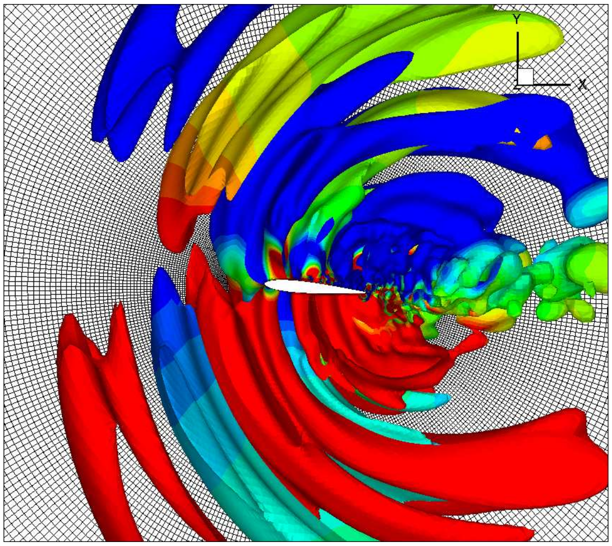

Figure 6.5: Iso-surface plot of acoustic pressure distribution from a NACA 0012 airfoil at Re=100 000, M=0.2 and $\alpha = 5^0$.

three-dimensional calculation shows that the acoustic waves are more irregular. This is because that the turbulent eddies on the airfoil have different size and strength which are all contributed as noise sources. All the small noise sources contribute to the overall noise generation from the airfoil and the dominant sources are located near the trailing edge where the strength of the vortices are known to be stronger.

In Figure 6.6, a comparison of acoustic spectrum against measurements is also performed. The simulation was carried out in a dimensionless form with unit inlet velocity and unit chord length. The present numerical result needs to be re-scaled to dimensional data. For a given Mach number 0.2 and sound speed 340 m/s, we obtain the free stream velocity of $U_\infty = 68$ m/s. The real chord length is therefore calculated as $Chord = Re \cdot \nu / U_\infty = 2.2$ cm. Experiments for noise generation from low Reynolds number flow is very difficult and experiments done by Brooks et al. [125] provided us an opportunity to make a comparison at the modest Reynolds number around 10^5. The experimental noise spectrum was obtained for flow past a NACA 0012 airfoil with chord length of 2.54 cm and an angle of attack of 4.8^0 at the observer positioned perpendicular to, and 1.22 m from the trailing edge. The receiver point of the present numerical simulation was also positioned perpendicular to the trailing edge but only two chord length away from the trailing edge. In practice, the numerical test point can be selected at the same position as used in the experiment which is around 48 chord length away from trailing

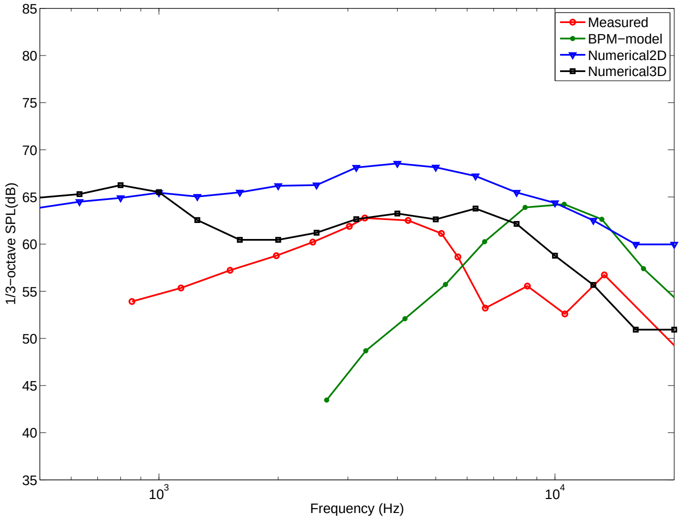

Figure 6.6: Comparison of acoustic sprectra in 1/3-octave band. The measurement data is obtained from ref. [125].

edge. Our computational domain in the present case is only 20 chord lengths and to increase the size of domain will make the mesh even coarser. Therefore, the acoustic signal was recorded at the position of two chord lengths with a large grid density. Assuming a cylindrical propagation the correction to the recorded acoustic signal is $10\log(1/48) - 10\log(1/2) = -13.8$ dB. In Figure 6.6 four spectra were compared in the 1/3-octave band (see Table 6.1 for the center frequencies): the experimental data, the data from semi-empirical model [125], two- and three-dimensional numerical simulations. The narrow band numerical data were averaged in 1/3-octave band to follow the same format as experiment data. Neither the semi-empirical data nor the numerical data fit well with the experimental data. The numerical simulations over predicted the sound pressure level especially for the two-dimensional calculation. The three-dimensional simulation seems to be closer to the experimental data except at the lower frequency range where predicted value is apparently higher. However, it is never easy to make such

20 25 **31.5** 40 50 **63** 80 100 **125** 160 200 **250** 315 400 **500** 630 800 **1000**
1250 1600 **2000** 2500 3150 **4000** 5000 6300 **8000** 10000 12500 **16000** 20000

Table 6.1: Standard octave (bold numbers) and 1/3-octave band center frequencies (in hertz).

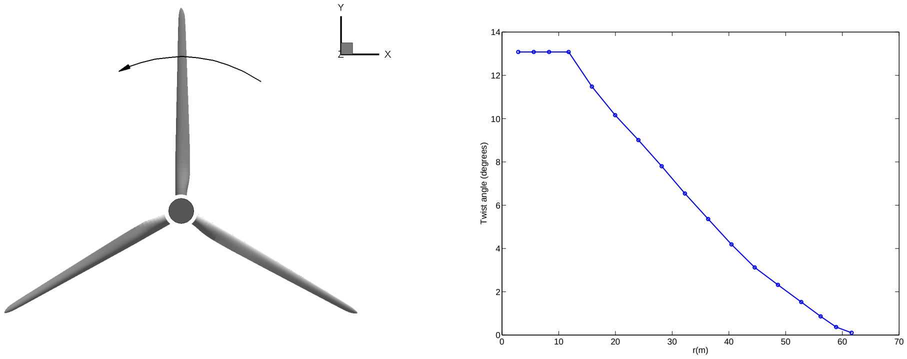

Figure 6.7: Rotor description of the NREL5MW virtual wind turbine.

comparisons since there are several issues that affect results from experiment and numerical simulations. For example, the smoothness of the airfoil makes sense for stability and transition therefore the generation of sound will be different. This phenomena was reported by Nash et al. [126] where they repeated a same set of experiment for a smooth and a further smoothed NACA airfoil. The smoother airfoil showed tonal acoustic response over a wide range of speeds and angles of attack. For the numerical simulations, a uniform inflow condition was applied at the inlet of computational boundary which is not the same case for wind tunnel measurement. Also only limited number of grid points are employed for numerical computation and the grid dependency study is expensive.

6.3 Flow over a wind turbine blade

In this section the numerical simulation is continued for a large wind turbine blade. The wind turbine was designed by the National Renewable Energy Laboratory (NREL) as a test wind turbine. The wind turbine is three bladed and supposed to be rated at 5 MW or higher. Each blade is 63 m long and with a quite smooth twist distribution, see Figure 6.7.

The configuration of the computational mesh is shown in Figure 6.8. The blade surface mesh was generated by Matlab together with Gridgen. The surface mesh was made very orthogonal since it will influence the overall mesh quality. The in-house hyperbolic mesh generation code was applied to create the body-fitted structured grid. The mesh was created for one blade and assuming periodic boundary condition at the two azimuthal surfaces. The wind goes through z-direction and the blades rotate in clockwise direction seen from the upwind direction. The total number of grid points is

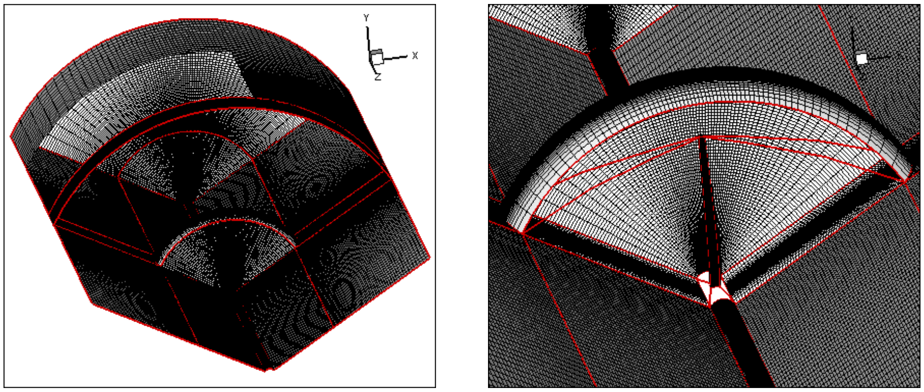

Figure 6.8: Mesh configuration of the NREL5MW virtual wind turbine.

2.62 million and the domain was divided into 10 blocks each consists 64^3 grid points. The domain consists two parts: the inner part with 5 blocks surrounding the blade and the outer part with another 5 blocks surrounding the inner part. In Appendix C, more details of the grid generation for a wind turbine blade are given.

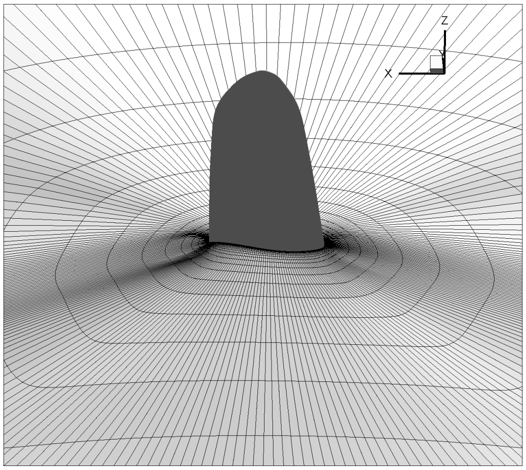

Figure 6.9: A slice of mesh near tip region.

In the present simulation, the inlet wind speed is at 10 m/s and rotor speed is at 12.1 rpm. The corresponding maximum Reynolds number based on chord is between 7 and 8 million. The flow simulation was carried out with EllipSys3D. The conventional RANS turbulence model was utilized since LES turbulence model for such a high Reynolds number becomes too

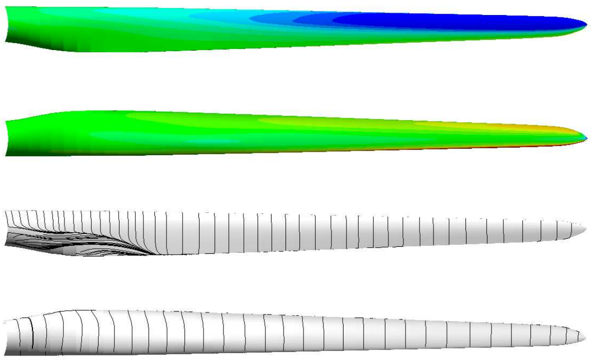

Figure 6.10: Surface pressure and streamlines on suction side and pressure side.

expensive. The plots of surface pressure and streamlines on the suction and pressure sides are shown in Figure 6.10. It is as usual that negative and positive pressures are distributed on the suction and pressure sides of the airfoil, respectively. Also the streamlines are fully attached on the pressure side as expected. On the suction side, the streamlines indicate that the flow is well attached in the outer part of the blade close to the tip. The incompressible pressure is shown together with streamlines at three spanwise blade stations: r = 15 m, 35 m and 55 m, see Figure 6.11 on the left column. Separation is seen in the inner part of the blade, e.g. at r = 15 m the flow is separated near trailing edge. At r = 15 m, DU35 airfoil is used and NACA64 airfoil profile is used at r = 35 m and 55 m. The pressure coefficients at the same spanwise blade locations were computed by both steady and unsteady computations. The pressure coefficients were found by the following definition

$$C_p = \frac{P - P_\infty}{\frac{1}{2}\rho_\infty \left[W_\infty^2 + (\Omega r)^2\right]} \tag{6.2}$$

where $W_\infty = 10$ m/s is the inlet wind velocity. Difference by using steady and unsteady computations was mainly found at the suction side of the blade inner part. The agreement of C_p curve is better at the outer parts of the blade. At the inner parts of the blade, angles of incidence are usually large and due to the neglect of transition from laminar to turbulent flow, the predicted pressure coefficient must be influenced for both steady and unsteady computations.

The unsteady flow computation was first carried out as a preparation for acoustic simulation. The flow was simulated for 40 000 iterations with a

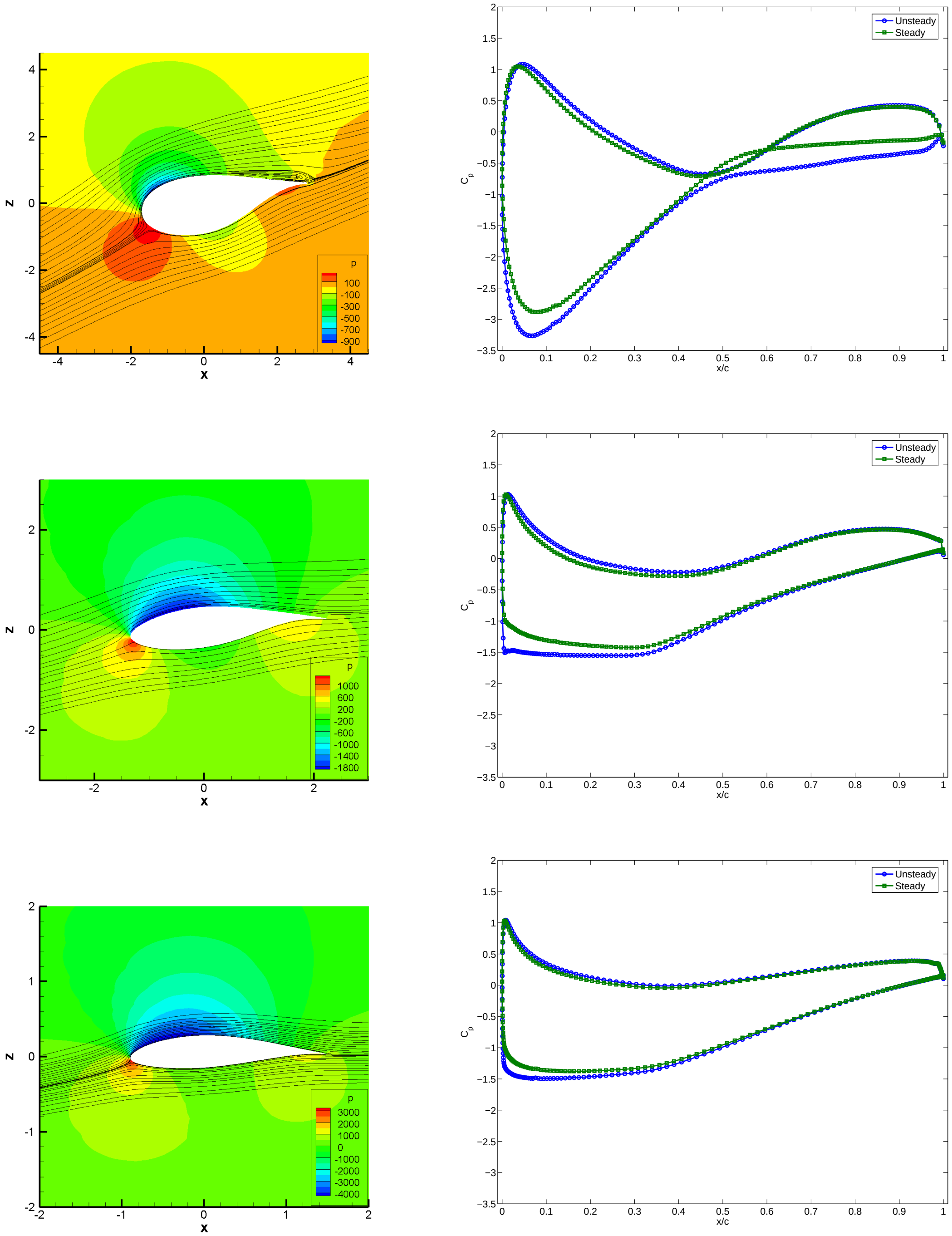

Figure 6.11: Left column: pressure contour and streamlines at 15 m, 35 m and 55 m blade positions; right column: the corresponding pressure coefficients obtained by steady and unsteady computations.

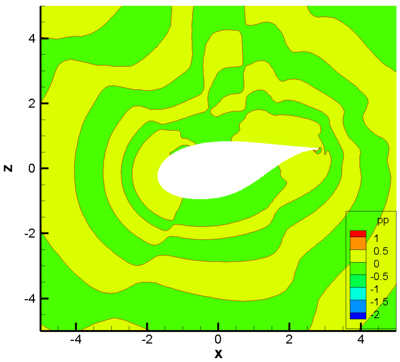

Figure 6.12: r = 15m.

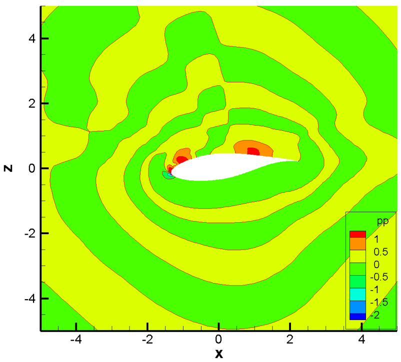

Figure 6.13: r = 35m.

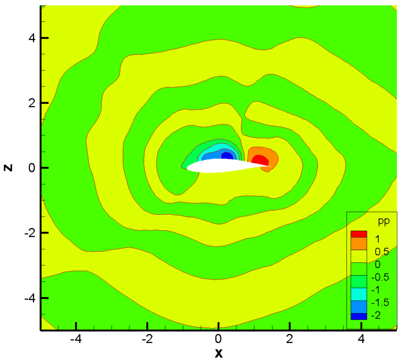

Figure 6.14: r = 55m.

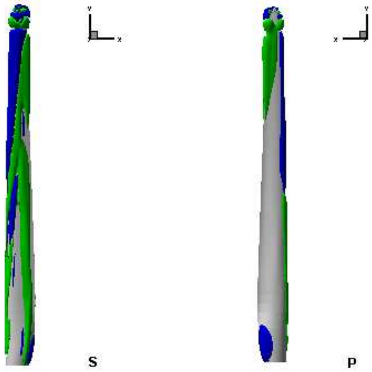

Figure 6.15: Sound sources on blade.

time step 0.0001 second which corresponds to two blade revolutions. The air density and dynamic viscosity is set at 1.225 $kg \cdot m^{-3}$ and 1.788 $kg \cdot m^{-1} \cdot s^{-1}$, respectively. The flow Mach number is about 0.03 based on the free stream velocity of 10 m/s and a sound speed of 340 m/s. Assuming the specific heat ratio is $\gamma = 1.4$, the ambient pressure is computed at $P_0 = c_0^2 \rho / \gamma = 1.01 \times 10^5$ Pa. The time step for acoustic simulation is very small, in this case $\Delta t = 10^{-6}$ second is used since the sound speed is more than 30 times faster than the free stream velocity. The acoustic computation was performed for a time period of 0.2 seconds with the number of iterations about 200 000. Although time period is relatively short, the computation is still very expensive in terms of computational time.

In Figure 6.12, 6.13 and 6.14 the sound pressure contours were shown at different spanwise stations: r = 15 m, 35 m and 55 m, respectively. The maximum sound pressure is around 1 Pa corresponds to sound pressure level at 94 dB. It is seen that the sound pressure increases from the root of the

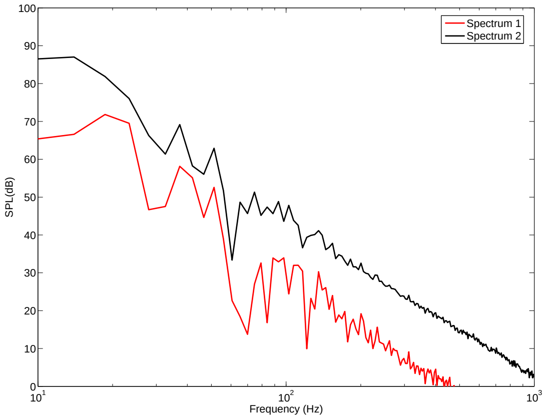

Figure 6.16: Plot of sound pressure level at two test points.

blade towards the tip. Also it may be noticed that the sound sources moved towards the leading edge from r = 55 m to r = 35 m as the angle of attack also increased. Figure 6.15 also shows the location of the sound sources on the suction and pressure surfaces of the blade. The sources are basically seen on the suction side where flow is generally more unstable than the pressure side, this indicates that the sound generation has strong dependency on flow unsteadiness.

The sound spectra is shown in Figure 6.16 where spectrum 1 was recorded at 1 m way just on top of the blade tip and spectrum 2 was recorded at the station of r = 60 m and 1m away from the trailing edge in the direction normal to the suction surface. The test points are selected very close to the blade since the mesh becomes too coarse at further positions which will introduce much larger dissipation and dispersion errors. An example of the mesh can be seen from Figure 6.9. The overall noise level is 84 dB for spectrum 1 and 96 dB for spectrum 2. It can be seen from the plot that the high frequencies were not well represented. This is basically due to two reasons: the use of RANS turbulence model and the low grid density. For solving wind turbine flow problems, a RANS model is the most popular one to low cost and good performance in practice. For solving acoustic problems, we might first consider DNS method which resolves all small turbulence structures without any modeling. However, this method is not considered for wind turbine cases due to the huge amount of computational cost. Following the suggestion of Piomelli and Balaras [127], the typical number of grid points for solving a three dimensional flow is in the order of $Re^{9/4}$. Therefore the total number of grid points for the present blade would be around 10^{15}.

The next possibility is to use a LES model which has lower cost than a DNS method and is able to model small turbulent structures to a certain level. The question is that for Reynolds number higher than 100 millon, the LES model is not very suitable. On the other hand, a high number of grid points is also demanded. An example was shown by Arakawa et al. [35] where they carried out LES simulation for a small wind turbine blade. The Reynolds number based on chord was 1 million. The simulation was performed by using up to 320 million grid points on 112 processors. The time step was restricted at 1.4×10^{-7} seconds and the simulation was performed only for a time period of 50 millisecond with the blade rotation of 20.4 degrees and the tip movement of 2.6 m. It is seen that the time period is possibly too short to obtain a reliable sound spectrum. Also the computation is still too heavy for such a small wind turbine. Our present simulation is considered as a trade off which shows the possibility to predict wind turbine noise. The use of a RANS model has an evident drawback to smooth out small turbulence structures. This leads to the acoustic solution which is absent of high frequency components, as shown in Figure 6.16. The day of using DNS will eventually arrive, consider the yearly increment of computer power, it will still take more than 20 years to make such computation to the real stage. While waiting, our work of simulating wind turbine noise will go on and the idea is to apply accurate method with low computational cost. Using a different mesh for acoustic computation could be a good strategy where time step will not be restricted by small grid size on the wall surface. This yields the further development of our in-house EllipSys3D code with a grid over-lapping method. Another issue is the choice of turbulence model, an hybrid turbulence model might be a better choice such as the DES model (the mixing of RANS and LES models).

Chapter 7

Closure and Outlook

This chapter summarizes methods and results shown in previous chapters and presents an outlook for future work.

High-order finite difference aeroacoustic code based on the incompressible/acoustic splitting method has been implemented into the in-house incompressible Navier-Stokes flow solver. The incompressible flow equations and the acoustic equations are solved at the same time levels where the pressure and the velocities obtained from the incompressible equations form the input to the acoustic equations at each time step.

The development of high-order schemes for solving CAA problems has been studied in details. A series of optimized explicit and implicit finite difference schemes were derived using the DRP (Dispersion-Relation-Preserving) strategy. It was found that the optimized schemes are more suitable for solving acoustic equations since they keep lower dispersion errors at higher frequency region than the traditional schemes. Study of numerical schemes was also extended to the non-centered boundary stencils and the high-order explicit/implicit filters. The use of acoustic radiation and outflow boundary conditions together with non-centered schemes has shown good performance.

Numerical results have been first presented for two test cases: the acoustic wave scattering from a circular cylinder and sound generation due to a spinning vortex pair. The numerical solutions were validated with analytical data and good agreement was obtained. To understand the mechanisms of flow generated sound, two dimensional aeroacoustic simulations of flow past a stationary circular cylinder and an oscillating circular cylinder was carried out and we focused in details. For flow over a stationary cylinder, it was found that the sound frequency was dominated by the Strouhal frequency which is the frequency of fluctuating lift force whereas the drag produces little noise. For flow over an oscillating cylinder, the sound frequency was dominated by the frequency from external force and also there are more contributions from the drag force which is not negligible for sound generation. Further numerical study was focused on airfoil flow and noise simulation in two- and three-dimensions. For turbulent cases, the use of a LES model provided reasonable good results where high-frequency components on the sound spectra were resolved. The general trend was found that it was still the unsteady lift force that is responsible for sound generation. The sound directivity patterns showed the same property for both cylinder and airfoil. The last attempt was made for CAA simulation of a large wind turbine. The results showed some general properties of sound generation from a wind turbine blade where the blade tip is the most noisy region. Due to a limited number of grid points and the use of a RANS turbulence model, the solution was limited in the low frequency range.

In the future, further improvement of the EllipSys3D code will be carried out. The use of a high-order grid over-lapping technique for coupling in CFD/CAA is seen to be very necessary. In such a way, the acoustic mesh can be constructed in different way such as a simple cartesian mesh. The advantage is to use much larger time step for acoustic simulation, also high-order finite difference schemes often require high quality of computational mesh. The choice of turbulence model is another issue to be discussed in the future. The hope is to apply LES model for wind turbine simulation in the inner part where sound sources are located.

Appendix A

Coefficient matrices of acoustic equations

The acoustic equations in 3D matrix form are written as:

$$\frac{\partial Q}{\partial t} + \frac{\partial E}{\partial x} + \frac{\partial F}{\partial y} + \frac{\partial G}{\partial z} = S \tag{A.1}$$

where matrices Q, E, F, G and S are

$$Q = \begin{pmatrix} \rho' \\ \rho u' + \rho' U \\ \rho v' + \rho' V \\ \rho w' + \rho' W \\ p' \end{pmatrix}, E = \begin{pmatrix} \rho u' + \rho' U \\ \rho(2Uu' + {u'}^2) + \rho' U^2 + p' \\ \rho(Vu' + Uv' + u'v') + \rho' UV \\ \rho(Wu' + Uw' + u'w') + \rho' UW \\ c^2(\rho u' + \rho' U) \end{pmatrix},$$

$$F = \begin{pmatrix} \rho v' + \rho' V \\ \rho(Vu' + Uv' + u'v') + \rho' UV \\ \rho(2Vv' + {v'}^2) + \rho' V^2 + p' \\ \rho(Vw' + Wv' + v'w') + \rho' VW \\ c^2(\rho v' + \rho' V) \end{pmatrix},$$

$$G = \begin{pmatrix} \rho w' + \rho' W \\ \rho(Wu' + Uw' + u'w') + \rho' UW \\ \rho(Wv' + Vw' + v'w') + \rho' VW \\ \rho(2Ww' + {w'}^2) + \rho' W^2 + p' \\ c^2(\rho w' + \rho' W) \end{pmatrix}, S = \begin{pmatrix} 0 \\ 0 \\ 0 \\ 0 \\ -\frac{\partial P}{\partial t} \end{pmatrix}. \tag{A.2}$$

Equation A.1 is identical to the following equation

$$\hat{C}\frac{\partial \hat{Q}}{\partial t} + \hat{A}\frac{\partial \hat{Q}}{\partial x} + \hat{B}\frac{\partial \hat{Q}}{\partial y} + \hat{D}\frac{\partial \hat{Q}}{\partial z} = S \tag{A.3}$$

with the condition that $\hat{C} = \partial Q/\partial \hat{Q}$. Defining the new vector $\hat{Q} = (\rho', u', v', w', p')^T$, the coefficient matrix $\hat{C}, \hat{A}, \hat{B}, \hat{D}$ are determined as

$$\hat{C} = \begin{pmatrix} 1 & 0 & 0 & 0 & 0 \\ U & \rho & 0 & 0 & 0 \\ V & 0 & \rho & 0 & 0 \\ W & 0 & 0 & \rho & 0 \\ 0 & 0 & 0 & 0 & 1 \end{pmatrix}, \hat{A} = \begin{pmatrix} U & \rho & 0 & 0 & 0 \\ U^2 & 2\rho U & 0 & 0 & 1 \\ UV & \rho V & \rho U & 0 & 0 \\ UW & \rho W & 0 & \rho U & 0 \\ c^2 U & c^2 \rho & 0 & 0 & 0 \end{pmatrix},$$

$$\hat{B} = \begin{pmatrix} V & 0 & \rho & 0 & 0 \\ UV & \rho V & 0 & 0 & 0 \\ V^2 & 0 & 2\rho V & 0 & 1 \\ VW & 0 & \rho W & \rho V & 0 \\ c^2 V & 0 & c^2 \rho & 0 & 0 \end{pmatrix}, \hat{D} = \begin{pmatrix} W & 0 & 0 & \rho & 0 \\ UW & \rho W & 0 & \rho U & 0 \\ VW & 0 & \rho W & \rho V & 0 \\ W^2 & 0 & 0 & 2\rho W & 1 \\ c^2 W & 0 & 0 & c^2 \rho & 0 \end{pmatrix} \tag{A.4}$$

Dividing matrix $\hat{C}$ at both sides of Equation A.3 yields

$$\frac{\partial \hat{Q}}{\partial t} + \bar{A}\frac{\partial \hat{Q}}{\partial x} + \bar{B}\frac{\partial \hat{Q}}{\partial y} + \bar{D}\frac{\partial \hat{Q}}{\partial z} = \hat{S} \tag{A.5}$$

where new coefficients $\bar{A}, \bar{B}$ and $\bar{D}$ are computed and the source term turns out to be the same

$$\bar{A} = \begin{pmatrix} U & \rho & 0 & 0 & 0 \\ 0 & U & 0 & 0 & 1/\rho \\ 0 & v' & U & 0 & 0 \\ 0 & w' & 0 & U & 0 \\ c^2 U & c^2 \rho & 0 & 0 & 0 \end{pmatrix}, \bar{B} = \begin{pmatrix} V & 0 & \rho & 0 & 0 \\ 0 & V & u' & 0 & 0 \\ 0 & 0 & V & 0 & 1/\rho \\ 0 & 0 & w' & V & 0 \\ c^2 V & 0 & c^2 \rho & 0 & 0 \end{pmatrix},$$

$$\bar{D} = \begin{pmatrix} W & 0 & 0 & \rho & 0 \\ 0 & W & 0 & u' & 0 \\ 0 & 0 & W & v' & 0 \\ 0 & 0 & 0 & W & 1/\rho \\ c^2 W & 0 & 0 & c^2 \rho & 0 \end{pmatrix}, \hat{S} = \begin{pmatrix} 0 \\ 0 \\ 0 \\ 0 \\ -\partial P/\partial t \end{pmatrix} \tag{A.6}$$

Appendix B

Coefficients of the high-order schemes

Coefficients for DRP and compact schemes

Consider spatial derivative $\partial f/\partial x$, the derivative can be approximated by central explicit 2N+1 point stencil finite difference scheme, such as

$$\frac{\partial f}{\partial x}(x_0) = \frac{1}{\Delta x}\sum_{j=-N}^{N} a_j f(x_0 + j\Delta x) \tag{B.1}$$

Table B.1 gives the coefficients for a_j.

To approximate $\partial f/\partial x$, compact finite difference schemes can be used alternatively. Using f' instead of $\partial f/\partial x$, the scheme reads

$$\begin{aligned} \alpha f'_{j-1} + f'_j + \alpha f'_{j+1} &= a\frac{f_{i+1} - f_{i-1}}{\Delta x} + b\frac{f_{i+2} - f_{i-2}}{\Delta x} + c\frac{f_{i+3} - f_{i-3}}{\Delta x} \\ &\quad + d\frac{f_{i+4} - f_{i-4}}{\Delta x} + e\frac{f_{i+5} - f_{i-5}}{\Delta x} \end{aligned} \tag{B.2}$$

Table B.2 gives coefficients for standard tridiagonal high-order compact finite difference schemes. Coefficients for the optimized compact finite difference schemes are shown in Table B.3.

	4th-order	**6th-order**	**8th-order**
a_1	0.7992664269741557	0.8331572598964366	0.8571043984185199
a_2	-0.1894131415793246	-0.2331572598964366	-0.2652621696211656
a_3	0.0265199520614978	0.0523054923365680	0.0748052085071437
a_4	0	-0.0059398042783169	-0.0144484568416228
a_5	0	0	0.0013596285337742
a_6	0	0	0
a_7	0	0	0
a_8	0	0	0
	10th-order	**12th-order**	**14th-order**
a_1	0.8749994731879014	0.8888984093343903	0.9000111291581978
a_2	-0.2901779129134481	-0.3101978791125205	-0.3266822474881437
a_3	0.0942455927359495	0.1111206315566125	0.1258713338034306
a_4	-0.0238093482054909	-0.0332537742227347	-0.0424313246158228
a_5	0.0039501765402089	0.0074088498991500	0.0114246353417500
a_6	-0.0003156525746558	-0.0010686423745439	-0.0022540026898321
a_7	0	0.0000740222661807	0.0002864892431738
a_8	0	0	-0.0000174903001106

Table B.1: Coefficients for high-order optimized finite difference schemes. $a_j = -a_{-j}$. Stencil width: 7-point(4th-order) up to 17-point(14th-order).

	4th-order	**6th-order**	**8th-order**	**10th-order**	**12th-order**
α	1/4	1/3	3/8	2/5	5/12
a	3/4	7/9	25/32	39/50	7/9
b	0	1/36	1/20	1/15	5/63
c	0	0	-1/480	-1/210	-5/672
d	0	0	0	1/4200	1/1512
e	0	0	0	0	-1/30240

Table B.2: Coefficients for original tridiagonal high-order compact finite difference schemes. Stencil width on the right hand side: 3-point(4th-order) up to 11-point(12th-order).

Coefficients for boundary schemes

Consider non-centered DRP schemes as

$$\frac{\partial f}{\partial x}(x_0) = \frac{1}{\Delta x} \sum_{j=-N}^{M} a_j f(x_0 + j\Delta x) \tag{B.3}$$

	4th-order	**6th-order**
α	0.3821038098462933	0.4111403764203249
a	0.7940346032820977	0.7842616980350271
b	0.0440346032820977	0.0692748674241733
c	0	-0.0038903521543495
d	0	0
e	0	0
	8th-order	**10th-order**
α	0.4278627893013504	0.4388871532438393
a	0.7786068605349324	0.7748150462341548
b	0.0852418595342336	0.0962949739000680
c	-0.0077472036156208	-0.0110116258189503
d	0.0005034551362033	0.0012257054792086
e	0	-0.0000771570500869

Table B.3: Coefficients for optimized tridiagonal high-order compact finite difference schemes. Stencil width on right hand side: 5-point(4th-order) up to 11-point(10th-order).

where $M \neq N$. An example of the backward stencil coefficients a_j^{MN} proposed by Tam is listed in Table B.4.

a_j^{NM}	N = 0, M = 6	a_j^{NM}	N = 1, M = 5	a_j^{NM}	N = 2, M = 4
a_0^{06}	-2.192280339	a_{-1}^{15}	-0.209337622	a_{-2}^{24}	0.049041958
a_1^{06}	4.748611401	a_0^{15}	-1.084875676	a_{-1}^{24}	-0.468840357
a_2^{06}	-5.108851915	a_1^{15}	2.147776050	a_0^{24}	-0.474760914
a_3^{06}	4.461567104	a_2^{15}	-1.388928322	a_1^{24}	1.273274737
a_4^{06}	-2.833498741	a_3^{15}	0.768949766	a_2^{24}	-0.518484526
a_5^{06}	1.128328861	a_4^{15}	-0.281814650	a_3^{24}	0.166138533
a_6^{06}	-0.203876371	a_5^{15}	0.048230454	a_4^{24}	-0.026369431

Table B.4: Coefficients of explicit backward schemes for boundary closures. $a_j^{NM} = -a_{-j}^{MN}$. N is the number of points to the left and M is the number of points to the right.

An example of a sixth-order compact scheme, a set of stable boundary scheme is written as

$$6f_1' + 18f_2' = \frac{1}{\Delta x}(-17f_1 + 9f_2 + 9f_3 - f_4) \qquad \text{fourth-order at } j = 1$$
$$3f_1' + 18f_2' + 9f_3' = \frac{1}{\Delta x}(-10f_1 - 9f_2 + 18f_3 + f_4) \qquad \text{fifth-order at } j = 2$$

More combinations of compact boundary schemes are referred to Carpenter et al. [59] where they performed stability analysis for difference boundary schemes.

Coefficients of filter schemes

The explicit type selective filter with $2N+1$ point stencil reads

$$\tilde{f}(x_0) = f(x_0) - \delta_d D_u(x_0) \tag{B.4}$$

where $\tilde{f}$ is the filtered value, δ_d is the damping coefficient from 0 to 1 and the term $D_u(x_0)$ is given as

$$D_u(x_0) = \sum_{j=-N}^{j=N} d_j f(x_0 + j\Delta x) \tag{B.5}$$

The coefficients d_j for standard and optimized filters are listed in Table B.5 and B.6.

	8th-order	**10th-order**	**12th-order**
d_0	35/128	63/256	231/1024
d_1	-7/32	-105/512	-99/512
d_2	7/64	15/128	495/4096
d_3	-1/32	-45/1024	-55/1024
d_4	1/256	5/512	33/2048
d_5	0	-1/1024	-3/1024
d_6	0	0	1/4096

Table B.5: Coefficients for standard high-order explicit filters. $d_j = d_{-j}$. Stencil width: 9-point(8th-order) up to 13-point(12th-order). [50]

Instead of using explicit high-order filters, the compact high-order filtering schemes can be used also. The compact filter form is written as

$$\alpha_f \tilde{f}_{j-1} + \tilde{f}_j + \alpha_f \tilde{f}_{j+1} = \sum_{n=0}^{N} \frac{a_n}{2}(f_{j+n} + f_{j-n}) \tag{B.6}$$

where $\tilde{f}$ is the value after filtering, α_f is the free parameter and a_n are the coefficients which are listed in Table B.7.

	6th-order	**8th-order**	**10th-order**
d_0	0.243527493120	0.215044884112	0.190899511506
d_1	-0.204788880640	-0.187772883589	-0.171503832236
d_2	0.120007591680	0.123755948787	0.123632891797
d_3	-0.045211119360	-0.059227575576	-0.069975429105
d_4	0.008228661760	0.018721609157	0.029662754736
d_5	0	-0.002999540835	-0.008520738659
d_6	0	0	0.001254597714

Table B.6: Coefficients for optimized high-order explicit filters. $d_j = d_{-j}$. Stencil width: 9-point(6th-order) up to 13-point(10th-order). [50]

	4th-order	**6th-order**	**8th-order**	**10th-order**
a_0	$\frac{5}{8}+\frac{3\alpha_f}{4}$	$\frac{11}{16}+\frac{5\alpha_f}{8}$	$\frac{93+70\alpha_f}{128}$	$\frac{193+126\alpha_f}{256}$
a_1	$\frac{1}{2}+\alpha_f$	$\frac{15}{32}+\frac{17\alpha_f}{16}$	$\frac{7+18\alpha_f}{16}$	$\frac{105+302\alpha_f}{256}$
a_2	$-\frac{1}{8}+\frac{\alpha_f}{4}$	$-\frac{3}{16}+\frac{3\alpha_f}{8}$	$\frac{-7+14\alpha_f}{32}$	$\frac{-15+30\alpha_f}{64}$
a_3	0	$\frac{1}{32}-\frac{\alpha_f}{16}$	$\frac{1-2\alpha_f}{16}$	$\frac{45-90\alpha_f}{512}$
a_4	0	0	$\frac{-1+2\alpha_f}{128}$	$\frac{-5+10\alpha_f}{256}$
a_5	0	0	0	$\frac{1-2\alpha_f}{512}$

Table B.7: Coefficients for high-order compact filters. $0 <\mid \alpha_f \mid\leq 0.5$. Stencil width on right hand side: 5-point(4th-order) up to 11-point(10th-order). [51]

Appendix C

Wind turbine mesh generation

The aim of this chapter is to illustrate some guide lines of generating structured meshes for wind turbine blades in connection of our in-house HyperMesh generator developed by Jess A. Michelsen. Three different mesh configurations will be shown by using different kind of wind turbine blades.

Case 1: Spherical-mesh of a two-blade turbine

We first consider the case of the two-blade NREL phase VI rotor. The radius of blade is about 5.3 m and the maximum twist angle is 20.4 degrees. In general, a smoothly distributed twist angle will make the mesh generation easier, and in this case the large twist angle at blade inner part will slightly increase the difficulty of generating a volume mesh. For a two-blade wind turbine, we wish to generate a mesh for one blade and apply symmetric (non-rotational case) or periodic boundary condition (rotational case) at the middle plane of the two blades. The desired mesh will be a half sphere with a radius of R = 50 m.

The present mesh generator is able to generate a mesh by self-extruding from the surface mesh (blade surface) with or without giving an outer bounded surface mesh. The first thing to do is to generate a blade surface mesh. The surface mesh for the present NREL phase VI blade is shown in Figure C.1 and C.2. There are five blocks on blade and each has number of grid points 64 × 64. The mesh is smoothly stretched towards tip where flow Reynolds number becomes higher. The tip has a nearly squared shape and there is one block representing the tip, see Figure C.2. The general requirement for surface mesh is the orthogonality. The surface mesh is saved with a name *blade.x2d* where *.x2d* is the mesh format of EllipSys2D. The next thing is to create an outer surface with the same number of blocks and grid points. The mesh is seen as the outer part (in black) of Figure C.3 where the radius of the half sphere is 50. The outer surface must be named as *blade.x2d.outer* which is written in the same format as *.x2d* file. The surface mesh must be created in the way that it obeys the right hand rule and the third dimension must be pointing outwards.

The last thing is to create the volume mesh in between the blade surface and the outer surface. Before running the hyper mesh generator a input script must be specified. The file with the name *blade.hyp* is shown below

```
0 1 0 0.d0          ! a b c d
601                 ! attrib
0.5d0               ! relax
1 0 0               ! u v w
2                   ! nb
1.d-4 50 1.025      ! dx R0 stretch
```

The input is short but it contains quite a lot of information. In order to make it easier for explanation, we listed the corresponding variable names on the right hand side of those numbers. There are four values defined in the first line which define the boundary planes: a,b,c,d. The boundary planes satisfy the condition that $ax + by + cz + d = 0$. Here we want the $y = 0$ to be the symmetric plane and this is satisfied by putting $a = 0$, $b = 1$, $c = 0$ and $d = 0$. In the second line we put the attribution of the symmetric plane which is 601 as defined in EllipSys code. The third line is the relaxation value which is between 0 and 1. The relaxation value defines the interpolation/extroplation factor which is case dependent and there is no optimum value that can be suggested here. The fourth line provides the farfield velocity components. In this case, $u = 1$ indicates the inlet wind direction is on the x-axis. Based on the information of this line, the attributions for inlet and outlet boundary conditions will be determined and finally written in the output data. The next line with $nb = 2$ allows us to generate two blocks way from the surface and the number of grid is 64 (default) for each block in the extruding direction. The last line has three numbers, the first one $dx = 1.d - 4$ defines the height of the first cell away from the blade surface. This value is chosen such that the boundary layer can be well-resolved. The next value $R0 = 50$ is active only when the outer boundary is absent (the absent of file *blade.x2d.outer*). In such a case the outer boundary will be generated automatically with the last mesh layer at approximately $R = 50$. The automatically generated outer surface is also a near sphere in the present case. Here we proved a more generalized method with a pre-specified outer geometry, so the value $R0 = 50$ is redundant in the present case. The very last value specifies the stretching rate which ensures the meshes are clustered on blade surface. This is the most sensitive value for the mesh generation. The only way is to choose it by practicing.

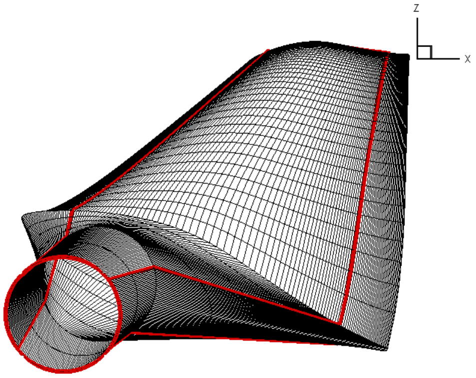

Figure C.1: Surface mesh on blade.

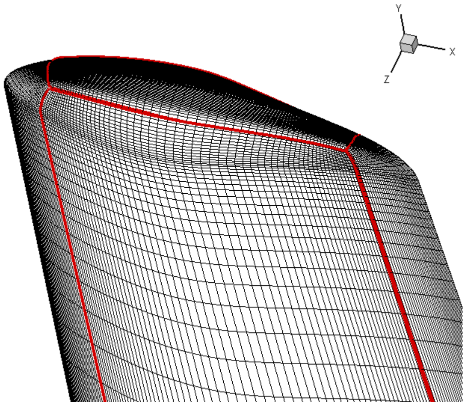

Figure C.2: Mesh on blade tip.

The mesh structure is shown in Figure C.3 and C.4. In Figure C.3, the blade is located at the center and we see that the half sphere is bounded by the symmetric plane (blue) at $y = 0$ and the in/out-flow boundary (black) at $r = 50$. Figure C.4 shows the block interfaces where the five numbers depict block numbers. The other five blocks are not visible in the plot since they are very closely attached on the blade.

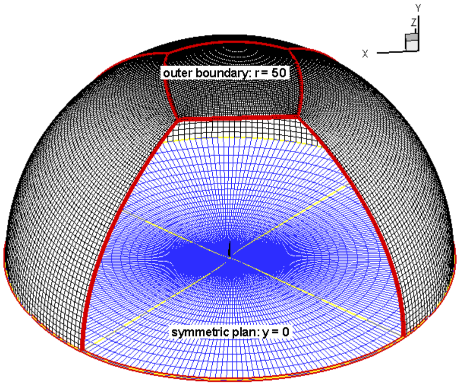

Figure C.3: Outer boundaries.

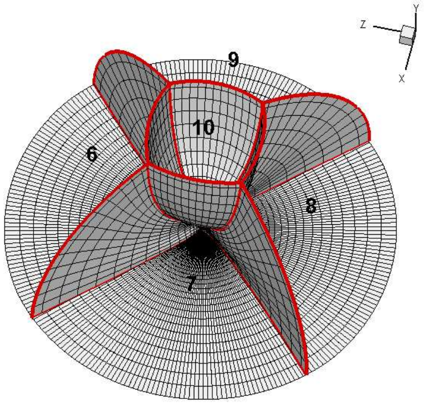

Figure C.4: Block interfaces.

Case 2: Spherical-mesh of a three-blade turbine

The second example is shown for a three-blade LM blade. The length of the blade is about 19 m and the maximum twist angle is about 13 degrees. We still choose to make a spherical mesh and only a sector of 120 degrees is considered since the turbine has three blades.

The surface mesh for this blade is shown in Figure C.5 and C.6. There are five blocks on blade surface and each block has number of grid points 64×64. The blade tip is rounded and shaper. The tip geometry is described by 64×64 grid points, see Figure C.6. The blade surface mesh is saved with a file named *blade.x2d*. In the next step we will create an intermediate outer surface. This surface mesh is shown in Figure C.7. There are five surface blocks defined for the intermediate outer surface which forms a sector of 120 degrees. They are two cyclic surfaces, the front and the back surfaces and the curved surface on top. The file name for this intermediate outer surface is *blade.x2d.outer*. The aim is to create volume mesh between the blade surface and the intermediate outer surface. The file *blade.hyp* listed below is used to generate five volume blocks with 64^3 mesh points each.

```
0 0 0 2.d0
601
0.d0
0 0 1
1
1.d-5 20 1.005
```

As it is mentioned that the first command line satisfies the condition: $ax + by + cz + d = 0$. And it is found to be not consistent in the present case where $a = b = c = 0$ and $d = 2$. In fact there is a special meaning in this case where an rotational axis is defined. Here $d = 2$ is the radius from the rotational axis (x=0, y=0) to the cylindrical surface (the white area in Figure C.7). The surface will be generated automatically by the command lines and a symmetric condition is provided. The thing needs to be drawn attention is the root of the blade. All the mesh points describe the last slice of the blade root must lay on the cylindrical surface (such as the intersection area of two circular pipes). Other commands in file *blade.hyp* are similar as described before. By now we have the inner volume mesh of five blocks.

The following task is to extend the domain larger which shall have a spherical outer boundary with a sector of 120 degrees. The shell of the outer surface is seen in Figure C.8 which has three blocks (the green one). Three volume blocks will be filled in between the intermediate outer surface and the outer surface. The two cyclic surfaces of intermediate outer surface are not used for extruding meshes since they are already part of the outer boundaries. Therefore volume meshes are extruded from the remaining three intermediate outer surfaces and the mesh generation is stopped at the pre-defined outer surface. The command lines are shown below with a few more lines describing the cyclic boundaries.

```
0 0 0 2.d0
601
0.577 1 0 0
501
-0.577  1 0 0
501
0.d0
0 0 1
1
0.15 100 1.001
```

The first two lines are the same as before which forms a sector of cylindrical surface. The third line indicates one cyclic plane such that $0.577x+y=0$. Another cyclic plane is defined as $-0.577x+y=0$. The attribution for these two planes is 501 by the definition of EllipSys code. The inflow direction is $w=1$ which follows the z-axis. Number of blocks in the extruding direction is 1. The first cell height is 0.15 which needs to be smoothly connected with the previous cell. The previous cell is in fact the last cell we created before for the inner blocks. Therefore the mesh with a total number of 8 blocks are constructed.

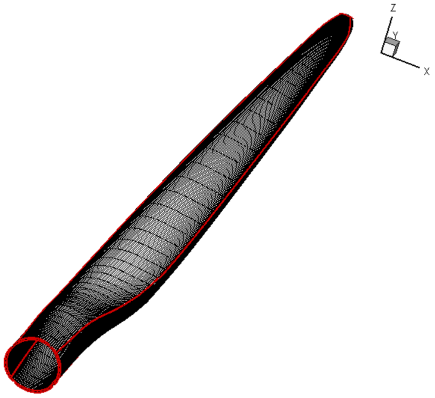

Figure C.5: Surface mesh on blade.

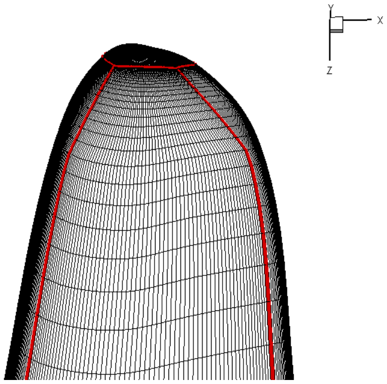

Figure C.6: Mesh on blade tip.

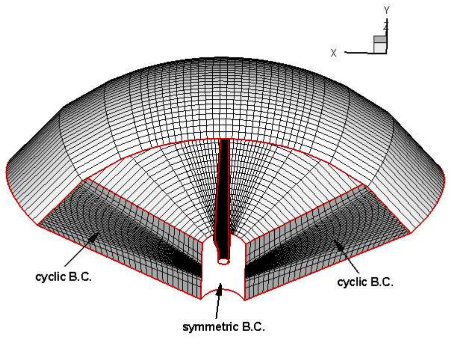

Figure C.7: Inner part of the mesh.

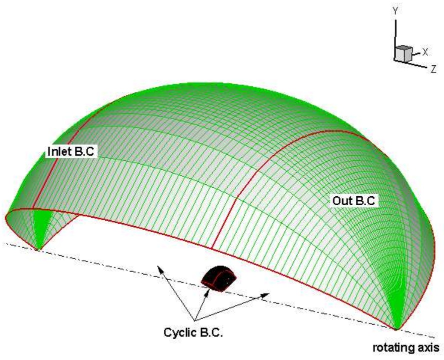

Figure C.8: The over all structure.

Case 3: Cylindrical-mesh of a three-blade turbine

In the last example we look at a three-blade large wind turbine. The length of the blade is 63 m and the maximum twist angle is 13.3 degrees. The surface mesh for this blade is shown in Figure C.9 and C.10. There are five blocks on blade surface and each has number of grid points 64 × 64. The blade tip is sharp and its geometry is described by 64 × 64 grid points, see Figure C.10. The cylindrical mesh is easier to create once the inner blocks are created. The first procedure is the same as before which does not need to be repeated. The command lines below shows that the radius of the rotational hole is 5 since the turbine is much larger.

```
0 0 0 5.d0
601
0.25d0
0 0 1
1
1.d-5 50 1.001
```

The structure of the mesh is given in Figure C.11 and C.12. The inner part of the blocks are shown in Figure C.11 where the blade is sitting on the surface of the rotational hole. In this case, the outer blocks are very easy to create since they have very regular geometries. Figure C.12 shows the overall structure the mesh where the blocks are separated by the red lines.

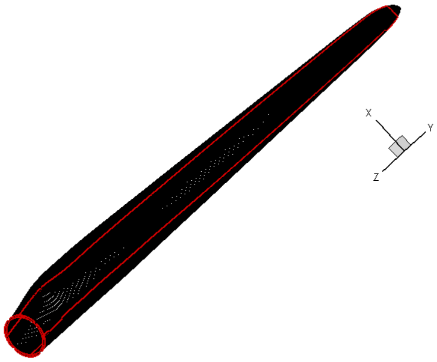

Figure C.9: Surface mesh on blade.

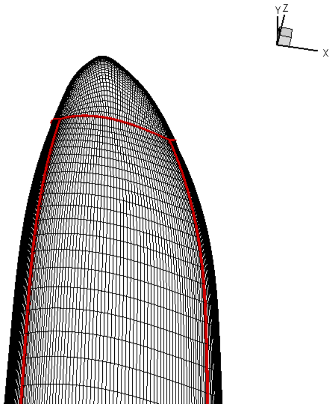

Figure C.10: Mesh on blade tip.

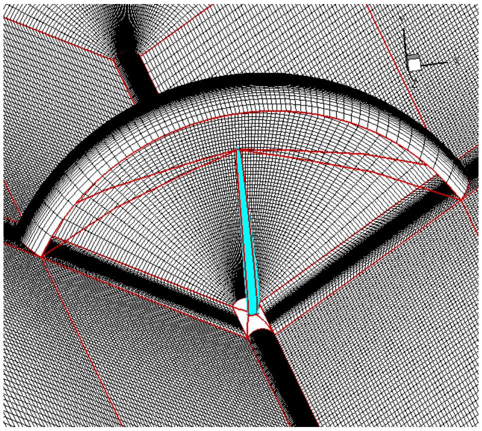

Figure C.11: Inner part of the mesh.

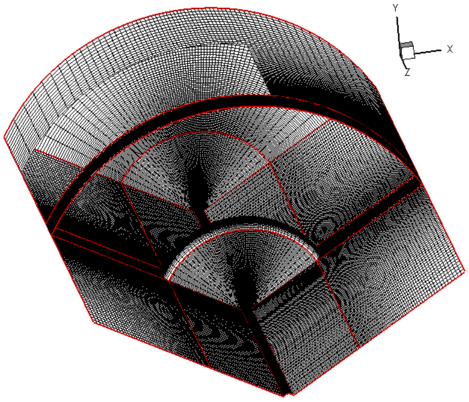

Figure C.12: The over all structure.

Bibliography

[1] Hardin J C and Pope D S 1994 An acoustic/viscous splitting technique for computational aeroacoustics. *Theoret. Comput. Fluid Dyn.* **6** 321-42.

[2] Shen W Z and Sørensen J N 1999 Comment on the aeroacoustic formulation of Hardin and Pope. *AIAA J.* **1** 141-143.

[3] Lighthill M J 1952 On sound generated aerodynamically: I.General Theory. *Proceedings of the Royal Society of London, Series A (Mathematical and Physical Sciences)* **211** 564-587.

[4] Curle N 1955 The influence of solid boundaries upon aerodynamic sound. *Proceedings of the Royal Society of London, Series A. Mathematical and Physical Sciences* **231** 505-514.

[5] Ffowcs Williams J E and Hawkings D L 1969 Sound generation by turbulence and surfaces in arbitrary motion. *Philosophical Transactions of the Royal Society of London A (Mathematical and Physical Sciences)* **264** 321-342.

[6] Colonius T, Lele S K and Moin P 1997 Sound generation in a mixing layer. *J. Fluid Mech.* **330** 375-409.

[7] Mitchell B E, Lele S K and Moin P 1999 Direct computation of the sound from a compressible co-rotating vortex pair. *J. Fluid Mech.* **285** 181-202.

[8] Inoue O and Hatakeyama N 2002 Sound generation by a two-dimensional circular cylinder in a uniform flow. *J. Fluid Mech.* **471** 285-314.

[9] Shen W Z and Sørensen J N 1999 Aeroacoustic modelling of low-speed flows. *Theoret. Comput. Fluid Dyn.* **13** 271-289.

[10] Shen W Z and Sørensen J N 2001 Aero-acoustic modelling of turbulent airfoil flows. *AIAA J.* **39** 1057-1064.

[11] Shen W Z and Sørensen J N 2004 A collocated grid finite volume method for aeroacoustic computations of low-speed flow. *J. Comput.Phy.* **196** 348-366.

[12] Tam C K W and Webb J C 1993 Dispersion-Relation-Preserving finite difference schemes for computational acoustics. *J. Comput.Phy.* **107** 262-281.

[13] Lele S K 1992 Compact finite difference schemes with spectral-like resolution. *J. Comput.Phy.* **103** 16-42.

[14] Kim J W and Lee D J 1996 Optimized compact finite difference schemes with maximum resolution. *AIAA J.* **34** 887-893.

[15] Hixon R, Nallasamy M, Sawyer S and Dyson R 2004 Comparison of numerical schemes for a realistic computational aeroacoustics benchmark problem. *AIAA Pap.* 2004 9539-9548.

[16] Farassat F 1996 Introduction to generalized functions with applications in aerodynamics and aeroacoustics. *NASA Technical paper* 3428.

[17] Brentner K S, Farassat F 1998 An analytical comparison of the acoustic analogy and Kirchhoff formulations for moving surfaces. *AIAA J.* **36** 1379-1386.

[18] Kirchhoff G R 1883 Theorie der Lichtstrahlen *Annalen der Physik und Chemie* **18** 663-695.

[19] Farassat F and Myers M K 1988 Extension of Kirchhoff's Formula to Radiation from Moving Surfaces. *J. Sound and Vibr.* **123** 451-461.

[20] Crighton D G 1975 Basic principles of aerodynamic noise generation. *Progr. Aerospace Sci.* **16** 31-96

[21] Brentner K S, Farassat F 2003 Modeling aerodynamically generated sound of helicopter rotors. *Progr. Aerospace Sci.* **39** 83-120.

[22] Farassat F and Succi G P 1983 The prediction of helicopter discrete frequency noise. *Vertica* **7** 309-320.

[23] Brentner K S and Holland P C 1997 An efficient and robust method for predicting helicopter rotor high-speed impulsive noise. *J. Sound and Vibr.* **203** 87-100.

[24] Brentner K S 1997 An efficient and robust method for computing quadrupole noise. *J. American Helicopter Society* **42** 172-181.

[25] Larsson J 2002 Computational aeroacoustics for vehicle Applications. *Chalmers University of Technology*

[26] Ask J, Davidson L, Enwald H and Larsson J 2003 An acoustic analogy applied to incompressible flow fields. *EUROMECH Colloquium Chamonix France* EUROMECH **449**

[27] Gloerfelt X, Pérot F, Bailly C and Juvé D 2005 Flow-induced cylinder noise formaulated as a diffraction problem for low Mach numbers. *J. of Sound and Vibr.* **287** 129-151.

[28] Mitchell B E, Lele S K and Moin P 1992 Direct computation of the sound from a compressible co-rotating vortex pair. *AIAA Pap.* 1992-0374.

[29] Mitchell B E, Lele S K and Moin P 1995 Direct computation of the sound from a compressible co-rotating vortex pair. *J. Fluid Mech.* **285** 181-202.

[30] Freund J B, Lele S K and Moin P 2000 Direct numerical simulation of a Mach 1.92 turbulent jet and its sound field. *AIAA J.* **38** 2023-2031.

[31] Freund J B 2001 Noise sources in a low-Reynolds-number turbulent jet at Mach 0.9. *J. Fluid Mech.* **438** 277-305.

[32] Ran H, Colonius T 2004 Numerical simulation of sound radiated by a turbulent vortex ring. *AIAA Pap.* 2004-2918.

[33] Rowley C W, Colonius T and Basu A J 2002 On self-sustained oscillations in two-dimensional compressible flow over rectangular cavities. *J. Fluid Mech.* **455** 315-346.

[34] Marsden O, Bogey C and Bailly C 2005 Noise radiated by a high-Reynolds-number 3-D airfoil. *AIAA Pap.* 2005-2817.

[35] Arakawa C, Fleig O, Iida M and Shimooka M 2005 Numerical approach for noise reduction of wind turbine blade tip with Earth Simulator. *J. Earth Simulator* **2** 11-33.

[36] Bogey C, Bailly C and Juvé D 2002 Computation of flow noise using source terms in linearized Euler's equations. *AIAA J.* **40** 235-243.

[37] Bogey C, Bailly C and Juvé D 2001 Noise computation using Lighthill's equation with inclusion of mean flow-acoustics interactions. *AIAA Pap.* 2001-2255.

[38] Bailly C and Juvé D 1999 A stochastic approach to compute subsonic noise using linearized Euler's equations. *AIAA Pap.* 1999-1872.

[39] Bailly C Lafon P and Candel S 1995 A stochastic approach to compute noise generation and radiation of free turbulent flows. *AIAA Pap.* 1995-092.

[40] Ribner H S 1996 Effects of jet flow in jet noise via an extension to the Lighthill model. *J. Fluid Mech.* **321** 1-24.

[41] Colonius T and Lele S K 2004 Computational aeroacoustics: progress on nonlinear problems of sound generation. *Progress in Aerospace Sci.* **40** 345-416

[42] Batchelor G K 1967 An introduction to fluid dynamics. *Cambridge Univ. Press, Cambridge, England, UK.* 164-171

[43] Hardin J C and Pope D S 1995 Sound generation by flow iver a two-dimensional cavity. *AIAA J.* **33** 407-412.

[44] Ekaterinaris J A 1999 New formulation of Hardin-Pope equations for aeroacoustics. *AIAA J.* **9** 1033-1039.

[45] Ekaterinaris J A 1997 Upwind scheme for acoustic disturbances generated by low-speed flows. *AIAA J.* **35** 1448-1455.

[46] Dahl K S 1996 Aeroacoustic computation of low Mach number flow. *number flow. Ph.D. thesis, Risø-R-947(EN), RisøNational Lab., Roskilde, Denmark.*

[47] Wells V L and Renant R A 1997 Computing aerodynamically generated noise. *Annu. Rev. Fluid Mech.* **29** 161-199.

[48] Colonius T and Lele S K 2004 Computational aeroacousrics : progress on nonlinear problems of sound generation. *Annu. Rev. Fluid Mech.* **38** 483-512.

[49] Wang M, Freund J B and Lele S K 2006 Computational prediction of flow-generated sound. *Annu. Rev. Fluid Mech.* **38** 483-512.

[50] Bogey C and Bailly C 2004 A family of low dispersion and low dissipative explicit schemes for flow and noise computations. *J. Comput.Phy.* **194** 194-214.

[51] Visbal M R and Gaitonde D V 2001 Very high-order spatially implicit schemes for computational acoustics on curvilinear meshes. *J. Comp. Acoustics.* **9** 1259-1286.

[52] Tam C K W 1995 Computational aeroacoustics: Issues and Methods. *AIAA J.* **33** 1788-1796.

[53] Canuto C, Hussaini M Y, Quarteroni A and Zang T A 1987 Spectral methods in fluid dynamics. *Springer-Verlag, New York.*

[54] Tam C K W and Dong Z 1994 Wall boundary conditions for high-order finite-difference schemes in computational aeroacoustics. *Theoret. Comput. Fluid Dyn.* **6** 303-322.

[55] Zhuang M and Chen R F 1998 Optimized upwind dispersion-relation-preserving finite difference scheme for computational aeroacoustics. *AIAA J.* **36** 2146-2148.

[56] Zhuang M and Chen R F 2002 Applications of high-order optimized upwind schemes for computational aeroacoustics . *AIAA J.* **40** 443-446.

[57] Berland J, Bogey C and Bailly C 2004 Optimized explicit schemes: matching and boundary schemes and 4th-order Runge-Kutta algorithm. *AIAA Pap.* 2004-2814.

[58] Bogey C, Bailly C and Juvé D 2003 Noise investigation of a high subsonic moderate Reynolds jet using compressible large eddy simulation. *Theoret. Comput. Fluid Dyn.* **6** 273-297.

[59] Carpenter M H, Gottlieb D and Abarbanel S 1993 The stability of numerical boundary treatments for compact high-order finite-difference schemes. *J. Comput.Phy.* **108** 272-295.

[60] Djambazov G S, Lai C H and Pericleous K A 2000 Staggered-mesh computation for aerodynamic sound. *AIAA J.* **38** 16-21.

[61] Kreiss H O 1968 Stability theory for difference approximations of mixed initial boundary value problems. *I. Math Comp.* **22** 703-714.

[62] Gustafsson B, Kreiss H O and Sundstrom A 1972 Stability theory for difference approximations for mixed initial boundary value problems. *II. Math Comp.* **26** 649-686.

[63] Kim J W 2007 Optimised boundary compact finite difference schemes for computational aeroacoustics. *J. Comput.Phy.* **225** 995-1019.

[64] Li Y 1997 Wavenumber-extended high-order upwind-baiased finite-difference schemes for convective scalar transport. *J. Comput.Phy.* **133** 235-255.

[65] Zhu Q Y and Li Y 2004 An upwind compact approach with group velocity control for compressible flow fields. *Int. J. Numer. Meth. Fluids* **44** 463-482.

[66] Kim C 2004 High-order upwind leapfrog methods for multi-dimensional acoustic equations. *Int. J. Numer. Meth. Fluids* **44** 505-523.

[67] Hixon R 2000 Prefactored small-stencil compact schemes. *J. Comput. Phys.* **165** 522-541.

[68] Hixon R and Turkel E 2000 Compact implicit MacCormack-type schemes with high acuracy. *J. Comput. Phys.* **158** 51-70.

[69] Hixon R 1998 A New Class of Compact Schemes. *AIAA Paper* 98-0367.

[70] Ashcroft G and Zhang X 2003 Optimized prefactored compact schemes. *J. Comput. Phys.* **190** 459-477.

[71] Chu P C and Fan C 1998 A three-point combined compact difference scheme. *J. Comput. Phys.* **140** 370-399.

[72] Chu P C and Fan C 1999 A three-point sixth-order nonuniform combined compact difference scheme. *J. Comput. Phys.* **148** 663-674.

[73] Hu F Q, Hussaini M Y and Manthey J 1996 Low-dissipation and low-dispersion Runge-Kutta schemes for computational acoustics. *J. Comput. Phys.* **124** 177-191.

[74] Berland J, Bogey C and Bailly C 2006 Low-dissipation and low-dispersion fourth-order Runge-Kutta algorithm. *Computers & Fluids.* **35** 1459-1463.

[75] Vasilyev O V, Lund T S and Moin P 1998 A general class of commutative filters for LES in complex geometries. *J. Comput. Phys.* **146** 82-104.

[76] Berland J, Bogey C, Marsden O and Bailly C 2007 High-order, low dispersive and low dissipative explicit schemes for multiple-scale and boundary problems . *J. Comput. Phys.* **224** 637-662.

[77] Gaitonde D V and Visbal M R 2000 Pade-type higher-order boundary filters for the NavierStokes equations. *AIAA J.* **38** 21032112.

[78] Visbal M R and Gaitonde D V 1999 Higher-order-accurate methods for complex unsteady subsonic flows. *AIAA J.* **37** 1231 1239.

[79] Bogey C and Bailly C 2002 Three-dimensional non-reflective boundary conditions for acoustic simulations: far field formulation and validation test cases. *ACTA Acoustica United with Acoustica* **88** 463-471.

[80] Israeli M and Orszag S 1981 Approximation of radiation boundary conditions. *J. Comput. Phys.* **41** 115-135.

[81] Adams N A 1998 Direct numerical simulation of turbulent compressible ramp flow. *Theoret. Comput. Fluid Dyn.* **12** 109-129.

[82] Tam C K W and Dong Z 1994 Wall boundary conditions for high-order finite difference schemes in computational aeracoustics. *Theoret. Comput. Fluid Dyn.* **6** 303-322.

[83] Thompson K W 1987 Time dependent boundary conditions for hyperbolic systems, I. *J. Comput. Phys.* **68** 1-24.

[84] Thompson K W 1990 Time dependent boundary conditions for hyperbolic systems, II. *J. Comput. Phys.* **89** 439-461.

[85] Bayliss A and Turkel E 1982 Far-field boundary conditions for compressible flows. *J. Comput. Phys.* **48** 182-199.

[86] Hu F Q 1996 On absorbing boundary conditions for linearized Euler equations by a perfect matched layer. *J. Comput. Phys.* **129** 201-219.

[87] Hu F Q 2001 A stable, perfect matched layer for linearized Euler equations in unsplit physical varaibles. *J. Comput. Phys.* **173** 455-480.

[88] Giles M B 1990 Nonreflecting boundary conditions for Euler equation calculations. *AIAA J.* **28** 2050-2058.

[89] Kim J W and Lee D J 2000 Generalized characterisctic boundary conditions for computational aeroacoustic. *AIAA J.* **38** 2040-2049.

[90] Hariharan S I and Hagstrom T 1989 Farfield expansion for anisotropic wave equations. NASA-Tn-102112.

[91] Berenger J P 1994 A perfectly matched layer for the absorption of electromagnetic waves. *J. Comput. Phys.* **114** 185-200.

[92] Tam C K W and Dong Z 1996 Radiation and outflow boundary conditions for direct computation of acoustic and flow disturbances in a nonuniform mean flow. *J. Comput. Acoust.* **4** 175-201.

[93] Tam C K W, Fang J and Kurbatskii K A 1998 Non-homogeneous radiation and outflow boundary conditions simulating incoming acoustic and vorticity waves for exterior computational aeracoustics problems. *Int. J. Numer. Meth. Fluids* **26** 1107-1123.

[94] Hixon R, Shih S H and Mankbadi R R 1995 Evaluation of boundary conditions for computationa aeroacoustics. *AIAA J.* **33** 2006-2012.

[95] Michelsen J A 1992 Basis3D - a platform for development of multiblock PDE solvers. Technical report, AFM 92-05, Technical University of Denmark, Denmark.

[96] Sørensen, N N 1995 General purpose flow solver over hills. *Risø-R-827(EN)*, Risø National Laboratory, Roskilde.

[97] Shen W Z, Michelsen J A and Srensen J N 2001 An improved Rhie-Chow interpolation for unsteady flow computations. *AIAA J.* **39** 2406-2409.

[98] Shen W Z, Michelsen J A, Sørensen N N and Sørensen J N 2003 An improved SIMPLEC method for steady and unsteady flow computations. *Numer. Heat Trans.* **43** 221-239.

[99] Tam C K W and Hardin J C (Eds.) 1997 Second Computational Aeroacoustics Workshop on Benchmark Problems. NASA CP-3352.

[100] Powell A 1964 Theory of vortex sound. *J. Acoustic Society of America* **36** 177-195.

[101] Müller E A and Obermeier F 1967 The spinning vortices as a source of sound. *AGARD CP-22* 22.1-22.8.

[102] Lee D J and Koo S O 1995 Numerical study of sound generation due to a spinning vortex pair. *AIAA J.* **33** 20-26.

[103] Ekaterinaris J A 1997 An upwind scheme for the computation of acoustic field generated by incompressible flow. *AIAA J.* **35** 1448-1455.

[104] Scully M P 1975 Computation of helicopter rotor wake geometry and its influence on rotor harmonics airloads. *Massachusetts Inst. Of Technology, Pub. ARSL TR 178-1, Cambridge, MA.*

[105] Stremel P M 1984 A method for modelling finite core vortices in wake flow calculations. *AIAA Paper* 84-0417.

[106] Strouhal V 1878 Ueber eine besondere art der tonerregung. *Annu. Phys. Chem. (Wied. Annu. Phys.)* **5** 216-251.

[107] Fey U, Köning M and Eckelmann H 1998 A new Strouhal-Reynolds-number relationship for the circular cylinder in the range $47 < Re < 10^5$. *Phys. Fluids* **10** 1547-1549.

[108] Ewert R and Schröder W 2003 Acoustic perturbation equations based on flow decomposition via source filtering. *J. Comput. Phys.* **188** 365-398.

[109] Seo J H and Moon Y J 2005 Perturbed compressible equations for aeroacoustic noise prediction at low mach numbers. *AIAA J.* **43** 1716-1724.

[110] Seo J H and Moon Y J 2006 Linearized perburbed compressible equations for low mach number aeroacoustics. *J. Comput. Phys.* **218** 702-719.

[111] Gu W, Chyu C and Rochwell D 1994 Timing of vortex formation from and oscillationg cylinder. *Phys. of Fluids.* **6** 3677-3682.

[112] Lu X Y and Dalton C 1996 Calculation of timing of vortex formation from an oscillating cylinder. *J. Fluids Struct.* **10** 527-541.

[113] Blackburn H M and Henderson R D 1998 A study of two-dimensional flow past and oscillating cylinder. *J. Fluid Mech.* **385** 255-286.

[114] Uzunoğlu B, Tan M and Price W G 2001 Low-Reynolds-number flow around an oscillating circular cylinder using a cell viscous boundary element method. *Int. J. Numer. Meth. Engng.* **50** 2317-2338.

[115] Ongoren A and Rockwell D 1988 Flow structure from an oscillating cylinder. Part 1. Mechanisms of phase shift and recovery in the near wake. *J. Fluid Mech.* **191** 197-223.

[116] Williamson C H K and Roshko A 1988 Vortex formation in the wake of and oscillating cylinder. *J. Fluids Struct.* **2** 355-381.

[117] Blackburn H M and Melbourne W H 1997 Sectional lift forces for an oscillating cylinder in smooth and turbulent flows. *J. Fluids Struct.* **11** 413-431.

[118] Price W G and Tan M 1992 Fundamental viscous solutions or 'transient oseenlets' associated with a body manoeuvring in a viscous fluid. *Proc. Royal Society of London A.* **438** 447-466.

[119] Shen W Z and Sørensen J N 1999 Quasi-3D Navier-Stokes model for a rotating airfoil. *J. Comput.Phy.* **150** 518-548.

[120] Ta Phuoc L 1994 Modéles de sous maille appliqués aux écoulements instationnaires décollés. *Proceedings of a DRET Conference: Aérodynamique Instationnare Turbulente-Aspects numériques et expérimentaux. Paris, France: DGA/DRET editors.*

[121] Bardina J Ferziger J H and Reynolds W C 1980 Improved subgrid scale models for large eddy simulation. *AIAA paper* 80-1357.

[122] Sagaut P 2006 Large Eddy Simulation for incompressible flows. Third Edition, Springer.

[123] Sheldahl R E and Klimas P C 1981 Aerodynamics of seven airfoil sections through 180 degrees angle of attack for use in aerodynamic analysis of vertical axis wind turbines. *SAND80-2114, Sandia National Laboratories, Albuquerque, New Mexico, USA.*

[124] Shen W Z and Sørensen J N 2007 Aero-acoustic modelling using large eddy simulation. *J. Phys. Conference Series* 75 (2007) 012085

[125] Brooks T F, Pope D S and Marcolini M A 1989 Airfoil self-noise and prediction. *NASA Reference Publication 1218.*

[126] Nash E C, Lowson M V and Mcalpine A 1999 Boundary-layer instability noise on aerofoils. *J. Fluid Mech.* **382** 27-61.

[127] Piomelli U and Balaras E 2002 Wall-layer models for large eddy simulations. *Ann. Rev. Fluid Mech.* **34** 349-374.

Recent Ph.D.-dissertations in Fluid Mechanics

Sørensen, J.N. Three-Level, Viscous-Inviscid Interaction Technique for the Prediction of Separated Flow Past Rotating Wing, AFM 86-03, 1986

Michelsen, J.A. Modelling of Laminar Incompressible Rotating Fluid Flow, AFM 86-05, and Modelling of Turbulent Incompressible Rotating Fluid Flow, AFM 86-07, 1986

Sørensen, L.S. Three-Dimensional Electro-Fluid-Dynamics in Tuft Corona Wire-Plate Precipitators, AFM 89-03, 1989

Gervang, B. Numerical Simulations of 3-Dimensional Flow in Straight and Curved Ducts of Rectangular Cross Section, AFM 89-09, 1989

Andresen, E. Statistical Approach to Continuum Models for Turbulent Gas Particles Flows, AFM 90-04, 1990

Nielsen, N.F. Low Reynolds Number Fluid Dynamics with Applications to Suspending Feeding Animals, AFM 91-10, 1991

Zamany, J. Modelling of Particle Transport in Commercial Electrostatic Precipitators, Ph.D under ATV, EF316, 1992

Christensen, E.A. Laminar-Turbulent Transition in the Rotating Driven Cavity Problem, AFM 93-12, 1993

Trinh, C.M. Turbulence Modelling of Confined Swirling Flows, Risø-R-647,1993

Mayer, K.E. Experimental and Numerical Modelling of Turbulent Flows and Heat Transfer in Staggered Tube Bundles, AFM 94-03, 1994

Mayer, S. Particle Motion in Unsteady Three-Dimensional Flow at Low Reynolds Numbers , AFM 94-04, 1994

Hansen, M.O.L. Vorticity-Velocity Formulation of Navier-Stokes Equations for Aerodynamic Flows, AFM 94-07, 1994

Hvid, S.L. Curvature Based Smoothing of Plane Cubic B-spline Curves, AFM 93-08, Surface Description using Bicubic B-splines, AFM 93-10, QM3D, 3D Netgenerering, Brugermanual, AFM 94-02 and Three-Dimensional Algebraic Grid Generation, AFM 94-08 1993-94

Walther, J.H. Discrete Vortex Method for Two-Dimensional Flow past Bodies of Arbitrary Shape Undergoing Prescribed Rotary and Translational Motion, AFM 94-11, 1994

Nim, E. Energidissipation og Masseoverfrsel af Gas i og Omkring Statiske Miksere med Boblestrømning, Ph.D. under ATV, EF410, 1994

Sørensen, N.N. General Purpose Flow Solver Applied to Flow over Hills, Risø-R-827(EN), 1995

Filippone, A. Interaction of Potential Flow Model with the Navier-Stokes Equations for Rotor Aerodynamics, AFM 95-07, 1995

Jensen, E. Optimization of the Electromagnetic Flowmeter, AFM 95-09, 1995

Schmidt, J.J. Experimental and Numerical Investigation of Separated Flows, ET-PHD 97-01 1997

Nygreen, P. A Vorticity-Streamfunction Formulation of the Navier-Stokes Equations for Predicting Unsteady Flow past Bodies in Arbitrary Movement, ET-PHD 97-02, 1997

Sørensen, D.N. Aerodynamic Modelling and Optimization of Axial Fans, ET-PHD 98-01, 1998

Lennart, A.S. Experimental and Theoretical/Numerical Study of Evaporation from Shallow

Pools of Organic Liquids, at Simulated Work Conditions, ET-PHD 98-02, 1998

Johansen, J. Unsteady Airfoil Flows with Application to Aeroelastic Stability, Risø-R-1116(EN), 1999

Ullum, U. Imaging Techniques for Planar Velocity and Concentration Measurements, ET-PHD 99-03,1999

Jørgensen, B.H. Low-Dimensional Modelling and Dynamics of the Flow in a Lid Driven Cavity with a Rotating Rod, ET-PHD 2000-02, 2000

Myllerup, L. Turbulence Models for Complex Flows, ET-PHD 2000-03, 2000

Pedersen, N. Experimental Investigation of Flow Structures in a Centrifugal Pump Impeller using Particle Image Velocimetry, ET-PHD 2000-05, 2000

Voigt, L.P.K. Navier-Stokes Simulations of Airflows in Rooms and Around a Human Body, ET-PHD 2001-00, 2001

Gaunaa, M. Unsteady Aerodynamic Forces on NACA 0015 Airfoil in Harmonic Translatory Motion, MEK-FM-PHD 2002-02, 2002

Pedersen, J.M. Analysis of Planar Measurements of Turbulent Flows, MEK-FM-PHD 2003-01, 2003

Mikkelsen, R. Actuator Disc Methods Applied to Wind Turbines, MEK-FM-PHD 2003-02, 2003

Ullum, T.U. Investigation of Turbulence and Flow Structures in Electrostatic Precipitator, MEK-FM-PHD 2003-03, 2003

Hjort, S. Incompressible Boundary Layer Instability and Transition, MEK-FM-PHD 2004-01, 2004

Reck M. Computational fluid dynamics, with detached eddy simulation and the immersed boundary technique, applied to oscillating airfoils and vortex generators, MEK-FM-PHD 2005-01, 2005

Cavar D. Large Eddy Simulation of Industrially Relevant Flows, MEK-FM-PHD 2006-02, 2006